FIRST PRINCIPLE STUDY ON INTERFACIAL ENERGETIC ALIGNMENT AND CHARGE TRANSFER IN QUANTUM DOTS FUNCTIONALIZED VIA METAL-ORGANIC DYE

A Dissertation
Submitted to the Graduate Faculty
of the
North Dakota State University
of Agriculture and Applied Science

By

Peng Cui

In Partial Fulfillment of the Requirements
for the Degree of
DOCTOR OF PHILOSOPHY

Major Program:
Materials and Nanotechnology

November 2016

Fargo, North Dakota

North Dakota State University
Graduate School

Title

First Principle Study on Interfacial Energetic Alignment and Charge Transfer in Quantum Dots Functionalized via Metal-Organic Dye

By

Peng Cui

The Supervisory Committee certifies that this ***disquisition*** complies with North Dakota State University's regulations and meets the accepted standards for the degree of

DOCTOR OF PHILOSOPHY

SUPERVISORY COMMITTEE:

Svetlana Kilina
Chair

Erik Hobbie

Andrei Kryjevski

Simone Ludwig

Approved:

11/02/2016
Date

Erik Hobbie
Department Chair

ABSTRACT

Quantum dots (QDs) are promising materials for applications in solar energy conversion because of tunable band gap, multi-exciton generation, photon-upconversion, etc. One of the main challenges of increasing solar energy conversion is to extend the lifetime of photoexcited charge-carriers in conduction band, and one of the strategies is to functionalize QD with mediator molecules. Functionalizing QD with metal-organic dye serves as the additional channel of manipulating charge transfer – the key process increasing solar energy conversion. When metal-organic dye is attached to QD, the interfacial charge transfer direction as well as the rates are determined by a balance between the energetic alignment, QD-dye interaction as well as charge-carrier relaxation dynamics. In this dissertation, we explore the effect of dye functionalization on these elements. We change the metal ion, organic ligands as well as binding geometry of dye, size of QD, polarity of solvent, and use density functional theory to study their effects on energetic alignment. Embedding density functional calculation is used to study the dipole interaction between QD and dye providing additional controllability on charge transfer excitation. At last, we apply Tully surface hopping scheme in combining with density functional theory in time domain to study the charge-carrier relaxation dynamics and charge transfer across the heterogeneous interface in QD/dye nanocrystal composite.

ACKNOWLEDGEMENTS

First of all, I would like to acknowledge my major advisor Dr. Svetlana Kilina, for accepting me as a student, and financially supporting me during the entire period of PhD by offering research assistantship in Chemistry and Biochemistry Department. During the four years in chemistry department, I benefit a lot by collaborating with people in different area, not only academically, but also the friendship that makes me feel like living inside a big family all the time.

Second, I would like to thank Dr. Erik Hobbie, for holding the first two years of fellowship to support my study and research under Materials and Nanotechnology Program. The special thanks should be given to Dr. Wenfang Sun, one of the best organic chemists in NDSU, who allows me to collaborate with her group members, Dr. Li Wang, Dr. Xiaolin Zhu, etc. They are wonderful guys! I also like to give my thanks to Dr. Andrei Kryjevski and Dr. Simone Ludwig, for agreeing to be my committee members.

At last, I want to say thanks to all my friends in NDSU. Without your support, I cannot go this far, and I will always treasure our friendship.

DEDICATION

To My Dearest Family.

TABLE OF CONTENTS

ABSTRACT iii

ACKNOWLEDGEMENTS iv

DEDICATION v

LIST OF TABLES ix

LIST OF FIGURES xi

CHAPTER 1. INTRODUCTION 1

1.1. General Overview of Solar Energy Conversion 1

1.1.1. Dye sensitizer 4

1.1.2. Quantum dot sensitizer 8

1.2. Challenges in Measuring and Modelling Interfacial Charge Transfer 12

1.3. Main Goals and Outline of the Dissertation 16

CHAPTER 2. METHODS AND COMPUTATIONAL DETAILS 19

2.1. Effective Mass Approximation for Modelling Electronic Structure and Optical Properties of Quantum Dots 19

2.2. Using Density Functional Theory in the Calculations of Nonadiabatic Couplings 24

2.3. Trajectory Surface Hopping (TSH) 27

2.4. Charge-constrained Density Functional Theory and Electronic Coupling 29

2.5. Embedded Fragment Potential Model 32

CHAPTER 3. MODELLING THE STRUCTURES AND SURFACES OF DYE FUNCTIONALIZED QDs 36

3.1. Geometries of $Cd_{33}Se_{33}$ QD 36

3.2. Geometries and Attachments of Dye Complexes 38

3.3. Computational Methods 39

3.3.1. Ground state and optical property calculations of the QD/dye composites 39

3.3.2. Embedded fragment and constrained DFT for calculations of QD-dye interaction as well as electronic coupling 42

3.3.3. Calculations of the NA-couplings and NA-dynamics 44

CHPATER 4. EFFECT of METAL ION ON ENERGETIC ALIGNMENT AND CHARGE TRANSFER EXCITATION 46

4.1. Results and Discussion 46

4.1.1. Geometrical structures 46

4.1.2. Dependency of the spin-State energetics of dye on the exact exchange in functional 51

4.1.3. Energetic alignment between QD and dye 55

4.1.4. QD-dye interaction and photoinduced charge transfer 59

4.2. Summary 73

CHAPTER 5. EFFECT OF LIGANDS ON ENERGETIC ALIGNMENT AND EXCITED-STATE PROPERTIES 75

5.1. Results and Discussion 75

5.1.1. Mutual energy alignment of dye and QD states 77

5.1.2. Band offsets: role of QD-dye interactions 87

5.1.3. Thermodynamic conditions for charge transfer 92

5.1.4. Excited state properties of QD/dye composites 95

5.2. Summary 98

CHAPTER 6. EFFECT OF BINDING GEOMETRY ON ENERGETIC ALIGNMENT AND ELECTRONIC COUPLING 101

6.1. Results and Discussion 101

6.1.1. Binding geometries 101

6.1.2. Energetic alignments of QD/dye composites 105

6.1.3. Electronic coupling 128

6.1.4. Optical absorption 130

6.2. Summary 131

CHAPTER 7. NONADIABATIC CHARGE-CARRIER RELAXATION IN $Cd_{33}Se_{33}$ QD/Ru(II) POLYPYRIDINE NANOCOMPOSITE 133

7.1. Results and Discussion 133

7.1.1. Ground-state electronic properties and optical spectra 133

7.1.2. Time-domain photoinduced electron- and hole relaxation 140

7.2. Summary 146

CHAPTER 8. CONCLUSION 148

REFERENCES 150

LIST OF TABLES

Table Page

1. Average NBO charges for the bare and the $[Me(II)(bpy)_2(mcb)]^{1+}$ dye functionalized $Cd_{33}Se_{33}$ QDs calculated in vacuum and solvent. 48

2. Averaged Cd-Se, Cd-O, C-C, C-N, C-H and N-Me(II) bond lengths (Å) of $Cd_{33}Se_{33}$ QD/Me(II) complex composite in vaccum, CH_3CN and CH_3Cl. 50

3. The highest occupied $dz2$ orbitals in isolated Me(II) complex and $Cd_{33}Se_{33}$ QD/Me(II) complex composite. The calculations are performed in CH_3Cl. 62

4. Natural transition oribitals of lowest optical transition and first absorption in $Cd_{33}Se_{33}$ QD/Me(II) dye composite, as marked by dark arrows and green arrows in Figure 15. The calculations are performd in CH_3CN. 66

5. Charge density differences (CDDs) of $Cd_{33}Se_{33}$ QD/$[Me(II)(bpy)_2(mcb)]^{1+}$ dye nanocomposite between the excited states and ground state for all the bright transitions with oscillation strengths (f) larger than 0.1. The energy window of excitation is between 600 nm and 400 nm, and calculated by B3LYP functional. Green color represents holes and red color represents electrons. The calculations are performed in CH_3Cl. 70

6. Difference between Energies of the Highest Occupied Orbitals of the Dye and the QD ($\Delta E = HOMO_{QD} - HOMO_{dye}$) in eV and the Dipole Moments (μ) in Debye[a] 89

7. Difference between Energies of the Highest Occupied Orbitals of the Dye and the QD ($\Delta E = HOMO_{QD} - HOMO_{dye}$) and the Dipole Moments (μ) of $Cd_{33}Se_{33}$/1a Composites in Different Solvents with the Complexes 1a Attached to Different Surfaces Labeled As A, B, and D[a] 91

8. Binding energy, band gap, Cd-S, Cd-O bond lengths of $Cd_{33}Se_{33}$ QD/N719 dye composites with different anchoring group as well as the surface orientation, in vacuum and CH_3CN, respectively 104

9. Frontier Molecular orbitals (FMOs) of ground state at the occupied and unoccupied energy levels of $Cd_{33}Se_{33}$ QD/N719 dye nanocrystal composite in vacuum. 107

10. Frontier Molecular orbitals (FMOs) of charge constrained state (*et* or *rt*) at the occupied and unoccupied energy levels of $Cd_{33}Se_{33}$ QD/N719 dye nanocrystal composite in vacuum 111

11. Frontier Molecular orbitals (FMOs) of ground state at the occupied and unoccupied energy levels of $Cd_{33}Se_{33}$ QD/N719 dye nanocrystal composite in CH_3Cl. 116

12. Electronic coupling vectors (charge transfer integrals) for electron-transfer (*et*) as well as electron & hole recombination (*re*) 120

13. Ionization potentials of isolated N719 dyes. The structures are cut from $Cd_{33}Se_{33}$ QD/N719 dye composites, and optimized. The calculations are performed in vacuum with the same functional and basis set as in other calculations 121

LIST OF FIGURES

Figure Page

1. A diagram illustrating solar energy conversion cycle adopted from [6]. (1) Photons with energies below the band gap (E_g) are not absorbed. (2) Photons with energies above band gap excite electron from valence band (VB) to conduction band (CB) assisted by vibrational motions of molecules or lattices, where the additional energies are converted to phonons. (3) The impurities or surface defects of bulk could prompt nonradiative recombination paths between electrons and holes, while in case of nanocrystals surface trap states dominates nonradiative recombination paths. (4) Electron recombines with hole radiatively and produces one photon with energy equal to the band gap. Mostly, the radiated photons are reabsorbed, however, if this occurs in the opposite direction of incoming sunlight the energy is lost forever, which limits the efficiencies of solar cells. 3

2. General working mechanism of dye sensitized solar cell adopted from [1]. 6

3. spiro-OMeTAD molecule [19]. 7

4. Potential energy curves of an electron transfer reaction. q represents the reaction coordinate [137] 31

5. $Cd_{33}Se_{33}$ QD (left), $Cd_{111}Se_{111}$ QD (middle), and ligated $Cd_{33}Se_{33}$ QD (right). 36

6. Schematic structures of [Me(II)(bpy)2(mcb)]1+ (left), Black dye (middle), and N719 dye (right). 38

7. Three attaching modes of carboxylate anchor on the surface of QD, the bridging (a), unidentate (b) and chelation (c). 39

8. Schematic representation of different charge transfer pathway upon the photoexcitation of $Cd_{33}Se_{33}$ QD functionalized by N719 dye. For the displayed energetic alignment there are three possible pathways: (1) electron transfer (*et*) between lowest unoccupied energy levels of QD and dye; (2) electron in LUMO recombines with hole at VB edge (*re*). 43

9. (a) $Cd_{33}Se_{33}$ QD functionalized by tris(2,2-bipyridine) Me(II) complex ($[Me(bpy)_2(mcb)]^{1+}$). (b) schematic structure of $[Me(bpy)_2(mcb)]^{1+}$ complex. (c) $[Me(bpy)_2(mcb)]^{1+}$ complex is attached on QD's surface through carboxylic acid linker. (d) The order of magnitudes of pauli electronegativities between different transition metal is: Os=Ru>Fe>Cd>Cr. 47

10. The energy differences (relative energies) between the singlet, triplet and quartet states for $[Me(II)(bpy)_3]^{2+}$ complex and $[Me(II)(bpy)_2(mcb)]^{1+}$ complex. The zero point is chosen to be the spin state of lowest energy. All complexes have the singlet states in lowest energies except $[Cr(II)(bpy)_3]^{2+}$ and $[Fe(II)(bpy)_3]^{2+}$ complexes. As the percentage of exact exchange in B3LYP functional decreased from 30%, 25% to 20%, it does not significantly affect the relative energetic positions between the spin states for most metal complexes. However, the singlet state of $[Fe(II)(bpy)_3]^{2+}$ complex is initially higher in energy than triplet state, which switches to triplet ground state when the exact exchange is reduced to 20%..... 53

11. Projected density of states (PDOS) of $Cd_{33}Se_{33}$ QD/Os(II) dye complex composite in vacuum and in solvent, respectively. The energy difference between the HOMOs of Me(II) complex and QD is denoted as E_{oc}, while the energy difference between the lowest unoccupied states of Me(II) complex and QD is denoted as E_{un}. The total band gap is denoted as E_g..... 56

12. Projected density of states (PDOS) of $Cd_{33}Se_{33}$ QD functionalized by Fe(II), Ru(II) and Cd(II) dye, respectively. The calculations are performd in vacuum (left column) and CH_3CN (right column), respectively. 57

13. (a) Band gaps (E_g) of dye functionalized $Cd_{33}Se_{33}$ QDs in vacuum, CH_3CN and CH_3Cl, respectively, which increase with the polarity of solvent. There exists a significant difference between the band gaps of QDs functionalized by different Me(II) complex, in solvent, i.e. Cd(II) > Fe(II) > Ru(II) > Os(II) > Cr(II). However, the difference beomes smaller in vacuum. (b) Band gaps ($E_{g'}$) of bare QD and isolated Me(II) dye that are directly cut from QD/dye composite. The calculations are performed in CH_3CN. (c) and (d) are the energy differences (E_{oc}) between the highest occupied states, and the energy differences (E_{un}) between the lowest unoccupied states in QD/dye composite. The E_{oc} and E_{un} for Cr(II) deviate from the trace line of other metals (dashed line)..... 58

14. (a) Multipole interaction energies (absolute values) of $Cd_{33}Se_{33}$ QD/Me(II) dye composites by performing the distributed multipolar analysis (DMA). (b) The dipole-dipole energy between $Cd_{33}Se_{33}$ QD and Cr(II) complex or Os(II) complex is larger than the other dyes..... 61

15. Absorption spectra of $Cd_{33}Se_{33}$ QD/Me(II) dye composite (black line), bare $Cd_{33}Se_{33}$ QDs (dashed dot red line) and isolated Me(II) complexes (dashed blue line). The green arrow marks the first absorption peak, while the black arrow marks the lowest optical transition. The geometries of bare $Cd_{33}Se_{33}$ QDs and isolated Me(II) complexes are cut from the dye functionalized $Cd_{33}Se_{33}$ QDs, then TDDFT calculations are carried out for the dye functionalized $Cd_{33}Se_{33}$ QDs, bare $Cd_{33}Se_{33}$ QDs and isolated Me(II) complexes in CH_3CN, respectively. The left and right columns show the absorption spectra calculated by CAM-B3LYP functional and B3LYP functional, respectively. CAM-B3LYP functional blue shifts the absorption spectra. Both B3LYP and CAM-B3LYP calculations show three types of optically active transitions: QD-to-QD, QD-to-dye, dye-to-dye; however dye-to-QD transition is optically dark in both spectra. Both spectra show a good additive feature, i.e. the curvature of bare $Cd_{33}Se_{33}$ QD adds the curvature of isolated dye approximately matches the curvature of QD/dye composite. For $Cd_{33}Se_{33}$ QD/Cd(II) dye composite the first absorption peak overlaps with the lowest optical transition. 63

16. The first optical transition energies of bare QDs, marked by filled symbols, and isolated Me(II) complexes, marked by void symbols. The geometries of bare QDs and isolated Me(II) complexes were kept as the same as in the optimized functionalized QDs. B3LYP functional and CAM-B3LYP functional are used to calculate the first optical transition energies, which are denoted by squre and triangle symbols, respectively. CAM-B3LYP functional blue shifts the energies of lowest optical transition. The first optical transition energies of isolcated Cd(II) complex are in the ultraviolet range, which are not shown..... 68

17. The optical transition energy of MLCT and π,π^*. 68

18. Optimized geometries of $Cd_{33}Se_{33}$ quantum dots (QDs) functionalized by Ruthenium(II)-2,2-bipyridine complexes with one carboxyl group $[Ru(II)(bpy)_2(mcb)]^{1+}$, complex 1, or two carboxyl groups $[Ru(II)(bpy)(mcb)_2]^0$, complex 2. Left and right columns illustrate the protonated (1 and 2) and deprotonated (1a and 2a) complexes attached to the surface of $Cd_{33}Se_{33}$ in the bridging mode, respectively. The bottom are Ru(II) functionalized QDs passivated by 8 OPMe3 ligands (left) and 19 OPMe3 ligands (right). 76

19. Structures of the systems we studied. On the left, the schematic structure of black dye (BD). Middle and right panels show the $Cd_{33}Se_{33}$ functionalized by the black dye attached via the carboxylate (QD/BD-c) and isothiocyanate (QD/BD-t) groups..... 77

20. PDOS of the $Cd_{33}Se_{33}$ QD functionalized by derivatives of Ru(II)-bipyridines (a−d) and the black dye (e−f). Calculations are done by CAM-B3LYP functional in chloroform. Zero energy is chosen at the middle of the HOMO−LUMO gap for all systems. The PDOS represents the contributions from the QD's surface (red) and core (dashed magenta) atoms, the Ru(II) ion (blue), the bipyridine (bpy) and terpyridine (tpy) ligands (cyan), the carboxylate (COO) groups (green for nonanchoring and teal for anchoring), thiocyanate groups (orange), and the passivating ligands OPMe3 (gray). The orbitals near the edge of the CB originate from the complex orbitals, independent of the complex. Orbitals associated with Ru(II) ion are deep inside in the VB of the QD functionalized by the Ru(II)-bipyridines, but are at the edge of the QD's VB for the black dye functionalization. 78

21. Representative molecular orbitals (MOs) of $Cd_{33}Se_{33}$ QD functionalized by the complex 1a (right panels) and the black dye (left panels). Calculations are done by CAM-B3LYP functional in chloroform. 79

22. Projected density of states (PDOS) of $Cd_{33}Se_{33}$ QDs functionalized with Ru(II) dyes bearing different charge: -1, 0, 1 and 2, respectively. Schematic structures of dye complexes are shown in left column. Middle column and right column are PDOS of QDs functionalized with different Ru(II) dye in Chloroform and Benzonitrile, respectively. All functionalized QDs are calculated by B3LYP functional. A mixed basis set is applied to all atoms, where LANL2DZ basis set is used for heavy atoms (Cd, Se, Ru) and 6-31G* is used for the other atoms (C, H, Ru, O). 81

23. Dependence of the PDOS of $Cd_{33}Se_{33}$ functionalized by the complex 1a (left panels a−c) and the black dye (right panels d−f) on the solvent polariry. PDOS is calculated by CAM-B3LYP functional in vacuum (a and d), chloroform (b and e) and benzonitrile (c and f). The line colors corresponding to contributions of different parts of systems are kept the same as in Fig 5.2. Zero energy is chosen at the middle of the HOMO−LUMO gap for all systems. 82

24. Projected density of states (PDOS) of $Cd_{33}Se_{33}$ QDs functionalized with derivatives of black dye (a-c) in Chloroform. Left column is the schematic structures of three derivatives of black dye, and right column is the PDOS of corresponding functionalized QDs. 85

25. Comparison of the DOS for two sizes of bare QDs in vacuum (top) and benzonitrile solvent (bottom). Calculations are done by CAM-B3LYP functional. The DOS confirms what is expected from effective mass theory: As size increases, the band gap shrinks mainly through the conduction band of light electrons, moving closer in energy to the essentially static valence band formed by heavy holes. 87

26. Schematic representation of the electronic structure of the QD/Ru(II)-dye composites illustrating the most probable charge transfer process. Left two panels describe processes in the CdSe QD functionalized by BD, when either the BD (first column) or the QD (second column) are excited. Right two panels describe processes in the CdSe QD functionalized by Ru(II)bpy, when either the QD (third column) or the Ru(II)bpy (fourth column) are excited. The states associated with the dye are red, and QD's states are gray. The lowest unoccupied states of the dyes are marked by dashed lines to depict their optically dark character originating from their metal-to-ligand charge transfer (MLCT) nature. The hole transfer from the QD to the dye is energetically favorable in QD/BD composites, while it is absolutely unfavorable in QD/Ru(II)bpy structures..... 92

27. Calculated absorption spectra of the $Cd_{33}Se_{33}$ QD functionalized by Ru(II)−bipyridine complexes 1a (top panels) and the black dye with different anchoring configurations (middle and bottom panels) in benzonitrile. For references, the absorption spectra of the bare $Cd_{33}Se_{33}$ QD (dashed black line) and the isolated Ru(II) complex (red line) are also plotted. Isolated systems are calculated with the preserved geometry they have in the hybrid QD/dye composite. Left and right panels compare the spectra calculated by hybrid B3LYP and by the long-range corrected CAM-B3LYP functionals. For all systems, the lowest-energy weakly intensive band are associated with the Ru(II) complex, which is very distinct from the next highly intensive band dominated by the QD transitions..... 96

28. Calculated absorption spectra of the $Cd_{33}Se_{33}$ QD functionalized by Ru(II)- bipyridine complexe 1a in benzonitrile. For references, the absorption spectra of the bare $Cd_{33}Se_{33}$ QD (dashed black line) and the isolated 1a complex (red line) are also plotted. Isolated systems are calculated with the preserved geometry they have in the hybrid QD/dye composite. The hight of vertical lines corresponds to the oscillator strength of electronic transitions contributing to each absorption peak. All calculations are performed using linear response TD-DFT within B3LYP functional and mixed basis set LANL2DZ (Cd, Se, Ru)/6-31G*(C, H, O). 97

29. N719 dye is attached to the Cd atoms of $Cd_{33}Se_{33}$ QD. Both carboxylate (denoted by "O") and isocyanate groups (denoted by "S") are used for anchoring N719 dye to $Cd_{33}Se_{33}$ QD. There are four groups of attachments depending on the anchoring group: I. double-carboxylate; II. single-carboxylate; III. carboxylate/isocyanate mixture; IV. double-isocyanate. Each group contains different binding configuration of dye to QD depending on the deprotonation site, denoted by A, B, C..... 102

30. Projected density of states (PDOS) of $Cd_{33}Se_{33}$ QD functionalized by N719 dye with different binding geometry in vacuum. The highest occupied molecular orbital (HOMO) in group I, group II and group III (2S-1O, 2O-1S) are dictated by isocyanate group of dye, while it is dictated by QD for the other attachments. QD's states and dye's states are mixed near the VB edge for 2O-B and 2O-C binding geometries. 106

31. Relative energetic positions of HOMO levels of dye with respect to the vacuum level, which are derived based on the ionization potentials, according to Koopman theory. The geometries are cut from $Cd_{33}Se_{33}$ QD/N719 dye composites, then these dyes in different binding geometries are optimized to the lowest energetic configurations. The highest HOMO level appear to be the dye cut from 2S despite its HOMO in 2S deep inside the VB. On the other hand, even though the 2S-1O also has the dye states deep inside the VB; however the HOMO level of dye in 2S-1O is much lower than 2S. The calculations are carried out in vacuum with the same functional and basis set used in other calculations. 122

32. Schematics of molecular orbital hybridization at the interface between $Cd_{33}Se_{33}$ QD and isocyanate anchor as well as carboxylate anchor. Carboxylate anchor forms an effective mixture with metal state of dye, thus strongly resonates with the frontier d and π orbitals of $Cd_{33}Se_{33}$ QD. On the contrary, isocyanate anchor only forms resonate states with π orbitals of $Cd_{33}Se_{33}$ QD..... 123

33. Projected density of states (PDOS) of Cd33Se33 QD/N719 dye nanocrystal composite, in dichloromethane (dcm). 126

34. Absorption spectra of bare $Cd_{33}Se_{33}$ QD, isolated N719 dye as well as $Cd_{33}Se_{33}$ QD/N719 dye composite in dichloromethane. Both bare $Cd_{33}Se_{33}$ QD and isolated N719 dye are cut from QD/dye composite, afterwards TDDFT calculations are carried out using CAM-B3LYP functional. All spectra reveal good additive feature, i.e. the spectra profile of QD adding to the spectra profile of dye approximately equals to the spectra profile of QD/dye composite, which is typical in weakly correlated donor-acceptor system. However, there exists differences in low-energy region of the spectra between different binding geometries. In cases of 2S, 2S-1O and 1S-1O-B the first absorption peak of isolated dye is split off the first absorption peak of QD/dye composite, suggesting a polarization of interface region by QD-dye correlation, therefore the additive feature is not applicable to the low-energy region of spectra. 131

35. Black dye functionalized $Cd_{33}Se_{33}$ QD. Black dye is attached to $Cd_{33}Se_{33}$ QD with carboxylate anchoring group. The profiles of PDOS calculated by Gaussian09 and VASP software packages are highly similar to each other, (a) and (b). The highest occupied state of energy levels is dictated by the Ruthenium ion as well as related isocyanate anchoring group, while the lowest unoccupied state is dictated by QD. After scissor operation the profile of PDOS calculated by PBE functional highly resembles the hybrid functional..... 134

36. (a) Fluctuation of time-evolved Kohn-sham orbital (KSO) energies of $Cd_{33}Se_{33}$ QD/BD dye composite. E_f is the fermi level. The energy spacing in valence band is relatively smaller than conduction band indicating the density of states of hole denser than electron. Several highest occupied KSOs near the E_f separated from the main bands consists of dye character indicating QD redoxed by dye during the charge carrier relaxation. (b) is time-evolved total density of states, and (c) and (d) are time-evolved projected density of states onto the QD and dye, respectively. 135

37. Time-averaged decomposed Kohn-Sham absorption spectra, where the optical transitions are governed by the occupied- and unoccupied quantized energy levels. Each quantized energy level is composed of QD state and dye sate. At the energy range between 0 eV and 1.8 eV only dye-QD and dye-dye charge-transfer excitations occur, where the amplitude of dye-QD transitions are much larger than dye-dye transitions. At the energy range between 1.8 eV and 2 eV the absorption is dominated by QD-QD and dye-QD transitions. Above 2eV the absorption is dominated by QD-QD symmetric transitions, indicated by arrows. 137

38. (a) Time-evolved electronic- and hole relaxation-dynamics by multiplying DOS by the corresponding state occupations. (b) and (c) are projected dynamics onto $Cd_{33}Se_{33}$ QD and BD dye, respectively. The initial excitation level of electron is about 0.6 eV higher than the CB edge, while for hole it is about 0.7 eV lower than the VB edge. The y axis time scale is logarithmic for showing the initial moment of population dynamics corresponding to a shorter time scale of exciton dynamics. 141

39. Exponential fitting of energy relaxation of electron- and hole dynamics..... 142

40. Projected electronic- and hole population dynamics onto the $Cd_{33}Se_{33}$ QD (lower panel) and the BD dye (upper panel), respectively. (a) and (b) show, the populations are fluctuated in $Cd_{33}Se_{33}$ QD and BD dye during the relaxation, while (c) and (d) show, there is a significant population injection from $Cd_{33}Se_{33}$ QD to BD dye at the initial phase of relaxation dynamics. 142

41. Fourier transforms of the energy gaps between initially excited MOs and HOMO/LUMO states of holes (a) and (b) electrons. Both charge carrier couple with low frequency phonons, with electrons coupled to a slightly higher frequency mode (ca. 800 cm^{-1})..... 145

42. The initial moment of electron relaxation in $Cd_{33}Se_{33}$ QD/BD dye. 145

43. Time-dependent populations of molecular orbitals (MOs) in CB (upper panel) and VB (lower panel). The five highest occupied MOs in VB are dominated by BD dye. 146

CHAPTER 1. INTRODUCTION

1.1. General Overview of Solar Energy Conversion

With the rapid growth of industries, economic globalization and high-speed public transportations, a rising demand for electrical power poses an unprecedented challenge to human world. From daily appliances (light bulb, refrigerator, microwave oven etc) to military defenses of a country, electrical power flows through the vein of modern society and becomes the momentum driven human world forward. Traditional ways of generating electricity through burning consumptible resources, such as fossil fuel, coal, natural gas etc, are not only low efficient and nonrenewable, but also pollutes the environment. Green and renewable energy resources are right at the demand of modern society which relies heavily on electrical power. Although consumptible energy resources are still widely used for industrial and commercial purposes, clean and sustainable energy resources such as solar power, hydropower, wind power etc, are gradually replacing conventional energy resources, and more and more research proposals in green energy field gain support from governments and other funding agencies. Solar energy, converted from sunlight, is the most abundant and promising energy resource among all. Unlike the hydropower and wind power, it is not constrained by the geology. In a perfect scenario all incident light striking the earth surface can be converted to solar power, most of which are in the visible spectrum.

Solar cell is a typical photovoltaic device to convert sunlight to electrical power. The conversion efficiencies of solar cells depends on the photocurrent density measured at short circuit, the open circuit photovoltage, the fill factor of the cell, and the intensity of incident rays of light [1]. An alternative way of evaluating the efficiencies of solar cells is through external quantum efficiency (IPCE) which is defined through the photocurrent density produced under monochromatic illumination of the cell divided by the photon flux that strikes the cell [2].

Solar cells of first generation based on p-n junction silicon system. However, the production cost is around \$3/W_p(peak Watt), which reduces its competitiveness with other energy resources in the market. Currently, the photovoltaic industry of first generation solar cells is largely dependent on government's subsidies. Second generation solar cells are based on thin film technology, such as amorphous silicon, Copper indium gallium selenide, Tandem-cell etc [2]. The biggest advantage of thin-film solar cells is low production cost, typically around \$1/W_p. Current thin-film technique is mostly established on amorphous silicon (a-Si) [3]. Due to the flexibility of thin film it can be easily manufactured into different shapes, and used on different substrates. This makes the second generation solar cells have attractive appearances, thereby suitable for commercial purposes. In laboratory the efficiency of 13.5% has reached by far [4]. Some companies even claim to achieve a lower production cost than \$1/W_p by using CdTe solar modules, and the module efficiency of 10.9% is reported for such system. An alternative choice is to use copper indium gallium diselenide system (CIGS), which is reported to have the efficiency of 13.5% [5].

Second generation and first generation solar cells are both based on p-n junction devices, therefore thermodynamic efficiency is still the main cause for the performance. Typically photons with energies above band gap are converted to phonon energies. i.e. heat.

The third generation solar cells which are intentionally designed to remove the disadvantages remained in second generation solar cells, and combining the advantages of first generation solar cells and second generation solar cells together. The most notable feature in third generation solar cells is the wide application of nanotechnology. The machinery of nanomaterials as light sensitizers are shown in Figure 1. Absorbing photons prompt electrons from valence band to conduction band, subsequently electrons either nonradiatively recombine with holes or go through radiative process releasing photons after relaxing to the band edge. There exists

fundamental differences in electron-phonon or hole-phonon couplings between bulk and nanocrystal semiconductors depending on the passivating ligands, size and shape of nanocrystals. An optimization of these factors yields low thermal energies and more photoexcited electrons during photo-relaxation. In addition, the quantum confinement enhancing the interactions between electron-hole pairs, potentially used for multiple-exciton generation. To this end, nanomaterials is more promising than bulk.

One major challenge in solar energy conversion using nanomaterials is the electron-hole recombination increasing the non-radiative recombination, which strongly competes with electron transfer from the light sensitizer to photoelectrode. To address such issue, the mediator molecule or electrolyte is used to extract the photoexcited holes, and regenerating the ground state of nanomaterials.

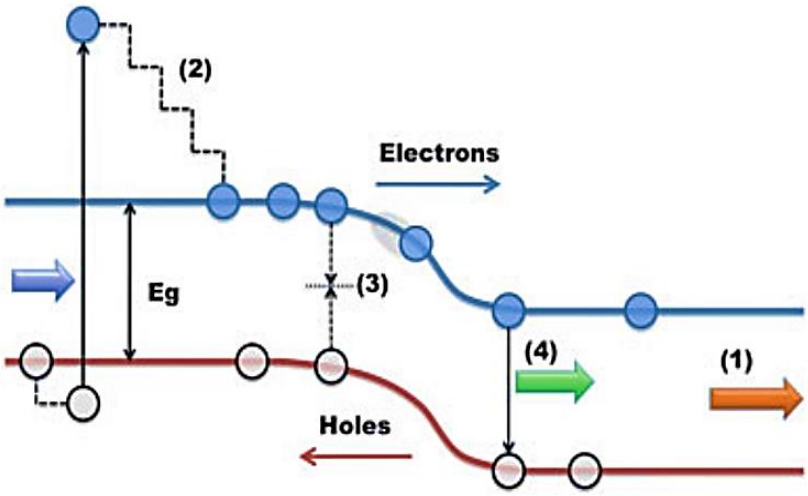

Figure 1. A diagram illustrating solar energy conversion cycle adopted from [6]. (1) Photons with energies below the band gap (E_g) are not absorbed. (2) Photons with energies above band gap excite electron from valence band (VB) to conduction band (CB) assisted by vibrational motions of molecules or lattices, where the additional energies are converted to phonons. (3) The impurities or surface defects of bulk could prompt nonradiative recombination paths between electrons and holes, while in case of nanocrystals surface trap states dominates nonradiative recombination paths. (4) Electron recombines with hole radiatively and produces one photon with energy equal to the band gap. Mostly, the radiated photons are reabsorbed, however, if this occurs in the opposite direction of incoming sunlight the energy is lost forever, which limits the efficiencies of solar cells.

1.1.1. Dye sensitizer

Efficient harvesting and conversion of solar energy to electrical or chemical energy relies on the charge separation process that prevents carrier recombination prior to their extraction to contacts. Application of molecular adsorbents forms the interface between two different media, one acting as an electron donor, and another as an acceptor. As such, this interface facilitates a quick separation of the photogenerated carriers before carrier annihilation or energy dissipation takes place, while not requiring high-quality materials as in conventional Si-based solar cells [7, 8]. This concept was first realized in the dye-sensitized solar cells, so-called Gratzel cells [9-11]. In these devices, a molecular dye - typically a chemical derivative of ruthenium(II) polybipyridine (Ru(II)-bpy) - is used as a sensitizer that absorbs visible light and then injects electrons into the large-bandgap semiconductor.

Dye sensitized solar cells are the intermediate products between first generation solar cells and second generation solar cells. The development of dye sensitizers is started from last century. In the early stage multilayers of dyes have been experimented to adsorb directly on the surface of semiconductors, however the efficiencies are found to be far less than 1% under AM 1.5G spectrum, as the smooth semiconductor surface is not able to hold many dyes. Increasing the roughness of semiconductor surface adsorbs more dyes, in addition, exposing semiconductor surface directly under electrolyte increases the redox efficiencies [12, 13]. However, it is found the conversion yields of sunlight to electricity are still below 1%, in addition, dyes cannot stably stay on the surface of semiconductor. Grätzel et al [14] presented a fractal-type TiO_2 electrode with high surface area in order to achieve a stable adsorption of dyes on the surface. The breakthrough came in 1991, a conversion yield with dye sensitized solar cells is reported to reach 7% ~ 8% by Grätzel

et al [5], which is increased by an order of magnitude than previous works. Later on, this record is renewed by the launch of N3 dye as light sensitizer raising the efficiencies up to around 10% [15].

The most promising part for dye sensitized solar cells is probably due to the fact of the availability of abundant resources of dye sensitizers. Up to date, there are hundreds of thousands of dyes had been synthetized. To increase the conversion efficiency, designing dye sensitizers should obey several rules [1]: (1) broad absorption spectrum; (2) high extinction coefficient; (3) strong binding force on surface of semiconductor; (4) proper energetic alignment with respect to conduction band of semiconductor as well as redox potential of electrolyte; (5) low toxicity and renewable; (6) high photostability for at least 20 years of use; (7) long charge carrier lifetime with very low recombination rates. Among them the energetics of dye play a fundamental role. Although smaller band gaps offer dye to absorb low energy photons increasing amounts of charge carriers, the proper excited state oxidation potential and ground state oxidation potential are equally important in order to separate charges efficiency. Excited state oxidation potential is controlled by the alignment between the lowest unoccupied energy level of dye and conduction (CB) edge of semiconductor, while ground state oxidation potential is governed by the alignment between the highest occupied energy level of dye and valence band (VB) edge of electrolyte. To design a favorable energetic configuration for dye, it should accelerate electron transfer from dye to semiconductor, and suppress the back-transfer. As such, an efficient charge separation is achieved and an apparent increase of conversion efficiency could be predicted from theoretical aspect and further verified through experiment.

To achieve efficient charge separation in dye it needs to optimize the chemical structure, and select chemically stable electrolyte to redox dye for continuous usage. An electrolyte is a substance that separates into cations and anions in a polar solution. It can redox the dye

regenerating the ground state, and typically is used in the electronic device where the chemical reactions occur at metal-electrolyte surface, such as batteries, fuel cells, electrolyte capacitor, solar cells, etc.

The general scheme of dye sensitization is illustrated in Figure 2.

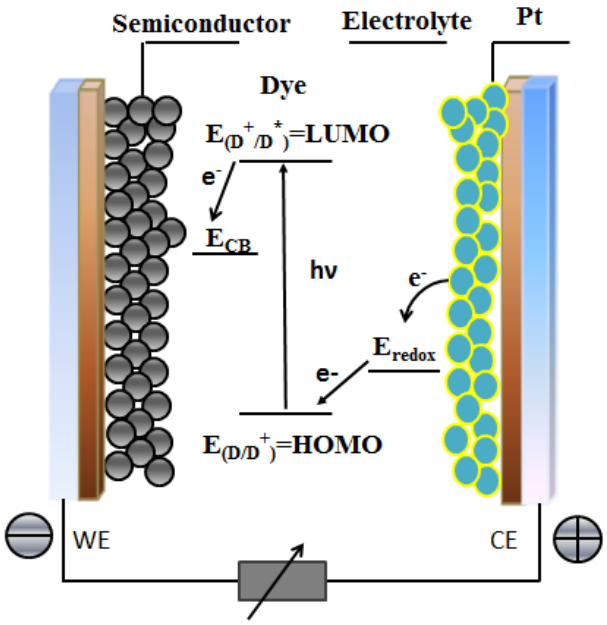

Figure 2. General working mechanism of dye sensitized solar cell adopted from [1].

Once dyes absorb photons electrons are excited to higher energy levels. If the lowest unoccupied energy level of dye is higher than that of semiconductor, the photoexcited electrons are driven to the semiconductor side, meanwhile, holes remained in VBs of dyes are reduced by electrolytes. After transferred to the semiconductor, electrons can still back-react with holes left in dye as well as oxidized electrolyte. Back reaction, existed in many different types of photocatalytic cells, is the main factor limiting the efficiency of photocatalytic cell, as it proceeds in a comparable time scale with charge separation. The interplays between charge transfer and separation have been fully examined recently through a series of experimental works on perovskite crystals [16-18], where spiro-OMeTAD molecules (Figure 3) are passivated on crystal surface acting as hole extractors. It

is estimated from the experiment that following photoexcitation the hole extraction from perovskite to dye occurs in a time scale shorter than 3 picoseconds strongly competed with electron transfer which occurs at the same time scale. Therefore, mechanistically, dye could be used as co-sensitizer to increase the conversion efficiencies of photocatalytic cells.

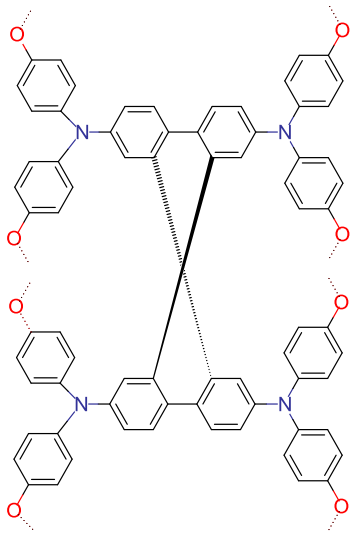

Figure 3. spiro-OMeTAD molecule [19].

Another working scenario suggests a substitution of the TiO_2 semiconductor by nanocomposites, e.g., arrays of QDs, acting as acceptors of electrons from photoexcited dyes[7, 20]. In this case, the prospect of having the ability to fabricate ultrathin, light, and flexible nanomaterials, as well as taking advantage of the size-tunable electronic properties of QDs, could be beneficial for the optimization of the work functions of devices [21], making the QD based dye-sensitized solar cells more attractive than Gratzel¨cells based on efficiencies. The charge transfer in surface-functionalized QDs is driven by mutual alignment of QD's and absorbent molecule's electronic levels [22] therefore, a controllable chemical functionalization of the QD's surface by certain molecules may help to separate charges in QDs [22-24]. Numerous experiments have

demonstrated the proof of concept of an electron or hole [25-27] extraction via adsorbent molecules. For example, functionalization of QD by metal complex promises directional charge transfer from photoexcited QD to complex, and improves solar energy conversion efficiency [28, 29]. In addition, surface voltage measurements show quantum efficiencies in CdSe QD/black dye composite and CdTe QD/black dye composite are increased by orders of magnitudes due to the light-induced hole transfer from QD to dye, which helps to decrease recombination rates in light-absorber layer of QDs thin film solar cells [21].

The main disadvantage of dye sensitized solar cells is the use of liquid electrolyte, which freezes at low temperature, while expands at high temperature making sealing the panels a series problem. Another disadvantage is the electrolyte solution containing volatile organic compounds that are hazardous to human health and environment.

1.1.2. Quantum dot sensitizer

QDs are quasi-zero dimensional materials of a few nm in diameter, where charge carriers are strongly confined inside the QDs. Such size quantization effect gives QDs a broad absorption band covering entire solar spectrum.

Using QDs as a sensitizer substituting for molecular dyes has been recently realized for semiconductor sensitized solar cells [21]. Just as in the QD-based photocatalytic agents, utilization of QDs in solar cells promises higher photostability and more efficient light absorption that can be tuned over a broad wavelength range. Additionally, the ability to generate multiple excited electron−hole pairs from a single photon, so-called carrier multiplication [30], promises significantly improved performance of photovoltaic devices[31, 32]. However, despite these potential advantages, power conversion efficiencies of QD-sensitized solar cells so far do not exceed 5%. Such relatively low performance is attributed to very rapid carrier recombination processes in these materials [33].

To attain efficient charge separation thereby allowing enough time for charges to reach the surface of electrode, tackling this problem could open up a new route to increase conversion efficiency of nanocrystal solar cell. Coupling a semiconductor nanocrystal or QD such as CdSe with another semiconductor with favorable energetics would rectify the charge delivery direction such that a spatial separation of charge carriers reduces the recombination rates between electrons and holes, thus increasing charge carrier lifetime [34]. Many different approaches of assembling a photocatalytic cell are developed along this line [7, 35, 36], among which dye is of particularly interested to be co-sensitized with QD for the reasons of: (1) abundant resources; (2) extending absorption spectrum into infrared region; (3) slowing e-h recombination rates; (4) stabilizing QD surface. The electronic structure and optical properties of a dye complex is governed by metal-ligand interaction, which can be manipulated by tuning the radii or electronegativity of metal ion [4, 37]. In addition, these dyes can be chemically attached in a controllable manner to either bulk semiconductors [38, 39] or QDs [40-42] *via* carboxylic [43] or phosphate [44] anchoring groups. Such easy tunability of attachment along with electronic structure of metal complexes *via* chemical modifications make them nearly ideal materials as hole mediators to QDs. To slow down electron−hole recombination, one can introduce structural modifications that will facilitate the hole transfer from the QD sensitizer. For example, Ru(II)-polypyridyl (N719) and Ru(II)- terpyridine (the black dye) have been shown to act as electron donors [45] by activating the hole transfer from the photoexcited QD to the dye. This prevents the electron−hole recombination between the transferred electron at the TiO2 surface and the trapped hole in the QD [45, 46]. Overall, QD-dye assemblies have a great promise to serve as an important element for both solar-to-electrical and solar-to-chemical energy conversion. In both types of applications, conditions and mechanisms of

the charge transfer from the photoexcited QD to the dye or backward play a crucial role in the device performance.

In recent development such hybrid structures reveal the enhancement of light conversion efficiencies [47, 48]. Especially, the size confinement effect of nanoparticle allows one to adjust band gap offsets as well as optical response such that a rectification of charge transfer direction could be used to separate charges in two different components. The prototypical example is given through functionalizing quantum dots (QDs) with Polypyridyl ruthenium dye (N719), where the emission spectral intensities of QDs are decreased after anchoring N719 dyes on the surface [46]. In addition, the shape of QD also has effect on excited-state dynamics. It is found CdSe nanorods with the same length but with different diameters display 8 times faster energy relaxation for thick rods than thin rods [49]. Multiexciton also draws much attention for the possible implementation in solar cells by increasing amount of photoexcited charge-carriers through Auger interaction. The relevant works can be found in reference papers [50, 51].

The mutual alignment of electronic levels in QD/dye composite and thus, the direction of photoinduced charge transfer, depend not only on which specific type of dye or what chemical compositions of QD, but also on their interactions [52, 53]. For example, charge-transfer direction between QD and dye is affected by their dipole interaction, which depends on the attachment of dye on the specific surface facet of QDs [53]. The specific type of molecular linkers (phosphonic acids [54], carboxylic acids [54], silianes [55] etc) that controls the adsorption of a metal complex to semiconductor plays a particular role in the electronic coupling between QD and dye. It either fosters or inhibits the ultrafast charge transfer, which is crucial for amplifying the short-circuit current upon the light irradiation. In addition, the dipole-dipole interaction between QD and dye has an influence on the interfacial charge transfer [56, 57]. For instance, Ru(II) complex has been

known for adsorbing on metal substrate with different configuration by controlling the protonation[39, 58]. Different configuration changes the metal-dye dipole interaction, consequently it changes the relative position of metal's lowest unoccupied molecular orbital (LUMO) with respect to Ru(II) complex's LUMO, thus changes the open circuit voltage [56]. Moreover, an instant charge transfer from dye to metal due to the electronic coupling occurs at some specific binding geometry [38]. However, in spite of the amount of studies focused on the binding geometry of a metal complex on semiconductor TiO_2 [38, 39, 56, 59-61], only few studies of these effects have been reported for semiconductor nanoparticles [62, 63]. In fact, the intrinsic dipole moment of nanocrystals is remarkably stronger than bulk solids, which means the electronic coupling in QD/dye composite plays a significant role in the dipole-dipole mediated charge transfer; however, the details of mechanism have yet to be explored.

The overall performance of QD-dye-co-sensitized photocatalytic cell is critically related with the charge carrier dynamics at the boundary between QD and dye. Some attempts to obtain the mechanistic details by probing the time-evolved electronic states of excited state dynamics, which requires a delicate design of samples as well as choosing the proper laser wavelengths, such that once excitation occurs the charge carriers could transfer along the anticipated direction, thus providing insight about interfacial charge carrier dynamics [35, 36]. However, such approach strongly depends on the system and experimental condition. In addition, for the mechanistic study the donor-acceptor electronic interaction provides elementary information for rational design of light sensitizer by engineering the interface, which again, cannot be directly obtained in experiments.

On the other hand, theory and computational modeling can provide important insights into the charge transfer direction as well as relaxation dynamics in dye functionalized QDs.

1.2. Challenges in Measuring and Modelling Interfacial Charge Transfer

Extending the lifetime of charge carrier in CBs of QDs promises an efficient charge separation between photoinduced electrons and holes in QDs in prior to radiative or nonradiative recombination. However, a roadblock to extend the lifetime is the size confinement effect of QDs, which enhances the nonradiative or radiative recombination in QDs, and increases thermally populated phonons and low amount of photoinduced electrons in CBs of QD. During the light-initiated photo-relaxation, relaxation energy is dissipated into the molecular environments, such as solvent and surface ligands. Typically, the organic or metal-organic ligands have much higher vibrational frequencies than QDs, which effectively absorbs the dissipated energies [28, 64]. At the end stage of photo-relaxation, the charge-transfer direction as well as the rate depend on the interfacial energetic alignment [65] and electronic coupling [38, 56] between QD and ligands, which require a balance between the orbital interaction, dipole interaction, charges, etc. The photoinduced electron- or hole transfer between QD and passivating ligands can occur with a proper energetic alignment between the lowest unoccupied molecular orbitals (LUMOs) or highest occupied molecular orbitals (HOMOs) of QD and ligands, increasing the amount of photoexcited charge carriers and extending their lifetimes staying in CBs[66].

There are considerable amounts of effort are now centered on proof-of-concept studies with the main focus on understanding the mechanisms of charge transfer and its competing processes. The latter include electron−hole recombination and energy transfer (i.e., when the electron−hole pair is transferred simultaneously). Different organic and metal−organic dyes have been experimentally studied as functional groups for CdSe [42, 46, 67-69], PbS [70, 71], and ZnO [20] QDs to facilitate various charge transfer processes in these composites. It was shown that the transfer of the photoexcited hole from the QD to the dye, as well as the photoexcited electron from the dye to

the QD, depends on the QD size [42], chemical composition [20], the complex type [69] and its interaction with the QD surface[67, 72]. Because the mechanisms and kinetics of charge and energy transfer and electron−hole recombination in these nanocomposites are extremely sensitive to the complicated surface chemistry of QDs, a fundamental understanding of these competitive processes is still incomplete. Experimentally, this task is difficult to address: typically electronic states associated with surface defects, impurities and QD-dye interactions are optically forbidden and cannot be probed by conventional spectroscopic means. Moreover, strongly overlapping absorption peaks of different molecular components greatly complicate identification of photoinduced carrier transport properties. It was experimentally observed that over 10 dye molecules can be adsorbed on a single QD [41]. This makes the system even more complex in terms of QD−dye interactions, as well as assembly light interactions. Overall, it is well understood that a delicate interplay between processes taking place at the QD surface controls the efficiency of light conversion to electrical or chemical energy in QD-based devices. As such, understanding the surface chemistry of QDs, in general, and to what extent we can control the photophysics of QDs by chemical functionalization, in particular, is an important prerequisite for optimization of materials for energy conversion applications.

It is challengeable to detect the photoinduced charge transfer property at the interface in strongly interacted (*via* a chemical bond) nanocrystal composite. Photoelectron spectroscopies (PES) and inverse photoelectron spectroscopies (IES) can measure the band-edge states [73]. However, to identify these states in terms of QD and dye is difficult. Optical approaches such as UV-Vis spectroscopy, is usually inhibited by selection rules due to the presence of dangling bonds in QD that are completely dark at room temperature. Electrochemical methods rely on measuring

oxidation potentials of isolated QD and isolated metal complex, separately, which is unreliable to evaluate the energetic offset in strongly interacted QD/dye composite.

On the contrary, atomistic computational approaches have no such limits. However, parameter-based methods, such as semiempirical, force field [15], Monte Carlo [74] etc., are not very suitable for modelling functionalized QDs due to a lack of explicit ways to describe the interactions between QDs and adsorbent molecules. In addition, the parameters used in those methods are highly dependent on the system, and cannot be generalized as a universal method. Although high level *ab initio* methods are robust, such as coupled cluster, multi-configuration self-consistent field (MCSCF), etc., they are computationally expensive and reported only for small systems, such as a few atoms in size clusters [75] and small dye molecules [76]. On the other hand, density functional theory (DFT) is a convenient tool for modelling system of different sizes ranging from a few to a few tens of nanometers [23, 77-79]. However, numerical accuracy of DFT is highly dependent on the choice of functionals and basis sets.

Previous DFT calculations on $Cd_{33}Se_{33}$ QD ligated by trimethylphosphine oxide ($OPMe_3$) ligands suggests, a combination of B3LYP functional with LANL2DZ basis set predicts a reasonable Cd-Se bond length, ligand-QD binding energy, as well as optical gap of $Cd_{33}Se_{33}$ QD [80]. The same methodology is adopted to simulate $Cd_{33}Se_{33}$ QD/Ru(II)-Polypyridine nanocrystal composite, and show that, independent of dye's attachment, and the type and size of QD (CdSe, PbSe or ZnO of 1 or 2 nm in size), Ru(II) complex with neutral ligands, like bipyridines, introduces unoccupied orbitals near CB edge of QD, while occupied orbitals localized on Ru(II) ion are deep inside QD's valance band [29, 81]. Such energetic offset between dye's and QD's orbitals makes hole transfer from photoexcited QD to dye energetically unfavorable due to insufficient thermodynamic driving force, while tending toward electron transfer from photoexcited dye to QD.

Even though the ground-state calculations are well enough to predict the energetic levels, molecular orbitals as well as linear and nonlinear optical properties, such as surface trap states, linear absorption, multiple exciton generation efficiency, etc; it fails to predict charge transfer dynamics. Even though one can bypass such dilemma by applying Fermi's golden rule using the first-order perturbation approach to obtain the charge transfer rates, such approach highly depends on the coupling of nuclear vibrational modes with electronic states. At high temperature limit it assumes a weak coupling that only ground state is appreciably populated, which turns into the famous Marcus equation, while at low temperature limit only one or two high frequency vibrational modes are allowed to couple with electronic states in order to parametrize the nuclear Hamiltonian easily. On the other hand, it is still an open question to derive the electronic coupling term at the seam of adiabatic crossing region based on current approaches, due to the overestimation of electron delocalization between donor and acceptor molecules giving the errors when constructing diabatic states from adiabatic states, such as generalized Mulliken–Hush method (GMH) [82, 83], fragment charge difference [84], fragment energy difference [85], etc. Alternatively, the fragment orbital density functional theory (FODFT)[86] resolves such issue by approximating the diabatic wavefunction with a linear combination of fragment molecular orbitals (FMO), where either electron or hole is constrained in donor or acceptor molecule by dividing the whole system into fragments; however it misses the important electronic correlation between fragment molecular orbitals, thus only valid for the weakly coupled donor-acceptor system. As such, the approach beyond Born-Oppenheimer approximation and inclusion of electron-vibrational interactions into the theory, is promising to describe the charge transfer property across the heterogeneous interface providing instrumental information about the interfacial electronic interaction.

The most important part of resolving time-evolved electronic wavefunction is to couple electronic dynamics with nuclear motion, i.e. nonadiabatic molecular dynamics (NAMD). When such coupling is weak, the electronic dephasing prevails nuclear dissipassion dominating the photo-relaxation. Otherwise, the relaxation process is modulated by phonons. There are many available electronic dynamic approaches, such as real-time density functional theory [87, 88], mean-field molecular dynamics [89, 90], red-field theory [91], etc, among which Tully fewest switched surface trajectory hopping method [92] is one of the most common NAMD schemes and can be viewed as a quantum master equation for electron dynamics in which state-to-state transition rates depend on time through coupling to explicit vibrational dynamics, with a statistical average over trajectories. Such atomistic computational modeling of charge transfer is an established theory. However, several challenges remain (i) precision of electronic structure computations, (ii) the initial statistical distribution of electronic populations upon photoexcitation, and (iii) the accuracy of approximating excited-state trajectory with ground state trajectory. In chapter 7, we will explicitly discuss each of them.

1.3. Main Goals and Outline of the Dissertation

In this dissertation, we use density functional theory (DFT) as well as time-dependent DFT methods to investigate the dye functionalization effect on interfacial charge transfer as well as photorelaxation between QD and dye, which includes the metal ion, organic ligands as well as binding geometry of dye. In addition, we study the environmental effect of solvent on interfacial energetic alignment between QD and dye using DFT. At last, we use time-domain DFT in combining with Tully-surface hopping to study the charge-carrier relaxation and transfer processes in QD/dye nanocomposite. A such, this dissertation is organized as follows:

In chapter 2, we overview the theoretical backgrounds for Time-domain density functional theory (TDDFT), the embedded fragment potential model, the fewest-switches surface hopping (FSSH) algorithm as well as the charge-constrained DFT. In chapter 3, we elucidate how to construct the geometrical structures of QD/dye nanocomposite as well as the reasons of choosing the specific functionals and basis sets for the DFT calculations.

In chapter 4, we study the effect of metal ion on the energetic alignment between $Cd_{33}Se_{33}$ QD and $[Me(II)(bpy)_2(mcb)]^{1+}$ complex. First, we benchmark the amount of exact exchange in B3LYP functional with different percentages: 30%, 25% and 20%, respectively, to establish a reliable amount of exact exchange for predicting ground spin state of $[Me(II)(bpy)_2(mcb)]^{1+}$ complex. Subsequently, we project the total density of states onto QD and dye, respectively, to obtain the energetic alignment. For evaluating the QD-dye interaction, the whole nanocomposite is divided into fragment environmental region (QD) and *ab initio* molecular region (dye). Then, the embedded fragment potential model is used to approximate QD's electric field as multiple expansion terms included in dye's Hamiltonian. Afterwards, different interaction energies (dipole, quarupole, octupole, first hyperpolarizability) are extracted out of the embedding energy. At last, we study the photoexcited charge-transfer by calculating the charge density difference between ground state and excited state.

In chapter 5, we elucidate the effect of different ligands in the Ru(II)-complexes on the relative alignments of the energy levels associated with the QD and the dye by performing DFT and TDDFT calculations. We show that QD−dye interactions strongly stabilize dye electronic orbitals with respect to the QD states, compared to the energy offsets of the isolated QD and the dye. A negative charge on the ligands coordinated with the metal ion, like a thiocyanate ligand in the black dye, results in a shift of the orbitals originated from the complex toward the very edge

of the valence band of the CdSe QD, and makes the hole transfer more favorable. In addition, our calculations predict that a polar solvent can be used to tune the mutual alignment of the dye's and QD's orbitals in order to improve efficiency of the charge transfer. Thus, these results potentially facilitate rational design of organometallic dyes to better control the dye−QD interactions and, consequently, the photophysics of QDs via chemical functionalization.

In chapter 6, we study the electronic effect of binding geometry on energetic alignment as well as electronic coupling. First, we generally describe the binding configurations and electronic structures of $Cd_{33}Se_{33}$ QD/N719 dye composite. Then, we calculate the projected density of states (PDOS) to show the energetic alignment between QD and dye depending on the binding geometry. In addition, the ionization potentials are calculated to represent the HOMO levels of isolated dyes cut from different binding geometry. The effect of binding geometries of dye on electronic coupling is represented by the charge transfer integral, which is proportional to the charge transfer rate according to Fermi's golden rule, and approximately describes how fast the charge transfer occurs.[93] Additionally, we use the donor-acceptor wavefunction overlapping to characterize the strength of QD-dye interaction.

In chapter 7, we perform Tully-surface hopping scheme in combining with time-dependent Kohan-sham equation to determine the nuclear trajectory hopping between different electronic potential surface of $Cd_{33}Se_{33}$ QD/BD dye nanocrystal composite. The electronic dynamics is coupled with nuclear trajectory through calculating nonadiabatic coupling vector reflecting the time-evolved electronic relaxation process, i.e. relaxation dynamics. Through projecting the total density of states onto QD and dye, we obtain the time-evolved projected density of states as well as the time-evolved electron- and hole population dynamics in QD and dye, respectively.

CHAPTER 2. METHODS AND COMPUTATIONAL DETAILS

2.1. Effective Mass Approximation for Modelling Electronic Structure and Optical Properties of Quantum Dots

The effective mass approximation (EMA) is the simplest model that describes the electronic properties of QDs[94]. EMA assumes the electronic structure of QDs remains the same as in crystal structure, where the wavefunction vanishes at the dot boundary having a spherical shape. According to Bloch's theorem, the wavefunction in periodic bulk system can be written as

$$\Psi_{n\boldsymbol{k}}(\boldsymbol{r}) = u_{n\boldsymbol{k}}(\boldsymbol{r}) \exp(i\boldsymbol{k}\cdot\boldsymbol{r}) \tag{2.1}$$

where $u_{n\boldsymbol{k}}(\boldsymbol{r})$ is a periodic function that repeats along lattice vector direction. $\boldsymbol{k}$ is the wavevector, and n is the index of the band. Under such approximation the bands of QDs can be assumed as simplified parabolic shape, which is a proper approximation in CdX (X=S, Se, Te) QDs[95] with conduction band edge and valence band edge occurring at $\boldsymbol{k}$=0. The wavefunction of QD can be represented as a linear combination of Bloch functions.

$$\Psi_n(\boldsymbol{r}) = \sum_{\boldsymbol{k}=-\frac{\pi}{a}}^{\boldsymbol{k}=\frac{\pi}{a}} C_{n\boldsymbol{k}} u_{n\boldsymbol{k}}(\boldsymbol{r}) \exp(i\boldsymbol{k}\cdot\boldsymbol{r}) \tag{2.2}$$

where a is the radius of QD.

As the size of QD is finite, $u_{n\boldsymbol{k}}$ has a weak dependency on $\boldsymbol{k}$. The eqn.(2.2) can be written as

$$\Psi_n(\boldsymbol{r}) = u_{n0}(\boldsymbol{r}) \sum_{\boldsymbol{k}} C_{n\boldsymbol{k}} \exp(i\boldsymbol{k}\cdot\boldsymbol{r}) = u_{n0}(\boldsymbol{r}) f_n(\boldsymbol{r}) \tag{2.3}$$

$$f_n(\boldsymbol{r}) = \sum_{\boldsymbol{k}} C_{n\boldsymbol{k}} \exp(i\boldsymbol{k}\cdot\boldsymbol{r}) \tag{2.4}$$

where $f_n(\boldsymbol{r})$ is the single-particle envelope function. Envelope function governs the superposition of Bloch functions with expansion coefficient satisfying the spherical boundary condition of the QD. With EMA the hole and electron wavefunction can be represented by a periodic Bloch wavefunction and an envelope function.

Both linear and nonlinear properties of small QDs are caused by the size confinement effect that determines the optical transitions between hole and electron quantized energetic levels. At the surface of the QD it requires that electron and hole wavefunctions vanishing at the dot boundary. Under such boundary condition with parabolic approximation, the quantized energy levels can be characterized by the *n*th root of the spherical Bessel function of order *l*, i.e. $\phi_{l,n}$. Spherical Bessel function is obtained by separating the radial part from the wavefunction, and assuming an infinite spherical well. Under such condition, the solution to the radial part is Bessel function. The quantized energetic levels are given as[96]

$$E_{l,n}^{e,h} = \frac{\hbar^2 \phi_{l,n}^2}{2m_{e,h}a^2} \tag{2.5}$$

where $m_{e,h}$ is the effective mass for electron and hole, respectively. a is the crystal radius. $\phi_{1,0} = \pi$, $\phi_{1,1} \approx 1.43\pi$, $\phi_{2,1} \approx 1.83\pi$. However, it has to be taken into account the coulomb interactions that exist between electrons and holes, since the exciton effect or electron-hole interaction ($\iint \frac{\varphi_e(r_1)\varphi_h(r_2)}{4\pi\epsilon(r_1-r_2)} dr_1 dr_2$) in QD is stronger than bulk due to electron-hole pair confined in a much smaller space in QD than bulk, i.e. $|r_1 - r_2|_{QD} < |r_1 - r_2|_{bulk}$. In addition, the shielding in QD is much smaller than bulk further increased its exciton effect.

As such, the ratio of the nanocrystal radius (a) to the exciton Bohr radius (a_B) of the bulk exciton determines the confinement regime as well as the optical properties. a_B is the exciton bohr radius. Bohr exciton radius can be used to estimate the most probable distance between a

photoexcited electron and a photoexcited hole[97]. According to the effective mass, and then the ratio of nanocrystal radius to exciton Bohr radius ($a_B = \frac{h^2\epsilon}{2\pi\mu e^2}$, where μ is the effective mass and $\frac{1}{\mu} = \frac{1}{m_e} + \frac{1}{m_h}$), the confinement has three categories: weak confinement regime, intermediate confinement regime and strong confinement regime.

At the weak confinement regime, i.e. $a \gg a_B$, the binding energy of an exciton, E_{ex}, is larger than quantized energies for electrons and holes, as such, the ground state energy is given by[98]

$$\hbar\omega = E_g - E_{ex} + \frac{\hbar^2\pi^2}{2Ma^2} \tag{2.6}$$

where E_g is the bulk semiconductor energy gap, and $M = m_e + m_h$ is the exciton translation mass.

At the intermediate confinement regime[96], i.e. $a_e > a > a_h$, where $a_e = \epsilon\hbar^2/m_e e^2$ and $a_h = \epsilon\hbar^2/m_h e^2$ are the Bohr radius of electrons and holes, respectively. ϵ is the dielectric constant of the semiconductor. At the intermediate confinement regime, the effective mass of hole is larger than electron ($a_e > a_h$), the hole is localized in the center of nanocrystal subjecting the averaged potentials due to a much faster movement of electrons. In such regime, the exciton oscillates around the center of nanocrystal.

At the strong confinement regime, i.e. $a \ll a_B$, the optical transitions between electrons and holes are determined by the quantized energy levels in valence band and conduction band, respectively. Therefore, the ground state energy is given by[99]

$$\hbar\omega_v = E_g + E_v^h(a) + E_v^e(a) - 1.8\frac{e}{\epsilon a} \tag{2.7}$$

where the last term is coulomb corrections to the band gap of bulk, which is a much smaller quantity than the sum of first three terms. Therefore, one can apply first order perturbation theory

to obtain the correction term. E_v^h and E_v^e are hole and electron energies as shown in eqn.(2.5). At the strong confinement region where the nanocrystal radius much smaller than Bohr radius, the electron and hole of QD can be treated as independent charge carriers with an effective mass m_{e^*} and an effective mass m_{h^*}, respectively, due to a much smaller coulomb interaction than quantized energy levels. The confinement energy is scaled as $(1/a)^2$ while the coulomb interaction between electron and hole is scaled as $1/a$. Therefore, the quantum confinement effect dominates, and under the zero-order approximation the exciton states are expressed as the product of electronic state and hole state. The exciton wavefunction can be written as

$$\Psi(r_e, r_h) = \Psi_e(r_e)\Psi_h(r_h) \tag{2.8}$$

Since Envelope function describes the motion of electrons and holes in an QD confinement potential, and is given by the solution of a particle in an infinite spherical potential well, it can be written as the product of a spherical Bessel function and a spherical harmonic function. Therefore, substituting eqn.(2.3) into the eqn.(2.8)[100]

$$u_{n0}(r)f(r) = C_{nk}\left(u_c \frac{j_{L_e}\left(k_{n_e,L_e} r_e\right)Y_{L_e}^{m_e}}{r_e}\right)\left(u_c \frac{j_{L_h}\left(k_{n_h,L_h} r_h\right)Y_{L_h}^{m_h}}{r_h}\right) \tag{2.9}$$

where j_{L_e} and j_{L_h} are the L-th order spherical Bessel functions for hole and electron[100], respectively. $Y_{L_e}^{m_e}$ and $Y_{L_h}^{m_h}$ are spherical harmonic functions for hole and electron[101], respectively, where m_e or m_h is magnetic quantum number, and L_e or L_h is orbital angular momentum[101].

The theoretical works are benefitted from the fact that optical transitions originate from quantized energy levels. This brings a great convenience to model the excited-state dynamics of $Cd_{33}Se_{33}$ QD for our study, which allows us to determine the initial excitation conditions for electron and hole, and as well as propagating their populations, respectively, based on the quantized energy levels in valence band and conduction band with single particle Kohn-sham

approach[23]. This also implies the nuclear trajectory with excited-state potential can be approximated by employing the ground-state potential constructed by the quantized Kohn-sham energy levels.

In the early works the effective mass model is used to explain the experimental measurements of electronic structure[102, 103] and absorption spectra[104, 105] of nanocrystals. In more recent works, this model has been extended to explain the band structures of direct band-gap semiconductor[106] and two-dimensional materials[107, 108]. In addition, the effective mass model is used to explain the multiple exciton generation[109, 110] in CdSe and PbSe QDs as well as linear and nonlinear properties of core/shell structure QD[111]. Moreover, the effective mass model is sensitive to the size of the nanocrystal. It is found, the effective mass model is failed for CdS nanocluster when the size is smaller than 20 Å in diameter[112].

Effective mass model only considers the QD as an ideal sphere, which allows for finding the electron and hole wavefunctions with spherical potential that is vanished at the dot boundary. However, the surface states of QD no longer retain the original lattice structure due to the surface reorganization and capping ligands, which introduces the surface trap states that appear as the dark exciton states in optical spectra. The Schordinger solutions of those localized, surface trap states are beyond the scope of effective mass model. In addition, the surface trap states also change the energetic positions of conduction and valence band edges of QD[113], which determine the charge transfer direction, therefore the effective mass model is failed for describing the interfacial charge transfer. The models that include atomistic information and can introduce surfaces, including defects etc. is needed for reasonable description of effects taking place at the QD's surfaces and interfaces.

2.2. Using Density Functional Theory in the Calculations of Nonadiabatic Couplings

Since its first foundation in mid-1960's [114, 115], Density Functional Theory (DFT) has rapidly developed into a powerful tool for predicting the ground state properties of materials. Rather than dealing with very complicated many body wavefunctions which depends on the coordinates of all electrons in molecules, DFT adopts a simplification by assuming the existence of a non-interacting ideal electron gas which shares the same electron density as the real system has. Thus, DFT greatly reduces the computational cost through mapping many-body real system into a fictitious system with only one spatial variable. i.e. one electron density system. This greatly reduces the computational cost required to solve many body problem, as such, it is now possible to predict the ground state properties of materials in condensed phase. The development of time-dependent Kohn-sham theory (TDKS) is more tricky than DFT. In DFT formalism one minimizes the total energy corresponding to the time independent ground state, thus obtaining the stationary solution with respect to one electron density, whereas the stationary solution of TDKS is not only dependent on the spatial coordinates of electrons but also the electron densities existed in the future and the past. As such, one can define a quantum mechanical action [116]:

$$\mathcal{A}[\Psi] = \int_{t_0}^{t_1} \left\langle \Psi(t) \middle| i\frac{\partial}{\partial t} - H(t) \middle| \Psi(t) \right\rangle dt \tag{2.10}$$

Through minimizing the energy functional $\mathcal{A}[\Psi]$ with respect to wavefunction $\Psi[t]$, it yields time-dependent Schordinger equation:

$$i\hbar\frac{\partial|\Psi(t)\rangle}{\partial t} = H|\Psi(t)\rangle \tag{2.11}$$

In our simulation presented here, the generalized gradient approximation (GGA) is employed, so that *H* can be expressed as the functional of electron density and its gradient [117]:

$$H = -\frac{\hbar^2}{2m_e}\nabla^2 + V_N(x) + e^2\int\frac{\rho(x')}{|x-x'|}d^3x' + V_{xc}[\rho, \nabla\rho] \quad (2.12)$$

where electron density ρ is written in Kohn-sham representation [117, 118] as:

$$\rho(x,t) = \sum_{p=1}^{N_e}|\varphi_p(x,t)|^2 \quad (2.13)$$

Applying variational principle to Kohn-sham energy which is written as

$$E[\varphi_p] = \sum_{p=1}^{N_e}\langle\varphi_p|K|\varphi_p\rangle + \sum_{p=1}^{N_e}\langle\varphi_p|V|\varphi_p\rangle + \frac{e^2}{2}\iint\frac{\rho(x',t)\rho(x,t)}{|x-x'|}d^3xd^3x' + E_{xc}[\rho] \quad (2.14)$$

Then it yields single-particle equation of motion for the KS orbitals[119-121]

$$i\hbar\frac{\partial\varphi_j(x,t)}{\partial t} = \mathcal{H}\varphi_j(x,t), j = 1,2,\dots\dots\dots, N_e \quad (2.15)$$

The right-hand side of Eqn. 2.14 gives the kinetic energy of noninteracting electrons, the electron nuclear attraction, the Coulomb repulsion of density *ρ(x, t),* and the exchange-correlation energy functional that accounts for the residual many-body interactions. The time-dependent $\varphi_p(x,t)$ can be expanded in adiabatic KS orbitals $\tilde{\varphi}_k(x;R)$

$$\varphi_p(x,t) = \sum_{k=N_1}^{N_2}c_{pk}(t)\,|\tilde{\varphi}_k(x;R)\rangle \quad (2.16)$$

Substituting Eqn. 2.16 into Eqn. 2.15, then TDKS Eqn. 2.15 is transformed into time-dependent equation of motion for the coefficients.

$$i\hbar\frac{\partial}{\partial t}c_{pk}(t) = \sum_{m}^{N_e} c_{pm}(t)(\varepsilon_m\delta_{km} + d_{km}\cdot\dot{\boldsymbol{R}}) \tag{2.17}$$

The NA coupling

$$d_{km}\cdot\dot{\boldsymbol{R}} = -i\hbar\langle\tilde{\varphi}_k(x;R)|\nabla_R|\tilde{\varphi}_m(r;R)\rangle\cdot\dot{\boldsymbol{R}} = -i\hbar\left\langle\tilde{\varphi}_k\middle|\frac{\partial}{\partial t}\middle|\tilde{\varphi}_m\right\rangle \tag{2.18}$$

NA coupling term can be numerically solved by overlapping molecular orbitals derived through Taylor expansion.

$$d_{km}\cdot\dot{\boldsymbol{R}} \approx -\frac{i\hbar}{2\Delta t}(\langle\tilde{\varphi}_k(t)|\tilde{\varphi}_m(t+\Delta t)\rangle - \langle\tilde{\varphi}_k(t+\Delta t)|\tilde{\varphi}_m(t)\rangle \tag{2.19}$$

Then, coefficients are solved via second-order differencing [122]

$$c_k(t+\Delta t) = c_k(t-\Delta t) - \frac{2i}{\hbar}\Delta t\sum_{m} c_m(t)(\epsilon_m\delta_{km} + d_{km}) \tag{2.20}$$

To simulate photoexcited dynamics in QD/dye nanocomposites, we use our homemade phonon-assisted non-adiabatic molecular dynamics (NAMD) codes to model electron or hole transfer upon photoexcitation facilitated by thermalized phonons. As such, inclusion of non-

adiabatic (NA) couplings is required, which a challenge for modern computations. To address this challenge, we apply several approximations, including classical trajectories, ground state density, etc, on the basis of the single-particle Kohn-Sham orbitals, allowing us to obtain electron-phonon NA couplings for the extended and complicated systems we study. We apply Tully's trajectory surface hopping technique to study electronic dynamics. In addition, we adopt a site-projected wave function procedure "on the fly" together with the calculation of NA couplings. In this way, the electron density is projected onto different part of the system and a map of time-evolved electron density located at different parts of QD/dye will be obtained, providing a description of charge carriers migrated from one part of system to another part as a function of time. Our computational insight reveals the elementary information about the charge transfer dynamics across the heterogeneous interface in QD/dye composite that cannot be directly accessed in experiments.

2.3. Trajectory Surface Hopping (TSH)

Quantum mean field theory (QMFT) assumes nuclear trajectories evolve along the average electronic potential surfaces. As such, each nuclear trajectory does not have a specific correlation with specific electronic state. In other words electron densities are spread over the entire nuclear trajectory space to feel the average coulomb potentials. Such approximation is satisfactory in modelling weakly correlated electron-nuclear system, in which nuclear motion and electronic dynamics can be treated as two independent systems; however it gives erroneous results when there exists a strong correlation between nuclear and electron, e.g. molecular and atomic scattering, non-radiative electron-nuclear relaxation, and current-induced heating in molecular electronics [123-128]. Trajectory surface hopping is designated to address this problem. Rather than evolving nuclear trajectories along the average of electronic potential surfaces, a particular electronic state is

stochastically determined to steer the nuclear trajectory. As a result, a probability distribution of nuclear trajectory ensemble is formed with stochastically determined hopping from one electronic potential surface to another one. There are many different kinds of surface hopping techniques developed so far, among which fewest trajectory surface hopping is the most popular one. Fewest-switches surface hopping is a method established on electronic states with nuclear trajectory hopped between the states. When the adiabatic state is chosen to be the electronic basis, the atomic forces for ground- and excited-electronic states as well as the NA coupling between the electronic states can be calculated on the fly. To extend our method to large-scale condensed phase modeling we adopt further approximation by representing many-particle wavefunction with one-particle wavefunction, which is suited for studying QDs whose electronic structure is well represented by the independent electron and hole picture. We also noted, CdSe QD is a wide gap semiconductor nanocrystal, where the optical gap is governed by the quantized energy levels rather than the coulomb interaction. As a result, the optical absorption is well described by Kohn-Sham spectra that is based on the single-particle formalism.

The hopping probability between the electronic state k and m within time interval *dt* equals

$$dP_{km} = \frac{b_{km}}{a_{kk}} dt \tag{2.21}$$

Where

$$b_{km} = -2Re\left(a_{km}^{*}\boldsymbol{d}_{km} \cdot \dot{\boldsymbol{R}}\right); \qquad a_{km} = c_k c_m^{*} \tag{2.22}$$

Here, c_k and c_m are the coefficients defined in eqn.(2.17). If the calculated dP_{km} is negative, the hopping probability is set to zero. As such the number of hops is greatly reduced, i.e. a hop that increases the population of upper state will never occur. In addition, in order to conserve the total

energy, the nuclear velocities are rescaled along the direction of NA coupling $\boldsymbol{d}_{km}$ [92, 125]. if a NA transition to a higher energy electronic state is predicted by eqn.(2.21), and the kinetic energy of nuclear along the direction of NA coupling is insufficient to accommodate the increase in electronic energy, the hop is rejected. As such, the velocity-rescaling and hop-rejection give detailed balance between upward and downward transitions [124]. However, the practical implementation of such algorithem requires the calculation of NA coupling along with propagation of nuclear trajectory in order to provide the driving force for nuclear coordinate, and requiring a lot of computational resources. To simply the procedure, we assume the energy exchange between the electronic and selected nuclear degree of freedom during the hop is rapidly redistributed between all nuclear modes. Therefore, it is reasonable to treat the distribution of energy in the nuclear mode along NA coupling as Boltzmann at all times, as such, the velocity-rescaling as well as hop-rejection can be replaced by multiplying eqn.(2.21) by the bolzmann factor - $e^{-\frac{\Delta E}{kT}}$, which saves computational cost, and avoids the quantum back-reaction, allowing one to use a predefined nuclear trajectory to evolve the electronic subsystem.

2.4. Charge-constrained Density Functional Theory and Electronic Coupling

Long range charge transfer interaction has received increased attention for its applications in biological system and molecular electronics [129]. Usually such charge transfer is weak and nonadiabatic. When two adiabatic surfaces approach each other, the electron is transferred from donor molecule to acceptor molecule. According to Marcus theory [130], three important parameters determine the charge transfer rate, i.e. the driving force (ΔG), the reorganization energy (λ), and electronic coupling vector (H_{ab}). The rate constant is given as

$$k = \frac{2\pi}{\hbar} H_{ab}^2 \times DOS \tag{2.23}$$

Where the *DOS* is the density of states weighted Frank-Condon factor. The Frank-Condon factor can be written as

$$FC = \sum_{v'=0}^{\infty} \sum_{v=0}^{\infty} S_{v',v}^2 \tag{2.24}$$

Here $S_{v',v}^2$ is the nuclear overlapping term.

There are many efforts in developing the techniques to solve the electronic coupling vector, such as perturbation theory [131], Green function [132], etc. They can be generally classified into four groups: (1) seeking minimum adiabatic state splitting determined through Koopman's theorem [133]; (2) self-consistent field energy difference with external perturbations [134], and (3) those depend on diabatic state [82]. However, all of these methods depend on the accuracy of wavefunction in describing the configuration, therefore, one has to face the dilemma of choosing the simplified Hartree-Fock (HF) method, which misses the important electron correlation, since more accurate methods, such as configuration interaction (CI), are too expensive for many system of interest.

The emergence of DFT complements the weakness of wavefunction based methods. Even though there is no corresponding Koopman's theorem in DFT, on top of that, the Kohn-sham wavefunction does not have any physical meaning, it has been successfully applied to GMH method [135] and the fragment orbital density functional theory (FODFT) [86, 136] to calculate the electronic coupling vector. The former one relies on adiabatic energies, dipole moments as well as transition dipole moments as input quantities, while the latter one constructs the diabatic wavefunction based on fragment molecular orbitals.

The constrained DFT method provides accurate description of long-range CT states [137, 138]. Through optimizing the geometry of constrained system, it is possible to obtain the inner sphere reorganization energy and electronic coupling vector. The basic idea of constrained DFT is to find

an effective potential that corresponding to the charge-localized states by adding the density constrain, i.e., $\int w_c(r)\rho_c(r)dr = N_c$, where $w_c(r)$ is the operator that defines the property of interest. There exists a unique potential corresponding to particular constrained state, therefore the wavefunction satisfies

$$(H + V_c w_c)|\Psi_c\rangle = F|\Psi_c\rangle \tag{2.25}$$

and

$$F = \langle\Psi_c|H + V_c w_c|\Psi_c\rangle = E[\rho_c] + V_c \int w_c \rho_c = E + V_c N_c \tag{2.26}$$

With such functional one can obtain the charge-constrained equilibrium geometry. To construct the diabatic wavefunctions Ψ_A and Ψ_B one has to use HF wavefunction that has physical meanings.

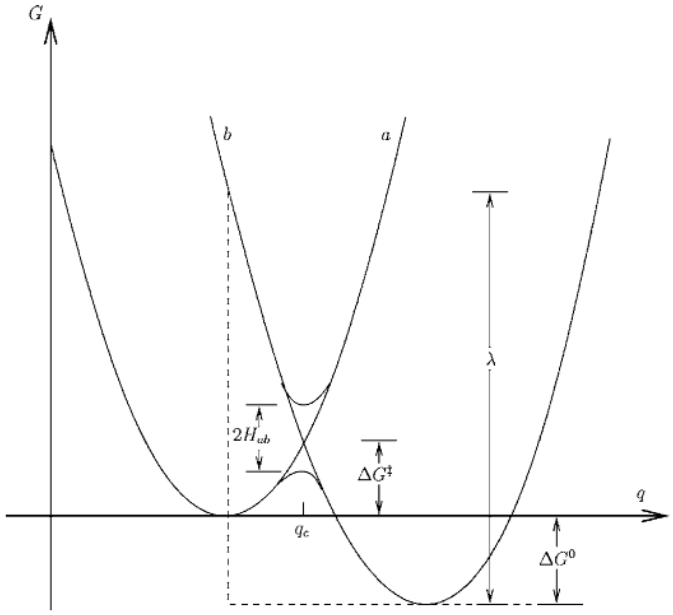

Figure 4. Potential energy curves of an electron transfer reaction. q represents the reaction coordinate [137].

At the crossing of adiabatic surfaces (Figure 4) the splitting can be obtained by solving the secular equation

$$\begin{vmatrix} H_{AA} - E & H_{AB} - ES_{AB} \\ H_{AB} - ES_{AB} & H_{BB} - E \end{vmatrix} = 0 \quad (2.27)$$

Where $S_{AB} = \langle \Psi_A | \Psi_B \rangle$, $H_{AA} = \langle \Psi_A | H | \Psi_A \rangle$, $H_{BB} = \langle \Psi_B | H | \Psi_B \rangle$, and E is the energy eigenvalue. Hence, the separation between adiabatic upper- and lower potential surfaces is [139]

$$\Delta(Q) = E_+ - E_-$$

$$= 2(1 - S_{AB}^2)^{-1} \left\{ \frac{1}{4}(H_{AA} - H_{BB})^2 - (H_{AA} + H_{BB}) H_{AB} S_{AB} + H_{AA} H_{BB} S_{AB} + H_{AA} H_{BB} S_{AB}^2 \right.$$

$$\left. + H_{AB}^2 \right\}^{\frac{1}{2}} \quad (2.28)$$

Where E_+ is upper root of potential surface and E_- is the lower root of potential surface. The half value of separation evaluated at the seam of the crossing where $H_{AA} = H_{BB}$, is designated by V_{AB}

$$V_{AB} = (1 - S_{AB}^2)^{-1} \left[H_{AB} - \frac{S_{AB}(H_{AA} + H_{BB})}{2} \right] \quad (2.29)$$

In FODFT approach, the kohn-sham determinants Ψ_A and Ψ_B are constructed from isolated donor and acceptor fragments [86]

$$\Psi_A^{DA} = \frac{1}{\sqrt{(2N+1)!}} \det(\phi_D^1 \dots \phi_D^{N+1} \phi_A^1 \dots \phi_A^N) \quad (2.30)$$

$$\Psi_B^{DA} = \frac{1}{\sqrt{(2N+1)!}} \det(\phi_D^1 \dots \phi_D^N \phi_A^1 \dots \phi_A^{N+1}) \quad (2.31)$$

Where N is the number of electrons for donor state and acceptor state. Through eqn.(2.29) one can obtain H_{AB}.

2.5. Embedded Fragment Potential Model

Embedded fragment potential model is specifically designed to describe the environmental effect, primarily aimed for describing the cluster behavior as well as the interaction between cluster and solute molecule, while the solute is not explicitly treated in ab initio quantum mechanical level.

It contains terms that represent [140] (a) coulombic interactions between solvent molecules and each other, or the ab initio solute. (b) solvent-solvent and solvent-solute interaction or polarization interactions, and (c) exchange and other repulsion terms. The first two terms can be generated through ab initio calculations stored for future use, while the third term can be generated through some fitting procedure. The Hamiltonian for the entire system can be divided by the ab initio region and environmental region

$$H = H_{AR} + V \tag{2.32}$$

Where H_{AR} is ab initio Hamiltonian, and V represent the potential due to the environment, corresponding to electrostatic, polarization, and exchange repulsion interaction. The effective fragment interaction Hamiltonian V that representing the interaction between μth solvent molecule and an electron in the ab initio region is given as [140]

$$V_{el}(\mu, s) = \sum_{k=1}^{K} V_k^{Elec}(\mu, s) + \sum_{l=1}^{L} V_l^{Pol}(\mu, s) + \sum_{m=1}^{M} V_m^{Rep}(\mu, s) \tag{2.33}$$

Where the three terms represents electrostatic, polarization and exchange-repulsion interactions. In addition, there are similar terms added to represent the interaction between nuclei in ab initio region and fragment molecule and fragment-fragment interaction. The solute is treated explicitly with ab initio wavefunction, while the fragment molecule is treated as environment that interacts with solute.

The electrostatic potential can be obtained through performing multipole analysis of the fragment charge distribution. K in eqn. (2.33) is the expansion point.

$$V_k^{Elec}(\mu, s) = \frac{q_k(\mu) q_s}{r_{sk}} - \sum_a^{x,y.z} \mu_a^k(\mu)\, F_a(r_{sk})$$

$$- \frac{1}{3} \sum_{a,b}^{x,y,z} \Theta_{ab}^k(\mu) F_{ab}(r_{sk}) - \frac{1}{15} \sum_{a,b,c}^{x,y,z} \Omega_{a,b,c}^k(\mu) F_{a,b,c}(r_{sk}) \quad (2.34)$$

where q, μ, Θ and Ω are the charge, dipole, quadrupole and octopole, respectively, and F_a, F_{ab} and F_{abc} are the solute electric field, field gradient and field Hessian. In order to account for the overlap of electron densities when molecules approach each other, eqn. (2.34) is multiplied by a distance-cutoff function,

$$V_k^{Elec}(\mu, s) = \left(1 - \beta_k(\mu) e^{-\alpha_k(\mu) r_{sk}^2}\right) V_k^{Elec}(\mu, s) \quad (2.35)$$

The polarization term is treated with self-consistent perturbation approach by employing the localized MOs. Bond and lone pair localized orbital dipole polarizabilities can be derived from finite-field Hartree-Fock calculations of isolated molecule.

The exchange-repulsion term is modelled by one-electron terms in ab initio Hamiltonian which have the form of Gaussian functions located at the fragment atom centers and the center of mass[140].

$$V_m^{Rep}(\mu, s) = \sum_j^J \beta_{mj}(\mu) e^{-\alpha_{mj}(\mu) r_{ms}^2} \quad (2.36)$$

The Gaussian functions are optimized by fitting procedure, in which the ab initio exchange-repulsion term is obtained by subtracting the sum of electrostatic plus polarization energies from the local potential to obtain the term $E_{rem}^{(ab)}$. Then, V_m^{Rep} is fitted to $E_{rem}^{(ab)}$ [140].

$$\Delta = \sum_p^P w_p [\langle \Psi | \sum_m^M V_m^{Rep} | \Psi \rangle_p - E_{rem}^{(ab)}(p)]^2 \quad (2.37)$$

where w_p is a weighting factor. Ψ is the ab initio wave function. The fragment-fragment interactions are treated with a single exponential instead of Gaussian functions.

CHAPTER 3. MODELLING THE STRUCTURES AND SURFACES OF DYE FUNCTIONALIZED QDs

3.1. Geometries of $Cd_{33}Se_{33}$ QD

We start with the construction of roughly spherical, "magic" size $Cd_{33}Se_{33}$, and in addition $Cd_{111}Se_{111}$ cluster is also constructed for comparison (Figure 5).

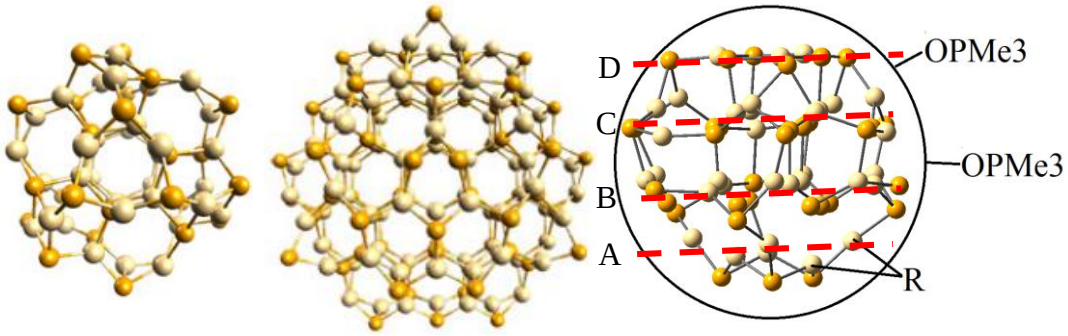

Figure 5. $Cd_{33}Se_{33}$ QD (left), $Cd_{111}Se_{111}$ QD (middle), and ligated $Cd_{33}Se_{33}$ QD (right).

Both clusters have the Wurtzite crystal symmetry and diameters of about 1.5 and 2.2 nm, respectively, in accordance to the procedure reported in the literature [23, 75, 80]. Geometries of QDs are cut from Wurtzite CdSe bulk [141], and optimized along with dye complex attached to the surface using the broken symmetry DFT. Wurtzite unit cell is the most stable structure in its natural form of CdSe bulk[142]. After geometry optimization, Cd atoms move outwards comprising the first layer of QD, while Se atoms move inwards comprising the second layer of QD. Core of QD remains the wurtzite crystal structure as bulk, and contains 6 Cd atoms and 6 Se atoms. Each Cd is coordinated with 4 Se with tetrahedral shape. Each Se is coordinated with 3 Cd with trigonal pyramidal shape. At the surface each Cd is coordinated with 3 or 4 Se with trigonal planar or tetrahedral or trigonal pyramidal shape. Each Se is coordinated with 3 or 4 Cd with tetrahedral or trigonal pyramidal shape. The $Cd_{33}Se_{33}$ "magic" structure has been experimentally shown to be stable [143], while it is

the smallest cluster that supports a crystalline-like core of the QD [144]. We choose the magic sized QDs for two reasons: first, the quantum confinement in magic sized QDs is much stronger than ~3 nm QDs making it an instrumental material for studying the charge transfer efficiency under the strong quantum confinement; second, the dipole moment in magic sized QD is exceptionally larger than its crystal form, which is comparable or even stronger than the dye [5], increased the intermolecular electronic coupling. On the other hand, for larger semiconductor nanocrystals (diameter > 3 nm) the QD-QD interaction and resonance energy transfer prevail the electronic coupling dominating the charge transfer efficiency [31, 145-148]. To this end, the magic sized QDs is the most idealized material to study the interfacial charge transfer governed by the quantum confinement and electronic coupling. Moreover, Changing the metal ion, organic ligands as well as binding geometry of dye have a main effect of tuning the energetic alignment of dye with respect to the QD. In particular, the binding geometry of dye, which has an important role in the dipole interaction, perturbs the energetic alignment, and changes the orbital interactions as well as the spectra overlap accordingly, resulting in different charge transfer efficiency [57].

Our larger $Cd_{111}Se_{111}$ model is even closer to the typical size of QDs in experimental samples. In fact, colloidal CdSe QDs with the average grain diameter of 1.84 - 2.27 nm, which have an efficient light emission at the wavelength of 500 - 560 nm, were recently synthesized and investigated. However, they are limited in only the ground state calculations of this system due to its large size. The $Cd_{111}Se_{111}$ model is only used to study the quantum confinement effect on band gap, discussed in chapter 5, while $Cd_{33}Se_{33}$ QD is the main model used for studying the dye functionalization effect on interfacial energetic alignment and charge transfer.

3.2. Geometries and Attachments of Dye Complexes

Here, we study three types of dye complexes, $[Me(II)(bpy)_2(mcb)]^{1+}$ dye, black dye and N719 dye, attached to the surface of $Cd_{33}Se_{33}$ QD, respectively, as shown in Figure 6. $[Me(II)(bpy)_2(mcb)]^{1+}$ dye is used for studying the effect of metal ion on interfacial energetic alignment. Black dye is used for studying the effect of ligands on interfacial energetic alignment as well as photorelaxation dynamics and interfacial charge transfer. N719 dye is used for studying the effect of binding geometry on interfacial energetic alignment as well as electronic coupling.

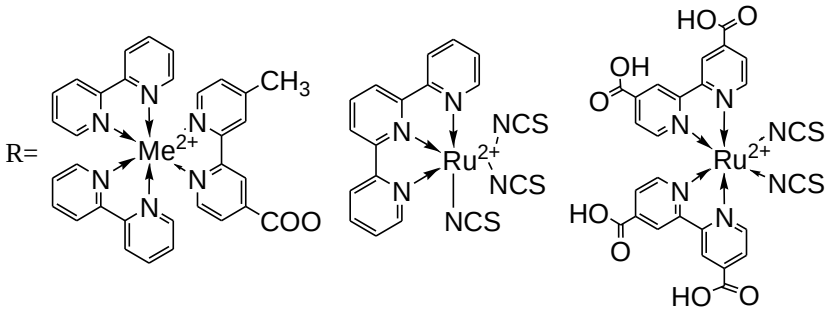

Figure 6. Schematic structures of [Me(II)(bpy)2(mcb)]1+ (left), Black dye (middle), and N719 dye (right).

All complexes are attached to the most chemically reactive surface {1 1 1 1} (here called the A surface) of the QD (Figure 5), where all surface cadmiums are 2-coordinated, as discussed in previous reports [80]. For a metal complex with carboxylic acid linker three types of linkages are available: bidentate (or bridging), unidentate and chelation.[39, 59, 149, 150] Previous calculation shows the bridging attachment of Ru(II)-Polypyridine dye on QD's surface gives the most stabilized energetic configuration for the QD/dye composite[81]. Therefore, in this study all $[Me(II)(bpy)_2(mcb)]^{1+}$ complexes are bridged on QD's surface *via* carboxylic acid linker (Figure 7 (a)). Bridging attachments of the complex at the different surfaces of the CdSe cluster have been also considered, and discussed in chapter 5. While multiple Ru(II) polypyridine complexes can be

adsorbed on a single QD [41], here we have to reduce our model to one adsorbed dye molecule on the QD surface to manage the computational cost. Thus, inter-dye interactions that are possibly present in the real systems are not taken into account in our models. However, our calculations allow us to include the effect of small capping ligands typically present at the QD surface. For this, we have fully passivated the surface of the CdSe cluster by trimethylphosphine oxide (OPMe3) molecules, which are known as a reasonable reduced model [151] for trioctylphosphine oxide (TOPO) ligands commonly used with colloidal CdSe QDs. While the question of the Ru(II) complex binding to the QD surface has been already investigated in detail [41, 81], here we focus on the role that a specific ligand coordinated with a Ru(II) ion in the dye plays on the electronic structure and optical properties of the QD/dye composites.

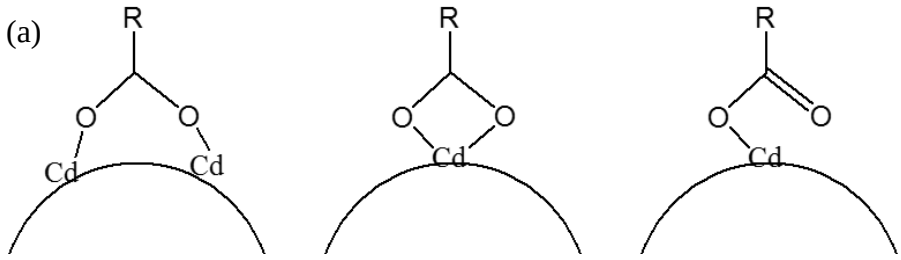

Figure 7. Three attaching modes of carboxylate anchor on the surface of QD, the bridging (a), unidentate (b) and chelation (c).

3.3. Computational Methods

3.3.1. Ground state and optical property calculations of the QD/dye composites

Computational modeling based on DFT and TDDFT has already been shown as a reliable tool in studies of interactions between QDs and various molecules adsorbed on the QD surface [81, 152, 153], providing important insights on the role of surface ligands in radiative [141, 154] and nonradiative [64, 155] photoexcited processes of CdSe QDs. Previous joint experimental and DFT studies [40] have determined the mechanism of attachment of Ru(II)bpy to the CdSe QD surface,

elucidating the exclusive attachment of the complex to the Cd sites of the QD surface via a bridging geometry, with the carboxylic anchoring group on the bipyridines being deprotonated in the process.

All QD-complex composites together with isolated pristine QDs and Ru(II) complexes are optimized to their lowest energy configurations at the DFT level of theory as implemented in the Gaussian-09 software package [156]. We utilize the LANL2DZ/6-31G* mixed basis set, where the LANL2DZ basis set is applied to heavy Ru, Cd, and Se atoms and the 6-31G* basis set is assigned to the rest of the atoms of the ligands. According to previous investigations, this combination of functional and basis set provides a reasonable description of the structures and QD-ligand binding energies [80, 157]. Overall, the increase in the basis set and inclusion of polarization functions have a minor effect on the electronic structure of composites. We have compared the performance of the LANL2DZ/6-31G* basis set (used in the paper for all compounds) with the more extended Def2TZVP basis set, and found an insignificant effect of the increased basis set on both ground state and excited state properties of the complex 1a, as well as on those of the QD/1a composite. In previous reports [80], the effect of the basis set with and without polarization functions on the CdSe QDs passivated by ligands is also investigated. No significant effect was observed on the electronic and optical properties of the systems, except for the absolute values of the ligand-QD binding energies.

Incorporation of long-range corrections to the hybrid functional is important for a more appropriate treatment of electronic states with possible charge transfer character, which are typical in metal−organic complexes [158, 159]. For example, utilization of the CAM-B3LYP[160] functional results in a decreased number of lower-energy dark states in PbSe and ZnO QDs functionalized by Ru(II)bpy, due to eliminating the well-known problem of "artificial" charge transfer states [81]. On

the other hand, long-range corrected functionals are known for their overcorrecting nature of the exciton interactions resulting in optical transition energies of QDs systematically blue-shifted compared to the reference [161]. It is known that the portion of the HF exchange used in the functional changes the gap: the larger the HF portion, the larger the gap. In other words, tuning the HF portion in the functional, one can adjust the calculated gaps to the experimental ones. Despite a blue shift in the energy due to high portion of the HF exchange, CAM-B3LYP functional has been shown [81] to provide qualitatively similar results to hybrid functionals such as PBE0 and B3LYP, which are able to accurately describe optical gaps of individual CdSe QDs [161-163] and Ru(II)bpy complexes [158]. In chapter 5, we have compared the electronic structure and optical spectra calculated with the B3LYP functional and CAM-B3LYP functional. In addition, using geometries optimized in vacuum, the electronic structures of all systems studied were calculated in chloroform, benzonitrile, and acetonitrile to elucidate the effect of the solvent polarity.

For calculating projected density of states (PDOS), the QD/dye is divided into fragments. After the single-point energy calculation, the total density of state (DOS) is projected onto each fragment by performing population analysis. PDOS are plotted using an inhomogeneous Gaussian line-broadening:

$$A(\omega) = \frac{1}{\sigma\sqrt{\pi}} \sum_{n} h_n exp \frac{-(\omega_n - \omega)^2}{\sigma^2} \tag{3.1}$$

where ω_n is n-th ground state Kohn-Sham (KS) energy eigenvalue. σ=100 meV. h_n is the percentage of KS orbitals projected on the specified fragment of total system. For total DOS, $h_n = 1$. Eqn. (3.1) is also used for plotting the absorption spectra based on the TDDFT calculations, in which ω_n and h_n are excitation energy and oscillation strength, respectively, and σ is empirical

parameter for line broadening chosen to be 100 meV that is close to the experimental width of 130 meV of the first absorption peak in 1.7 nm CdSe nanocrystal [164]. The excitation energy and oscillation strength in eqn. (3.1) are obtained by solving the linear response equation based on Casida formalism [165]. To visualize the photoexcited states as separated hole-electron pairs, natural transition orbitals (NTOs) [166] are calculated. To visualize the charge-transfer state, the charge density difference (CDD) between the excited state and ground state is calculated. Gaussview software [167] is used for plotting the NTOs pairs corresponding to the lowest and first absorption peaks, as well as the CDD pairs corresponding to bright transitions. NTOs, CDD, PDOS and TDDFT calculations are performed by Gaussian09 software [168].

Solvation effect is included using the polarizable continuum medium model (CPCM) implemented in both Gamess and Gaussian09 software packages [169] with the dielectric constants (ε) defined for different solvent. Two different solvents, acetonitrile (CH_3CN,$\varepsilon = 35.688$), and dichloromethane (CH_3Cl, $\varepsilon = 9.08$) are used in order to compare the effect of polarity on the electronic structure of dye functionalized QDs. Single-point energy and TDDFT calculations are performed in both solvents. DMA calculation is carried out in CH_3Cl.

3.3.2. Embedded fragment and constrained DFT for calculations of QD-dye interaction as well as electronic coupling

To perform the embedded fragment potential calculations, the electrostatic potential of QD is substituted by performing the distributed multipolar analysis [170, 171] (DMA) of the fragment charge distributions [140]. The composite is dived by the fragment environmental region (QD) and *ab initio* molecular region (dye), respectively. For the *ab initio* molecular part a strict quantum mechanical calculation is performed, while for the fragment part the electric field is expanded into the monopole, dipole, quadrupole and octupole terms by performing the DMA. In addition, the

first hyperpolarizability term is also included due to the QD/dye interface region likely to be polarized. Subsequently, all these terms are implemented in dye's Hamiltonian. The first hyperpolarizability term is updated after each electronic step because of the variation of electron densities of QD during self-consistent field (SCF) calculation, while all the other terms are implemented as permanent distributions in the dye's Hamiltonian. The DMA are carried out using the general atomic and molecular electronic structure system (Gamess) [172, 173] software package. Afterwards, the monopole, dipole, quadrupole, octopole and first hyperpolorizability terms are imported, and the embedded fragment potential calculation [174] is carried out using Dalton2015 *ab intio* electronic structure software package [175].

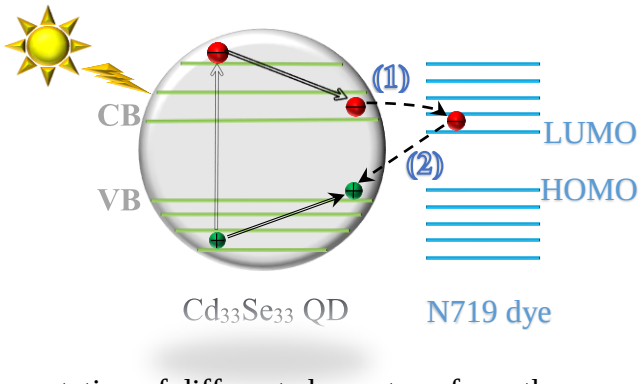

Figure 8. Schematic representation of different charge transfer pathway upon the photoexcitation of $Cd_{33}Se_{33}$ QD functionalized by N719 dye. For the displayed energetic alignment there are three possible pathways: (1) electron transfer (*et*) between lowest unoccupied energy levels of QD and dye; (2) electron in LUMO recombines with hole at VB edge (*re*).

To calculate the charge transfer integral, we consider two charge transfer diagrams (Figure 8): (1) electron transfer from CB edge to LUMO (*et*); (2) electron & hole recombination from LUMO to VB edge (*re*).

To reproduce a certain charge distribution condition for charge transfer, a scleronomic constraint, $\int w(r)\rho(r) = Nc$ is imposed with $\rho(r)$ being the electron density, Nc is the charge difference between donor and acceptor and $w(r)$ is the weight [176]. In case of *et* one extra negative

charge is placed in $Cd_{33}Se_{33}$ QD; in case of electron & hole recombination one extra negative charge and one extra positive charge are placed in $Cd_{33}Se_{33}$ QD and N719 dye, respectively. Afterwards, the geometry is optimized against the localized charges until the potential energy surface reaches the adiabatic crossing region, which gives two charge localized diabatic states. Afterwards, the two diabatic wavefunctions are imported into the charge transfer module [139] implemented in NWChem 6.5 software package [177] to obtain the charge transfer integral by solving the secular equation. The same functional and basis set that have been applied in previous DFT calculations are used for charge transfer integral calculations.

3.3.3. Calculations of the NA-couplings and NA-dynamics

To perform NA-dynamics, BD dye is attached to $Cd_{33}Se_{33}$ QD with carboxylate anchor. The initial geometry is contained in the simulation box with periodical boundary condition along x, y and z directions. To avoid the interactions between periodic images of QDs, the box is constructed to assure at least 10Å between QD replicas. The ground state geometry optimization is performed at 0 K, afterwards, the system is heated to 300 K until the temperature fluctuated within ±25K to reach thermal equilibrium. Then, a standard molecular dynamics is carried out to obtain the nuclear trajectory for calculating the NA coupling as well as the diagonal part of electronic Hamiltonian later on.

Tully surface hopping scheme paves the way to establish the correlation between nuclear trajectory with electronic dynamics, which is typically ignored in conventional time-dependent DFT. Providing such information is crucially important for describing the chare transfer property at the interface. However, to implement such scheme several adaptions have to be made, especially for modelling large-scale system. First, generalized gradient approximation functional (GGA) is used to calculate the electronic structure at each time step, which is much faster than hybrid

functional at the price of accuracy; second, a predetermined ground-state nuclear trajectory is used to propagate the electronic coefficient in order to save the computational cost. Nuclear trajectory is obtained through performing equilibrium molecular dynamics at 300 K after ground state geometry optimization; third, we have to provide the statistical distribution of electron population upon photoexcitation to serve as the starting point of propagating electronic coefficient by solving time-dependent Schordinger equation, meanwhile the correlation between nuclear trajectory and electronic dynamics is represented by the probability of trajectory surface hopping between electronic states by performing Tully surface hopping scheme. In the following, we will discuss the implementation as well as the accuracy for each case.

CHPATER 4. EFFECT of METAL ION ON ENERGETIC ALIGNMENT AND CHARGE TRANSFER EXCITATION

In this chapter we study the effect of tuning metal ion on interfacial energetic alignment between QD and dye. In general, a proper energetic alignment promises the hole transfer by overcoming the QD-ligand's interfacial potential barrier, and dissipating the relaxation energies into the passivating ligands [65]. In addition, an instant charge delocalization between the donor and the acceptor may also occur assuming electronic coupling sufficiently large [38] and the effective mass of hole in donor sufficiently small [59]. However, the study shows the energetic alignment between Tris(2,2´-bipyridine)Ru(II) dye and $Cd_{33}Se_{33}$ QD does not favor the hole transfer[81]; while the large effective mass of hole in small-sized CdSe QD (1~10 nm) reduces the electronic coupling effect [22]. Hence, we substitute different metal ion of dye, and examine the differences in the energetic alignment as well as the charge-transfer excitations in different Me(II) dye functionalized $Cd_{33}Se_{33}$ QDs.

4.1. Results and Discussion

4.1.1. Geometrical structures

To investigate the metal ion effect on interfacial energetic alignment, $Cd_{33}Se_{33}$ QD is functionalized by Tris(2,2'-bipyridine)Me(II) complex ($[Me(II)(bpy)_2(mcb)]^{1+}$), mcb is 4'-methyl-4-carboxy-2,2'-bipyridine, where Me= Os, Ru, Cr, Fe, Cd (Figure 9). All Me(II) complexes in this study had been synthesized previously in labs with physical and chemical properties well characterized [178-181].

The order of magnitudes of electronegativities between the metal ions is: Os = Ru > Fe > Cd > Cr, according to Pauli electronegativity. The electronegativities of Cd and Cr are very close and relatively smaller than the other three metal elements. Os and Ru possess the same

electronegativity; however, Os^{2+} holds more valence electrons ($4f^{14}5d^6$), thus a larger radii than Ru^{2+}. The electronegativity of Fe is larger than Cd and Cr, but smaller than Os and Ru. In the oxidized form Fe^{2+} has a slightly larger set of d electrons ($3d^6$) than Cr^{2+} ($3d^4$), but they possess different spin states when complexing with ligands. For instance, $Fe(II)(bpy)_3^{2+}$ complex is spin free [182] with fully paired d electrons, while $Cr(II)(bpy)_3^{2+}$ complex has been found to possess two unpaired electrons[182, 183]. Cd^{2+} has a full set of d orbitals ($4d^{10}$), therefore it possesses a fully degenerated ground state.

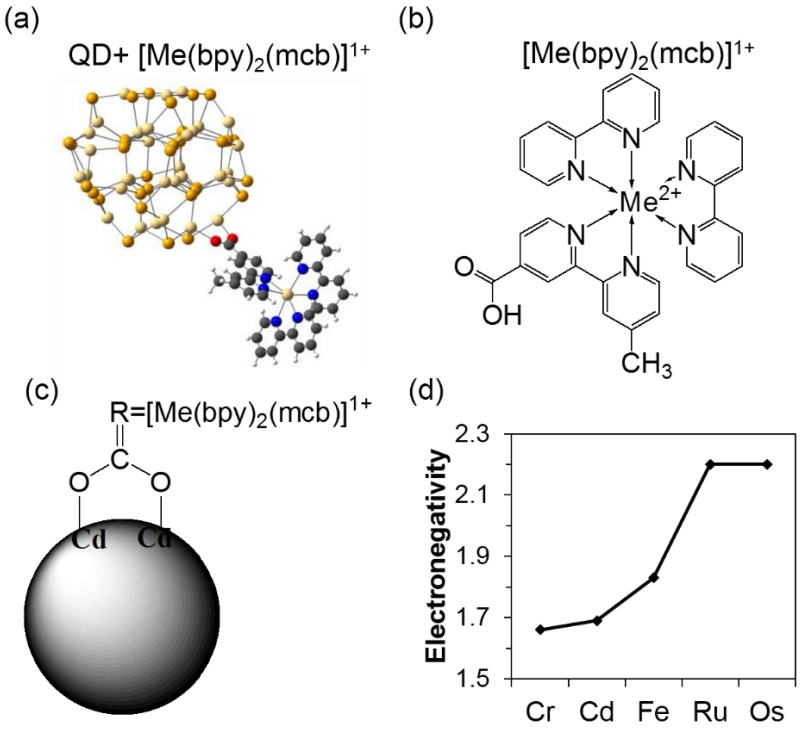

4

Figure 9. (a) $Cd_{33}Se_{33}$ QD functionalized by tris(2,2-bipyridine) Me(II) complex ($[Me(bpy)_2(mcb)]^{1+}$). (b) schematic structure of $[Me(bpy)_2(mcb)]^{1+}$ complex. (c) $[Me(bpy)_2(mcb)]^{1+}$ complex is attached on QD's surface through carboxylic acid linker. (d) The order of magnitudes of pauli electronegativities between different transition metal is: Os=Ru>Fe>Cd>Cr.

Table 1. Average NBO charges for the bare and the $[Me(II)(bpy)_2(mcb)]^{1+}$ dye functionalized $Cd_{33}Se_{33}$ QDs calculated in vacuum and solvent.

Vacuum							
	Cd	Se	N	H	O	C	Me(II)
Bare $Cd_{33}Se_{33}$ QD	0.95	-0.99					
Ru(II) dye/$Cd_{33}Se_{33}$ QD	0.97	-0.99	-0.44	0.25	-0.77	-0.76	0.28
Cd(II) dye/$Cd_{33}Se_{33}$ QD	0.97	-0.99	-0.62	0.25	-0.77	-0.76	1.51
Cr(II) dye/$Cd_{33}Se_{33}$ QD	0.97	-0.99	-0.48	0.25	-0.77	-0.76	0.49
Fe(II) dye/$Cd_{33}Se_{33}$ QD	0.97	-0.99	-0.45	0.25	-0.77	-0.76	0.30
Os(II) dye/$Cd_{33}Se_{33}$ QD	0.97	-0.99	-0.46	0.25	-0.77	-0.76	0.43
Dichloromethane							
	Cd	Se	N	H	O	C	Me(II)
Bare $Cd_{33}Se_{33}$ QD	1.07	-1.08					
Ru(II) dye/$Cd_{33}Se_{33}$ QD	1.09	-1.08	-0.44	0.25	-0.78	-0.76	0.29
Cd(II) dye/$Cd_{33}Se_{33}$ QD	1.10	-1.08	-0.60	0.25	-0.78	-0.76	1.55
Cr(II) dye/$Cd_{33}Se_{33}$ QD	1.09	-1.08	-0.47	0.25	-0.78	-0.76	0.49
Fe(II) dye/$Cd_{33}Se_{33}$ QD	1.08	-1.08	-0.45	0.25	-0.78	-0.76	0.30
Os(II) dye/$Cd_{33}Se_{33}$ QD	1.09	-1.08	-0.45	0.25	-0.78	-0.76	0.44
Acetonitrile							
	Cd	Se	N	H	O	C	Me(II)
Bare $Cd_{33}Se_{33}$ QD	1.09	-1.08					
Ru(II) dye/$Cd_{33}Se_{33}$ QD	1.09	-1.08	-0.43	0.25	-0.78	-0.76	0.29
Cd(II) dye/$Cd_{33}Se_{33}$ QD	1.09	-1.09	-0.60	0.25	-0.78	-0.76	1.56
Cr(II) dye/$Cd_{33}Se_{33}$ QD	1.10	-1.08	-0.47	0.25	-0.78	-0.76	0.49
Fe(II) dye/$Cd_{33}Se_{33}$ QD	2.19	-1.08	-0.45	0.25	-0.78	-0.76	0.29
Os(II) dye/$Cd_{33}Se_{33}$ QD	2.17	-1.08	-0.45	0.25	-0.78	-0.76	0.44

Each Cd in bare QDs contains nearly the same positive charge, ca. (0.87-1.02)e in vacuum (table 1), which is consistent with the published data [184]. Adding solvent increases the positive charge on Cd, ca. (0.94−1.19)e in CH_3Cl and ca. (0.96−1.21)e in CH_3CN, respectively. Cd or Se remains nearly the same charges by comparing the functionalized QDs with bare QDs, suggesting a weak perturbation of Me(II) complex to QD's surface states. The surface states of QDs are mainly distributed in the frontier molecular orbitals populated by the electrons in Se atoms [185],

therefore the weak perturbation indicates a weak orbital interaction between QD and dye, as such, Dexter type energy transfer through electron exchange interaction is unlikely to play a vital role in $Cd_{33}Se_{33}$ QD/$[Me(II)(bpy)_2(mcb)]^{1+}$ composite, which requires a strong frontier orbital interaction between QD and dye. Our conjecture is in line with the recent experimental study of CdSe QD/$[Co(III)(bpy)_3]^0$ complex nanocrystal composite [186], in which it is observed the weak Dexter type energy transfer by measuring the energetic alignment between QD and dye.

Bonding between Cd and Se reflects the delocalization of electrons in CdSe QD. NBO analysis suggests, Cd-Se bond is sp hybridized σ bond with ~90% p character from Se and ~10% s character from Cd. The Cd-Se bond remains nearly the same in both dye functionalized QD and bare QD (see table 2). However, there are more Cd-Se bonds in the functionalized QD than bare QD, which suggests the attachment of dye increased the delocalization of electrons. Our results resembles Matthew et al.'s study [65] in which the delocalization radius of the exciton confinement is controlled by the height of potential barrier through the interfacial orbital interaction between CdSe QD and hole-delocalizing ligand phenyldithiocarbamate. However, unlike small organic ligands, the HOMO of $[Me(II)(bpy)_2(mcb)]^{1+}$ complex is deep inside the VB of QD, as such, the enhanced delocalization of electrons is caused by the long-range QD-dye interaction. It further suggests, attaching the metal complex on different facet plane of QD as well as manipulating the binding geometries of metal complex to CdSe QD have an influence on the surface states, which would have the potential effects on the electronic dynamics upon photoexcitation, such as charge transfer, Auger recombination, biexciton generation, etc.

Table 2. Averaged Cd-Se, Cd-O, C-C, C-N, C-H and N-Me(II) bond lengths (Å) of $Cd_{33}Se_{33}$ QD/Me(II) complex composite in vaccum, CH_3CN and CH_3Cl.

		Bare QDs	QD/Cr(II) complex	QD/Os(II) complex	QD/Ru(II) complex	QD/Fe(II) complex	QD/Cd(II) complex
Vacuum	Cd-Se (core)	2.85	2.85	2.85	2.85	2.85	2.85
	Cd-Se (surf)	2.78	2.77	2.77	2.77	2.77	2.77
	Cd-O		2.38	2.30	2.30	2.30	2.30
	C-C		1.42	1.42	1.42	1.42	1.41
	C-N		1.37	1.38	1.37	1.37	1.36
	C-H		1.09	1.08	1.08	1.08	1.10
	C-O		1.28	1.29	1.29	1.29	1.30
	N-Me(II)		2.07	2.09	2.10	2.01	2.38
CH_3CN	Cd-Se (core)	2.92	2.88	2.92	2.91	2.92	2.91
	Cd-Se (surf)	2.87	2.85	2.86	2.87	2.86	2.86
	Cd-O		2.38	2.36	2.36	2.30	2.36
	C-C		1.42	1.41	1.41	1.41	1.41
	C-N		1.37	1.34	1.37	1.37	1.36
	C-H		1.08	1.09	1.08	1.08	1.09
	C-O		1.29	1.29	1.29	1.29	1.29
	N-Me(II)		2.07	2.08	2.09	2.00	2.43

Table 2. Averaged Cd-Se, Cd-O, C-C, C-N, C-H and N-Me(II) bond lengths (Å) of $Cd_{33}Se_{33}$ QD/Me(II) complex composite in vaccum, CH_3CN and CH_3Cl (continued).

	Cd-Se (core)	2.92	2.87	2.93	2.92	2.92	2.92
	Cd-Se (surf)	2.86	2.83	2.85	2.85	2.85	2.85
CH_3Cl	Cd-O		2.36	2.36	2.35	2.35	2.34
	C-C		1.42	1.41	1.41	1.41	1.41
	C-N		1.37	1.37	1.37	1.37	1.36
	C-H		1.09	1.11	1.09	1.09	1.09
	C-O		1.29	1.29	1.29	1.29	1.29
	N-Me(II)		2.07	2.08	2.09	2.09	2.41

4.1.2. Dependency of the spin-State energetics of dye on the exact exchange in functional

To determine the ground spin state of a metal complex, the total energies of different spin multiplicity are calculated. We choose the restricted Hartree-Fock (RHF) Slater determinant to expand one-electron density as a linear combination of localized atomic basis sets. Geometry optimization with RHF typically searches a lower stationary point close to global minimum than unrestricted Hartree-Fock (UHF) Slater determinant due to the well-known spin contamination [187].

It is known the exact exchange (a_0) always stabilizes high-spin states due to fermi correlation [188]. Increasing a_0, in certain situations, creates artificial high spin ground state. For example, Paulsen et al [189] found high spin multiplicity is falsely predicted to be the ground state for a number of Fe(II) complexes ($[Fe(tpa)(NCS)_2]$, $[Fe(bptn)(NCS)_2]$ (bptn=N,N‘-bis(2-pyridylmethyl)-1,3-propanedi-amine), $[Fe(phen)_2(NCSe)_2]$, $[Fe(tpm)_2]^{2+}$(tpm=tris-(1-pyrazolyl)methane), etc) when using B3LYP functional with 20% exact exchange. On the other

hand, reducing the percentage of exact exchange, in certain situation, correctly predicts the ground spin state of a transition-metal complex. For example, Hauke et al [189] calculate the free energies of $[Fe(N_H)S_4]L$ (L=CO, NO^+, PR_3, NH_3, N_2H_4) by reducing a_0 to 15%, and correctly predict the singlet ground states, while the standard B3LYP functional falsely predicts the quartet ground states. Latevi et al [188] further found the metal-ligand bond length is proportional to the amount of exact exchange parameter in the functional, in which the metal-ligand bond is elongated by increasing a_0, which reduces the wavefunction overlapping between metal ion and related ligands, consequently, the electrons in t_{2g} level tend to populate into e_g level due to the reduced ligand field that creates artificial high spin ground state.

Based on above studies, it is reasonable to assume the ground spin state of $[Me(II)(bpy)_3]^{2+}$ complex can be correctly predicted when reducing the exact exchange parameter to some threshold value. Therefore, we benchmark $[Fe(II)(bpy)_3]^{2+}$ complex with three different percentage of a_0: 30%, 25% and 20% (inset in Figure 10 (b)).

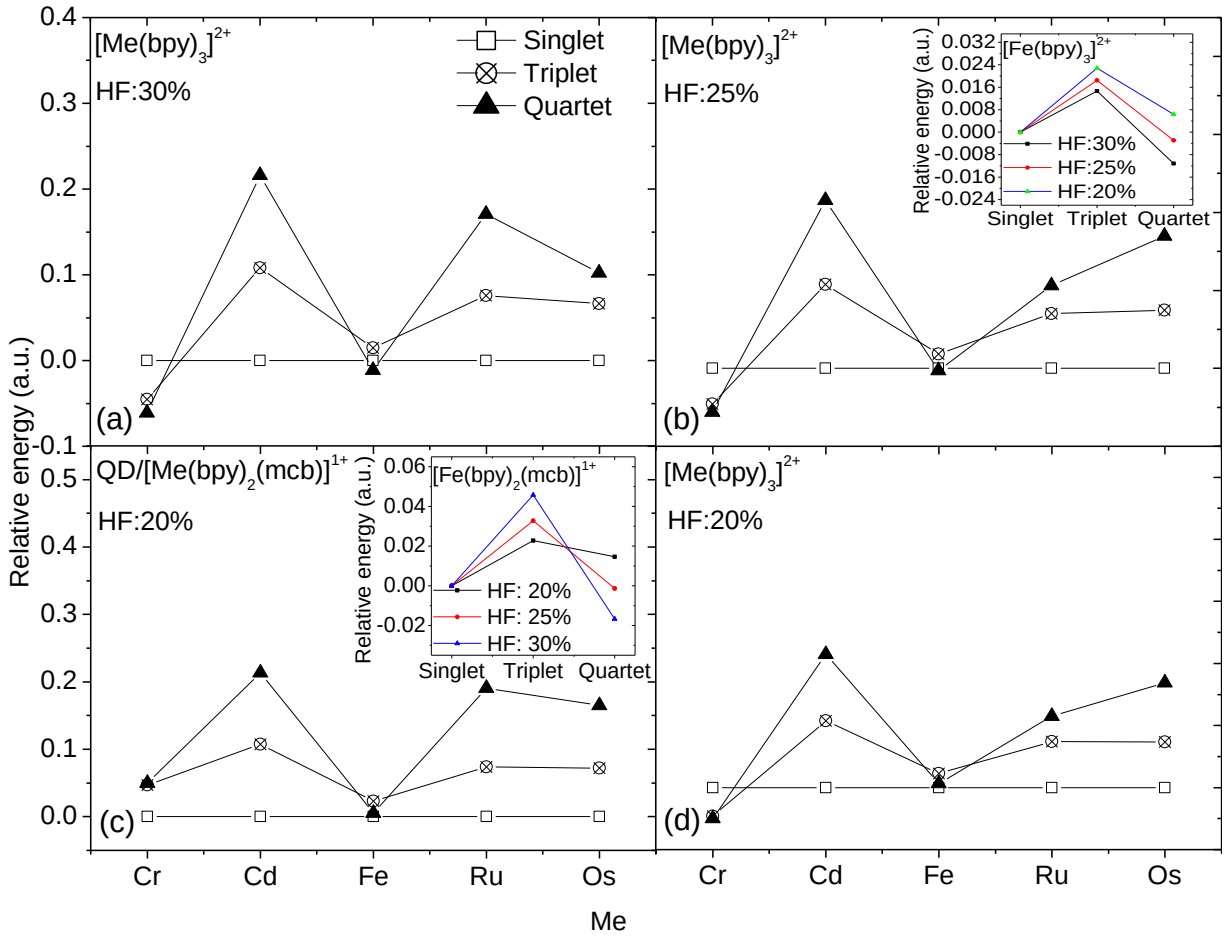

Figure 10. The energy differences (relative energies) between the singlet, triplet and quartet states for $[Me(II)(bpy)_3]^{2+}$ complex and $[Me(II)(bpy)_2(mcb)]^{1+}$ complex. The zero point is chosen to be the spin state of lowest energy. All complexes have the singlet states in lowest energies except $[Cr(II)(bpy)_3]^{2+}$ and $[Fe(II)(bpy)_3]^{2+}$ complexes. As the percentage of exact exchange in B3LYP functional decreased from 30%, 25% to 20%, it does not significantly affect the relative energetic positions between the spin states for most metal complexes. However, the singlet state of $[Fe(II)(bpy)_3]^{2+}$ complex is initially higher in energy than triplet state, which switches to triplet ground state when the exact exchange is reduced to 20%.

To our surprise, when a_0 is reduced to 20%, i.e. B3LYP, the singlet state is predicted to be the lowest energetic state, which is 5% higher than the exchange parameter suggested in Hauke et al's study. This is due to the fact that the chemical structure $[Fe(II)(bpy)_3]^{2+}$ complex is different from Fe(II)/Fe(III) complexes in their study, subjecting to different ligand field, and giving different correlation between the exact exchange and metal-ligand bond. We further benchmarked

the spin-state energies for other $[Me(II)(bpy)_3]^{2+}$ complexes using three different exact exchange parameters (Figure 10 (a), (b) and (d)). The zero point is chosen to be the spin state with lowest energy. Our results show, the singlet state is predicted to be ground state for most $[Me(II)(bpy)_3]^{2+}$ complex except for $[Cr(II)(bpy)_3]^{2+}$ and $[Fe(II)(bpy)_3]^{2+}$ complexes. $[Cr(II)(bpy)_3]^{2+}$ has the triplet ground state; however, it changes to the singlet when substituting one of the 2,2'-bipyridine ligands with mcb ligand. By inspecting the number of electrons in mcb ligand, we noted the methyl group and carboxylate group contain odd number of electrons, respectively. Therefore, we speculate that, the unpaired electrons in Cr^{2+} are saturated by the unpaired electrons from methyl and carboxy groups. To verify the speculation, we divide $[Cr(II)(bpy)_2(mcb)]^{1+}$ complex into the metal part and ligand part, then perform the single-point energy calculations for each fragment. We found, the spin density of Cr^{2+} is 2.98 when coordinating with three 2,2'-bipyridine ligands; however, it changes to 1.12 when one of the 2,2'-bipyridine ligands is substituted with mcb ligand, indicating a singlet state (Figure 10 (c)), and suggesting mcb ligand having an effect of stabilizing low spin state of $[Me(II)(bpy)_2(mcb)]^{1+}$ complex.

Another interesting fact is, $[Fe(II)(bpy)_3]^{2+}$ complex possesses a lower quartet state than triplet state, which is close to the singlet state ($\Delta E_{difference} = 0.012\ eV \ll 1K_bT$), therefore the ground state tends to be trapped in the quartet state during the light-induced photo-relaxation [190, 191]. However, a substitution of 2,2´-bipyrindine ligand with mcb ligand stabilizes the low spin state, and increases the separation between the singlet and quartet states, thus reduces the probability of high spin mesostable state.

We further calculate the spin-state energies for $[Me(II)(bpy)_2(mcb)]^{1+}$ complexes (Figure 10 (c)). The singlet state is predicted to be the ground state for all complexes. In addition, the energy separation between low spin and high spin states is increased along with the decrease of

exact exchange parameter (as illustrated by $[Fe(II)(bpy)_2(mcb)]^{1+}$ complex in the inset of Figure 10 (c)), which means, the high spin states cannot cross over the low spin state by reducing the exact exchange parameter, once the singlet state becomes the lowest energetic state. Therefore B3LYP functional is reliable for predicting the ground spin states for all $[Me(II)(bpy)_2(mcb)]^{1+}$ complexes, which inspires our confidence on using B3LYP functional. Overall, the spin of $[Me(II)(bpy)_2(mcb)]^{1+}$ complex for our study is singlet based on above calculations. In addition, attaching the metal complex to the surface of $Cd_{33}Se_{33}$ QD further stabilizes the singlet state against the HF portion.

4.1.3. Energetic alignment between QD and dye

One important question to be resolved in our study is, whether changing the electronegativity of metal ion favor the energetic condition of hole transfer from QD to dye. To address it, we get the energy difference (E_{oc}) between highest occupied states of QD and dye from PDOS (illustrated for Os(II) complex in Figure 11). In addition, we get the energy difference (E_{un}) between the lowest unoccupied states of QD and dye, and the total band gap (E_g) from PDOS.

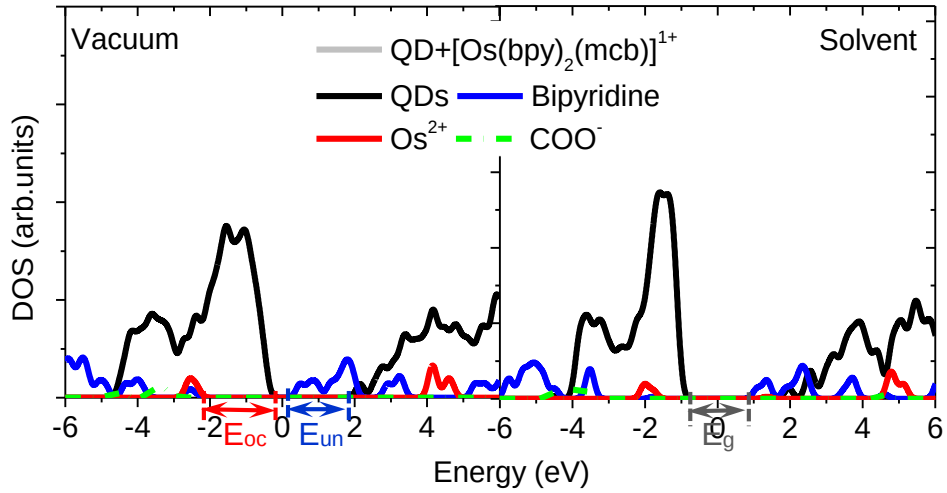

Figure 11. Projected density of states (PDOS) of $Cd_{33}Se_{33}$ QD/Os(II) dye complex composite in vacuum and in solvent, respectively. The energy difference between the HOMOs of Me(II) complex and QD is denoted as E_{oc}, while the energy difference between the lowest unoccupied states of Me(II) complex and QD is denoted as E_{un}. The total band gap is denoted as E_g.

Figure 12 is the complete PDOS information for all QD/dye composites. Our results show, the highest occupied orbital of dye is hybridized between metal ion and 2,2´-bipyridine, therefore the relative position of HOMO with respect to the VB edge is associated with metal-ligand interaction. The lowest unoccupied energy level is dominated by 2,2´-bipyridine with no hybridization character. The larger metal-ligand interaction, the larger energy gap between bonding- and antibonding orbitals. As a result, HOMO is driven into deeper energy levels. Increasing electronegativity pulls electrons closer to nuclear, consequently, it reduces the electronic interaction between metal ion and ligand field, and shifts HOMO upwards. Even though LUMO is not directly associated with metal-ligand interaction, the decrease of metal-ligand interaction causes the low-lying unoccupied molecular orbitals shifted downward, therefore the LUMO energy level is decreased too.

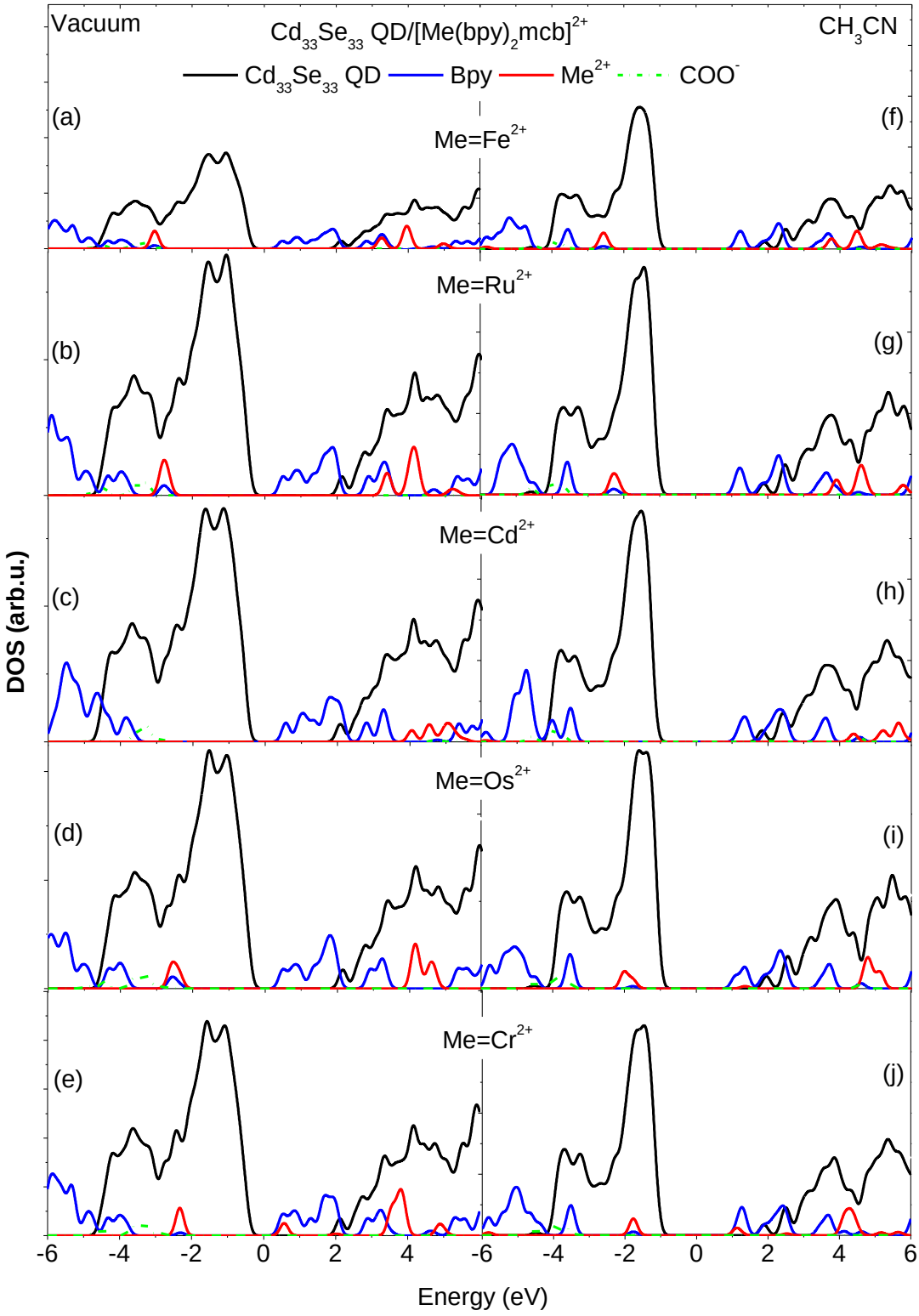

Figure 12. Projected density of states (PDOS) of $Cd_{33}Se_{33}$ QD functionalized by Fe(II), Ru(II) and Cd(II) dye, respectively. The calculations are performd in vacuum (left column) and CH_3CN (right column), respectively.

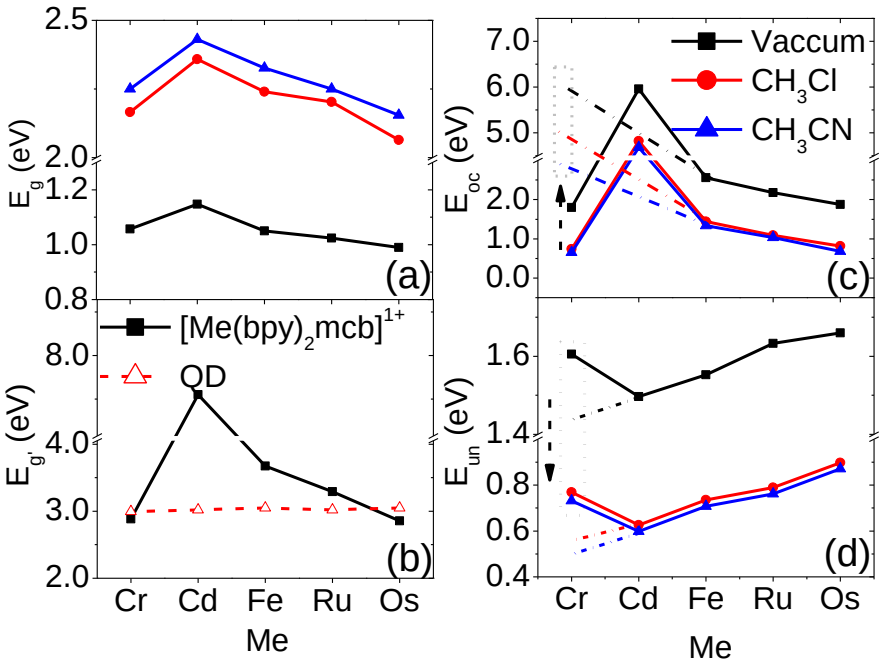

Figure 13. (a) Band gaps (E_g) of dye functionalized $Cd_{33}Se_{33}$ QDs in vacuum, CH_3CN and CH_3Cl, respectively, which increase with the polarity of solvent. There exists a significant difference between the band gaps of QDs functionalized by different Me(II) complex, in solvent, i.e. Cd(II) > Fe(II) > Ru(II) > Os(II) > Cr(II). However, the difference beomes smaller in vacuum. (b) Band gaps ($E_{g'}$) of bare QD and isolated Me(II) dye that are directly cut from QD/dye composite. The calculations are performed in CH_3CN. (c) and (d) are the energy differences (E_{oc}) between the highest occupied states, and the energy differences (E_{un}) between the lowest unoccupied states in QD/dye composite. The E_{oc} and E_{un} for Cr(II) deviate from the trace line of other metals (dashed line).

Figure 13 (c) and (d) show, except $[Cr(II)(bpy)_2(mcb)]^{1+}$ complex, the energy difference E_{oc} is increased with the electronegativity, while this is the opposite trend for the energy difference E_{un}. Adding solvent reduces both E_{oc} and E_{un}, in addition, it increases the number of states in frontier molecular orbitals in occupied energy levels for both QD and dye. Cd(II) complex has the largest E_{oc}, then it is Fe(II), Ru(II), Os(II) and Cr(II) complexes in a descending order. The trend is opposite for E_{un}. Even though Ru and Os have the same electronegativity, Ru(II) complex has larger E_{oc} and smaller E_{un} than Os(II) complex, suggesting some additional factor controlling the energy difference. As indicated earlier, Os(II) holds more valence electrons thereof a larger radii

than Ru(II), which gives a stronger metal-ligand interaction. A stronger metal-ligand interaction opens the HOMO-LUMO gap of dye with respect to the CB and VB edges of QD, respectively. Accordingly, it decreases E_{oc}, and increases E_{un}. We also noted, Cr has the smallest electronegativity; however it turns out the E_{oc} of Cr(II) complex is the smallest one, while E_{un} is the largest one among all complexes. Such unusual trend is due to the dipole-dipole interaction changes the percentage of highest occupied d_{z^2} electron density in Me(II) ion, which will be explicitly discussed in the next section. There is a general trend that the total band gap is decreased with the electronegativity except Cd(II)- and Cr(II) dye functionalized $Cd_{33}Se_{33}$ QDs, and adding solvent increases the total band gap (Figure 13 (a)).

Overall, based on above analysis we conclude that, increasing electronegativity has a main effect of increasing energy separation between LUMO of dye and CB edge, and decreasing the energy separation between HOMO of dye and VB edge.

4.1.4. QD-dye interaction and photoinduced charge transfer

The QD-dye interaction had been indicated for playing an important role in the energetic alignment, according to previous report [29]. Here, we are particularly interested in elucidating the role of varying QD-dye interaction with respect to the electronegativity of metal ion. To illustrate such effect, we first apply the distributed multipolar analysis (DMA) to expand QD's total charges, then the expanded total charges are embedded into dye's electric field. QD-dye interaction can be represented as multipole interaction terms in dye's Hamiltonian, such as monopole, quadrupole, octupole, etc; however monopole term is originated from the zero-order expanded electron density that is strongly confined within $Cd_{33}Se_{33}$ QD, thus it has a negligible contribution in QD-dye interaction. The quadrupole, octupole and first hyperpolarizability energies are orders of magnitudes smaller than the dipole energies (Figure 14 (a) and (b)). Therefore, the main

contributor to QD-dye interaction originates from the dipole energy. The order of magnitudes of dipole energies between QD and different Me(II) complex is: QD-Cr(II) complex > QD-Os(II) complex > QD-Ru(II) complex > QD-Fe(II) complex> QD-Cd(II) complex (Figure 14 (b)).

As indicated earlier, the value of E_{oc} for $Cd_{33}Se_{33}$ QD/Cr(II) dye does not appear in the anticipated position (dashed line in Figure 14 (c) and (d)) according to the electronegativity. By inspecting the highest occupied d_{z^2} orbitals (Table 3), we found, all other complexes except Cr(II) complex remain nearly the same d_{z^2}-orbital after attaching to QD's surface, indicating a negligible effect of QD-dye dipole interaction on ligand field. Therefore, the energetic alignment between QD and dye is not significantly perturbed by such interaction, which follow the trend of electronegativity of metal ion. However, in case of Cr(II) complex the size of d_{z^2}-orbital is decreased significantly after attaching dye to QD's surface indicating a significant change of ligand field, which reduces the metal-ligand interaction resulting in a small E_{oc} and a large E_{un}. Such unusual trends of E_{oc} and E_{un} in case of Cr(II) complex suggests the QD-dye dipole interaction perturbs the energy level alignment by changing the ligand field, which reduces the metal-ligand interaction. On the other hand, even though Os(II) complex has the second largest dipole interaction with $Cd_{33}Se_{33}$ QD, the size of d-orbital is not as decreased as Cr(II) complex. This is because Os(II) ion contains additional f electrons than Cr(II) ion, which gives a stronger shielding effect towards the electronic interaction, consequently, the d-orbital is not significantly perturbed by the dipole interaction. At last, we realize our model does not include the ligand passivation that induces the surface trap states near the band gap. However, our previous study for $Cd_{33}Se_{33}$ QD passivated by 21 OPMe3 ligands show [57], those ligand states are deep inside the VB, thus negligibly overlapped with QD's surface states. Additionally, the dipole moments of these ligands counterbalance each other in a fully passivated QDs due to the spherical symmetry shape of QDs,

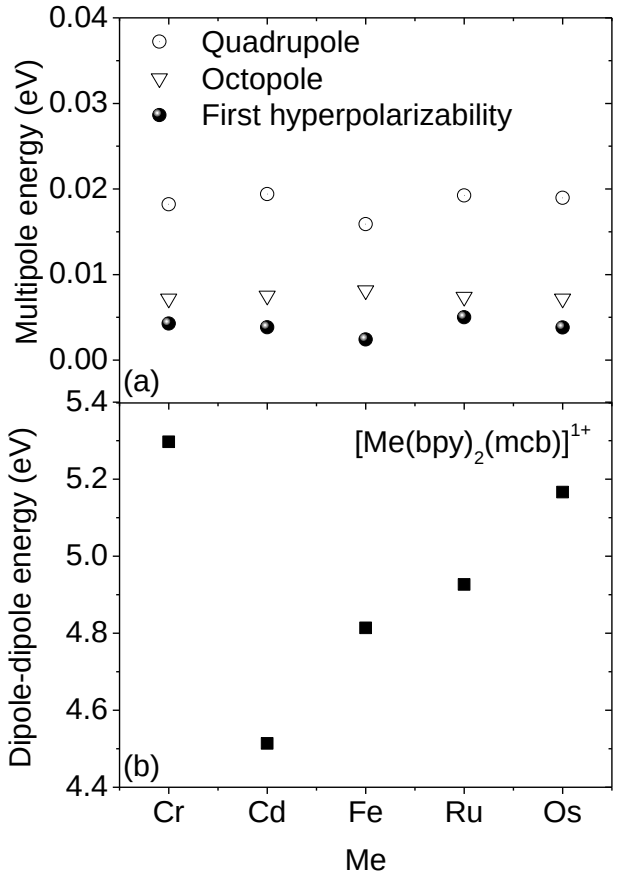

Figure 14. (a) Multipole interaction energies (absolute values) of $Cd_{33}Se_{33}$ QD/Me(II) dye composites by performing the distributed multipolar analysis (DMA). (b) The dipole-dipole energy between $Cd_{33}Se_{33}$ QD and Cr(II) complex or Os(II) complex is larger than the other dyes.

which do not bring additional dipole into QDs. As such, ligand passivation has an insignificant effect toward QD-dye interaction.

Table 3. The highest occupied d_{z^2} orbitals in isolated Me(II) complex and $Cd_{33}Se_{33}$ QD/Me(II) complex composite. The calculations are performed in CH_3Cl.

Me	Isolated Me(II) complex	CdSe QD/Me(II) complex composite
Ru	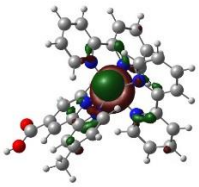	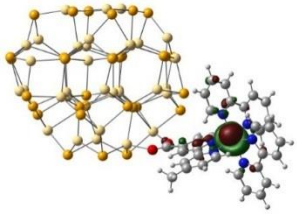
Cr	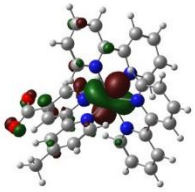	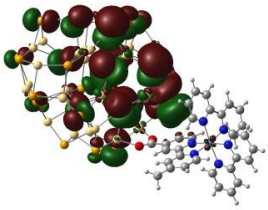
Fe	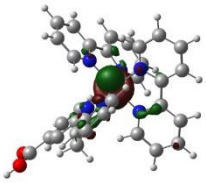	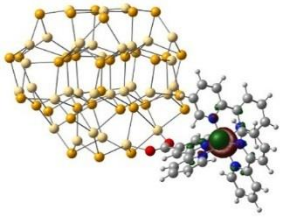
Os	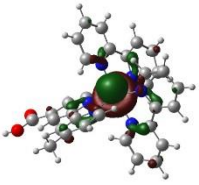	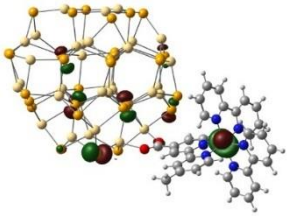
Cd	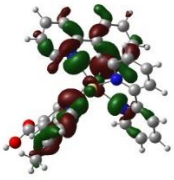	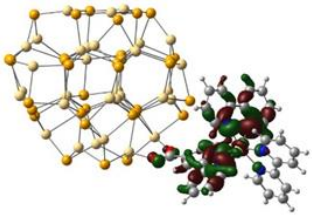

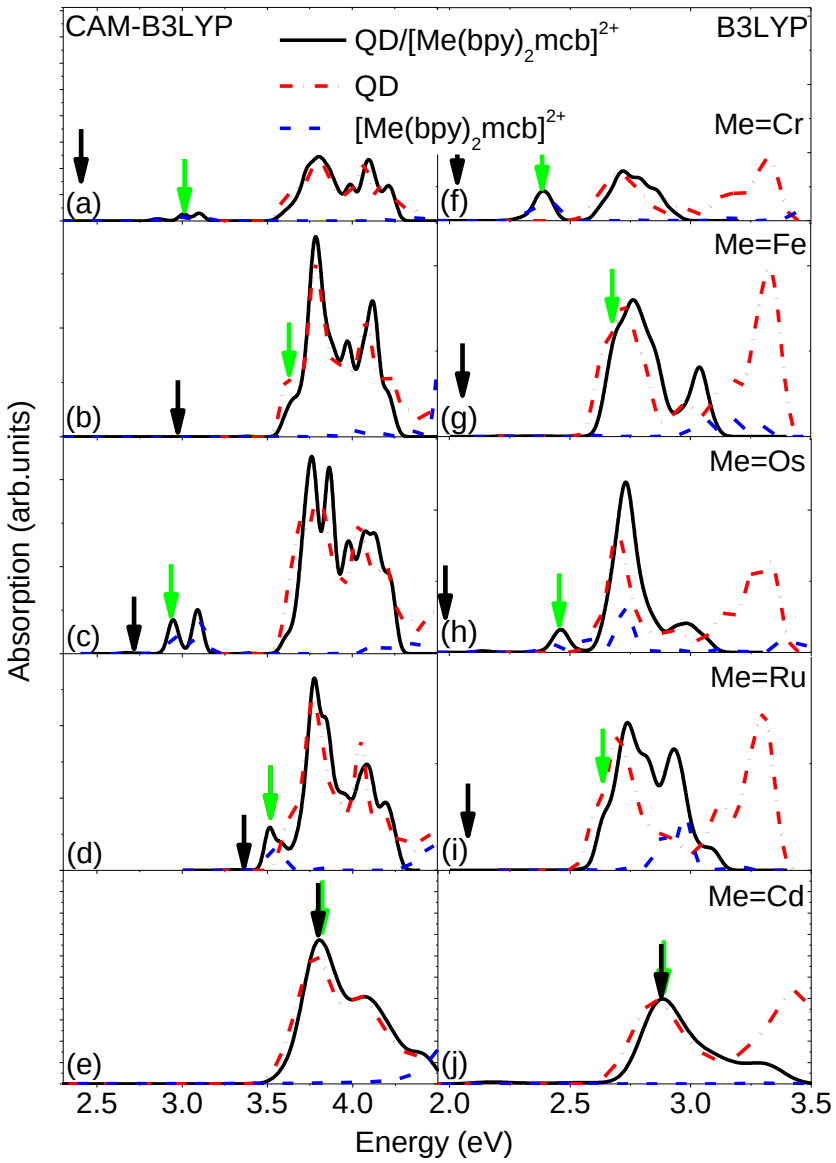

Figure 15. Absorption spectra of $Cd_{33}Se_{33}$ QD/Me(II) dye composite (black line), bare $Cd_{33}Se_{33}$ QDs (dashed dot red line) and isolated Me(II) complexes (dashed blue line). The green arrow marks the first absorption peak, while the black arrow marks the lowest optical transition. The geometries of bare $Cd_{33}Se_{33}$ QDs and isolated Me(II) complexes are cut from the dye functionalized $Cd_{33}Se_{33}$ QDs, then TDDFT calculations are carried out for the dye functionalized $Cd_{33}Se_{33}$ QDs, bare $Cd_{33}Se_{33}$ QDs and isolated Me(II) complexes in CH_3CN, respectively. The left and right columns show the absorption spectra calculated by CAM-B3LYP functional and B3LYP functional, respectively. CAM-B3LYP functional blue shifts the absorption spectra. Both B3LYP and CAM-B3LYP calculations show three types of optically active transitions: QD-to-QD, QD-to-dye, dye-to-dye; however dye-to-QD transition is optically dark in both spectra. Both spectra show a good additive feature, i.e. the curvature of bare $Cd_{33}Se_{33}$ QD adds the curvature of isolated dye approximately matches the curvature of QD/dye composite. For $Cd_{33}Se_{33}$ QD/Cd(II) dye composite the first absorption peak overlaps with the lowest optical transition.

Figure 15 shows the optical absorption spectra simulated based on Casida formalism using the B3LYP functional in CH_3CN. We also simulate the spectra with the long-range corrected CAM-B3LYP functional for comparison. Both B3LYP and CAM-B3LYP functional show a qualitative consistency in the transition orbitals of absorption spectra, except CAM-B3LYP functional blue shifts the absorption energy, which is a well-known issue for range-separated functional [192]. There exists three types of optically active transitions in both spectra: QD-to-dye, QD-to-QD and dye-to-dye. The dye-to-QD transition is optically dark. The first absorption peak for Cr(II)- or Os(II) dye functionalized $Cd_{33}Se_{33}$ QDs consists of metal-ligand and π,π^* transitions (Table 4) forming the Soret band centered around 400 nm. This is due to the fact that, Cr(II) complex and Os(II) complex have smaller band gaps ($E_{g'}$) than $Cd_{33}Se_{33}$ QD (Figure 13 (b)), therefore the lowest excitation originates from the dye. In contrast, for other dye functionalized $Cd_{33}Se_{33}$ QDs the first absorption peaks emanate from $Cd_{33}Se_{33}$ QD due to the band gaps of those dyes significantly larger than that of $Cd_{33}Se_{33}$ QD. In addition, we found, both CAM-B3LYP and B3LYP predict the same transition characters except for $Cd_{33}Se_{33}$ QD/Ru(II) complex composite. For $Cd_{33}Se_{33}$ QD/Ru(II) complex composite B3LYP predicts metal-metal transition, while CAM-B3LYP predicts MLCT transition. To understand the origin, we calculate the optical transition energies for bare $Cd_{33}Se_{33}$ QD and isolated dye using both functionals. Both QD and dye are directly cut from QD/dye composite, afterwards TDDFT calculations are carried out. Figure 15 shows, both B3LYP and CAM-B3LYP predict relatively constant trends for first optical transition energies of $Cd_{33}Se_{33}$ QDs via changing metal ions; however B3LYP predicts the first optical transition energy of $Cd_{33}Se_{33}$ QD lower than that of Ru(II) complex, on the contrary, CAM-B3LYP gives the opposite trends. It is known the optical transition at low energy range is composed of MLCT and π,π^* characters, therefore, we suspect MLCT is subjecting more impacts from

changing metal ion, while π,π* transition energy remains relatively unchanged. To prove our thought, we compared the transition energies corresponding to first- and highest absorption peaks of isolated dye calculated by CAM-B3LYP and B3LYP, respectively (Figure 16). Both functionals show, the first absorption peak is dominated by MLCT character, while the highest absorption peak is dominated by π,π* character. Indeed, the π,π* transition remains relatively constant via changing metal ion, while MLCT energy strongly depends on the metal ion. In addition, the trend of MLCT energies is similar to that of first optical transition energies of QD/dye composites, indicating the latter one dominated by MLCT character rather than π,π* character.

Table 4. Natural transition oribitals of lowest optical transition and first absorption in $Cd_{33}Se_{33}$ QD/Me(II) dye composite, as marked by dark arrows and green arrows in Figure 15. The calculations are performd in CH_3CN.

		Excited state energy and oscillation strength	Hole	Electron		Hole	Electron
QD/$[Os(bpy)_2(mcb)]^{2+}$	B3LYP	**S_1** **1.96 eV** **f=0.0027**	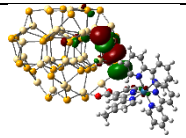	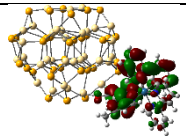	CAMB3LYP	**S_1** **2.71 eV** **f=0.004**	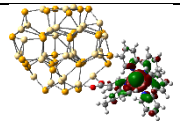	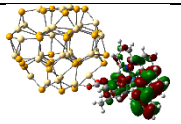
		S_{36} **2.47 eV** **f=0.06**	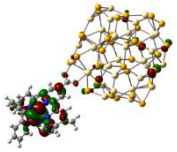	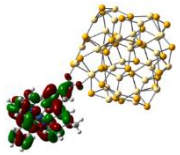		**S_8** **2.78 eV** **f=0.18**	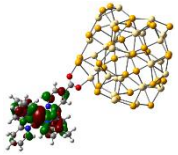	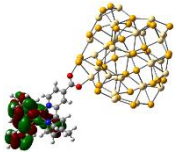
QD/$[Cr(bpy)_2(mcb)]^{2+}$	B3LYP	**S_1** **2.05 eV** **f=0.0039**	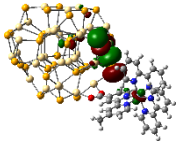	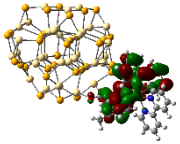	CAMB3LYP	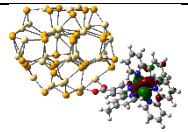 47% **S1** **2.32 eV** **f=0.0001** 33% **S_5** **3.02 eV** **f=0.04**	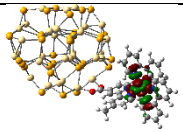 47% 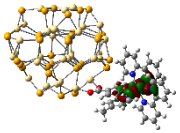 33%	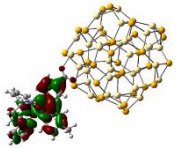
		S_{40} **2.37 eV** **f=0.14**	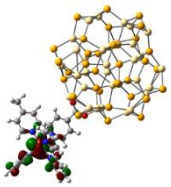	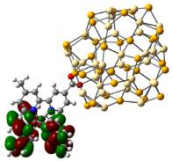			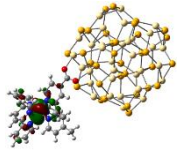	

Table 4. Natural transition oribitals of lowest optical transition and first absorption in $Cd_{33}Se_{33}$ QD/Me(II) dye composite, as marked by dark arrows and green arrows in Figure 15 (continued). The calculations are performd in CH_3CN.

QD/[Ru(bpy)$_2$(mcb)]$^{2+}$	B3LYP	**S_1** **2.07 eV** **f=0.0031**	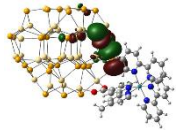	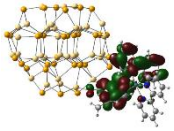	CAMB3LYP	**S_1** **3.31 eV** **f=0.0021**	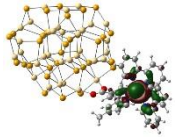	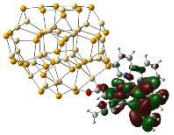
		S_{78} **2.69 eV** **f=0.14**	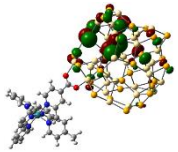	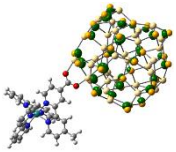		**S_9** **3.51 eV** **f=0.07**	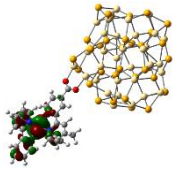	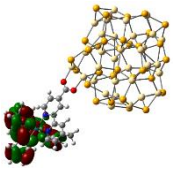
QD/[Fe(bpy)$_2$(mcb)]$^{2+}$	B3LYP	**S_1** **2.04 eV** **f=0.01**	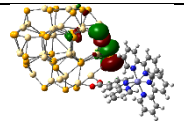	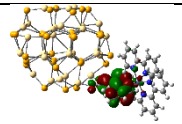	CAMB3LY P	**S_1** **2.94 eV** **f=0.0004**	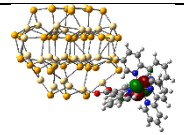	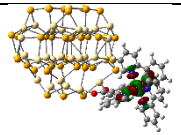
		S_{65} **2.65 eV** **f=0.07**	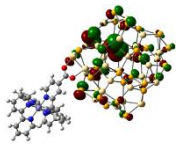	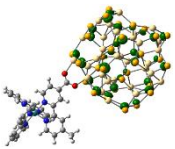		**S_9** **3.62 eV** **f=0.09**	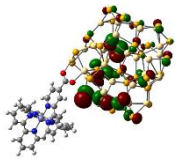	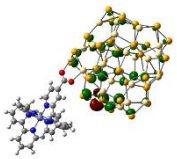
QD/[Cd(bpy)$_2$(mcb)]$^{2+}$	B3LYP	**S_1** **2.81 eV** **f=0.015**	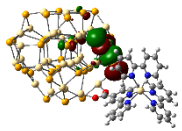	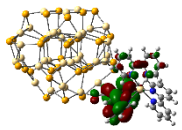	CAMB3LYP	**S_1** **3.73 eV** **f=0.03**	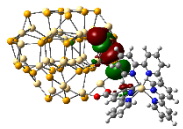	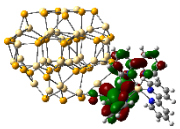

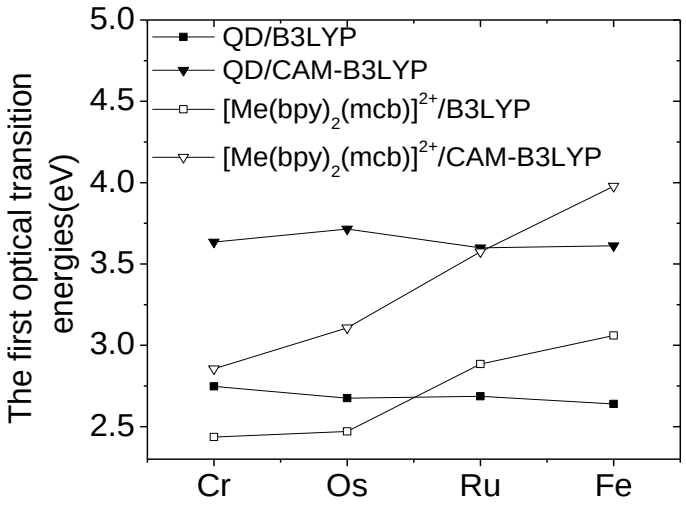

Figure 16. The first optical transition energies of bare QDs, marked by filled symbols, and isolated Me(II) complexes, marked by void symbols. The geometries of bare QDs and isolated Me(II) complexes were kept as the same as in the optimized functionalized QDs. B3LYP functional and CAM-B3LYP functional are used to calculate the first optical transition energies, which are denoted by squre and triangle symbols, respectively. CAM-B3LYP functional blue shifts the energies of lowest optical transition. The first optical transition energies of isolcated Cd(II) complex are in the ultraviolet range, which are not shown.

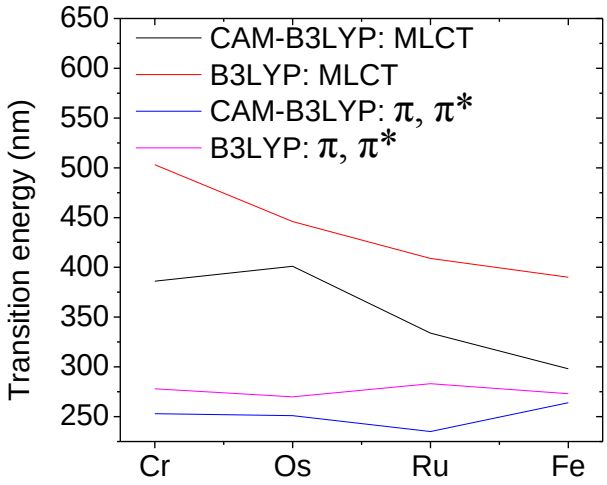

Figure 17. The optical transition energy of MLCT and π,π*.

The lowest optical transition (S1) provides important charge-transfer information in QD/dye composite. If S1 is localized in CdSe QD, which is typically dark at room temperature, those dark excitons become bright state in photoluminescence emission. The emission energy as well as emission time are associated with surface trap states of QD [193]. Otherwise, the emission originates from the lowest singlet/triplet mixed state of dye resulting in different charge relaxation pathway due to the spin-orbit coupling effect. For instance, a weak spin-orbit coupling allows for a longer electron lifetime in the LUMO level of dye, increasing the charge injections to the CB of QD in prior to return to the ground state or reduced by the electrolyte. Moreover, studies [194, 195] show the lowest emitting state in CdSe QD is triplet, which allows for the spin-spin resonant interaction between lowest states of QD and dye giving additional tunability to control the charge carrier mobility in QD/dye nanocrystal composite. There is a divergence between the lowest optical transitions for most $Cd_{33}Se_{33}$ QD/Me(II) dye composites predicted by B3LYP functional and CAM-B3LYP functional (Table 4), in which B3LYP functional predicts a charge-transfer exciton, i.e. QD-to-dye, while CAM-B3LYP functional predicts a Frenkel exciton, i.e. dye-to-dye. This is because, as mentioned above, CAM-B3LYP functional blue shifts the overall optical spectra increasing the exciton binding energy. Since the Frenkel exciton typically possesses a relatively larger binding energy than charge-transfer exciton [196], it is predicted by CAM-B3LYP functional. It further indicates the long-range corrected functional not only blue shifts the spectra but also changes the character of excited state giving artificial transition states. Such discrepancy originates from the implementation of exact exchange terms in both functionals, where the long-range corrected functional changes the percentage of exact exchange according to the electron-electron distance giving two potential energy terms - short range and long range interactions, while the standard functional only has a fixed exact exchange. This gives rise to different optical

transition especially for the lowest transition, since for CAM functional the short and long range electron-electron interaction is determined by parameters (μ, α, β) that are system-dependent, while the parameters in B3LYP functional are more robust for the prediction of optical gap and band gap [80], especially, the latter one is largely tested for modelling ligated QDs. In addition, we are fully aware that the hybrid B3LYP functional is well known for the instable prediction of charge-transfer excitation in metal complexes [197-199], where there is a strong bonding between metal ion and related ligands. On the contrary, QD-dye composite is a typical donor-acceptor system with weak interaction, such charge-transfer excitation is mainly governed by the orbital resonant interactions provided by the energetic alignment, as such, B3LYP gives more accurate prediction than CAM-B3LYP, since CAM-B3LYP overestimates the band gap of QD resulting in an inaccurate energetic alignment between QD and dye.

Table 5 shows the charge density difference between the excited state and ground state for all bright transitions between the wavelength of 600 nm and 400 nm. All CT excitonic states have very significant charge localization characters.

Table 5. Charge density differences (CDDs) of $Cd_{33}Se_{33}$ QD/$[Me(II)(bpy)_2(mcb)]^{1+}$ dye nanocomposite between the excited states and ground state for all the bright transitions with oscillation strengths (f) larger than 0.1. The energy window of excitation is between 600 nm and 400 nm, and calculated by B3LYP functional. Green color represents holes and red color represents electrons. The calculations are performed in CH_3Cl.

Ru(II)	Cr(II)	Cd(II)	Os(II)	Fe(II)
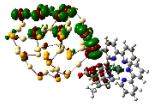	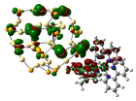	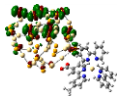	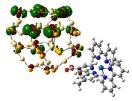	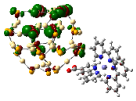
f=0.29	f=0.25	f= 0.50	f= 0.50	f=0.41
442 nm	440 nm	441 nm	441 nm	441 nm
	CT state			

Table 5. Charge density differences (CDDs) of $Cd_{33}Se_{33}$ QD/[Me(II)$(bpy)_2$(mcb)]$^{1+}$ dye nanocomposite between the excited states and ground state for all the bright transitions with oscillation strengths (f) larger than 0.1 (continued). The energy window of excitation is between 600 nm and 400 nm, and calculated by B3LYP functional. Green color represents holes and red color represents electrons. The calculations are performed in CH_3Cl.

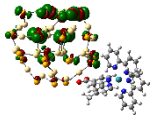	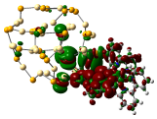	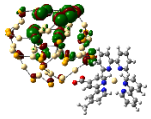	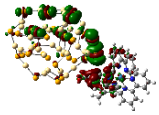	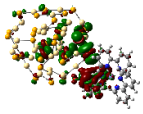
f=0.43	f=0.34	f= 0.28	f= 0.20	f= 0.13
441 nm	433 nm	440 nm	440 nm	435 nm
	CT state		**CT state**	**CT state**
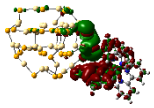	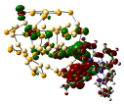	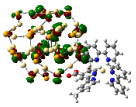	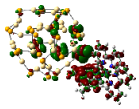	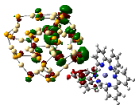
f=0.18	f=0.15	f= 0.34	f= 0.19	f= 0.32
436 nm	427 nm	434 nm	436 nm	431 nm
CT state	**CT state**		**CT state**	
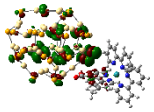	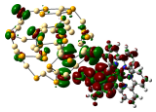	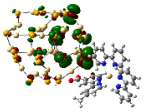	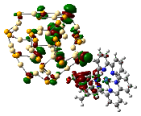	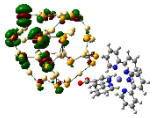
f=0.29	f=0.24	f= 0.33	f= 0.32	f= 0.29
435 nm	424 nm	431 nm	432 nm	429 nm
	CT state		**CT state**	
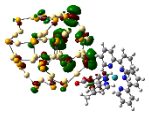	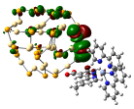	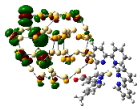	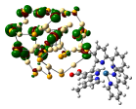	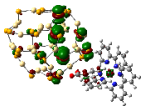
f=0.33	f=0.17	f=0.28	f=0.17	f= 0.28
432 nm	419 nm	428 nm	429 nm	428 nm
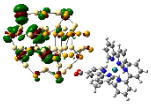		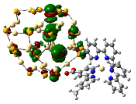	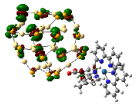	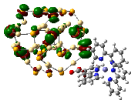
f=0.30		f=0.34	f=0.33	f=0.11
427 nm		427 nm	428 nm	422 nm

Table 5. Charge density differences (CDDs) of $Cd_{33}Se_{33}$ QD/$[Me(II)(bpy)_2(mcb)]^{1+}$ dye nanocomposite between the excited states and ground state for all the bright transitions with oscillation strengths (f) larger than 0.1 (continued). The energy window of excitation is between 600 nm and 400 nm, and calculated by B3LYP functional. Green color represents holes and red color represents electrons. The calculations are performed in CH_3Cl.

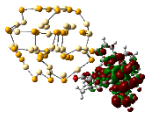	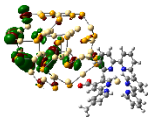	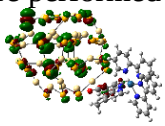	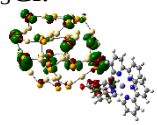
f=0.16	f=0.23	f=0.16	f=0.13
426 nm	421 nm	427 nm	421 nm
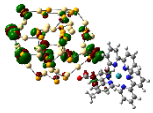	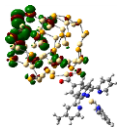	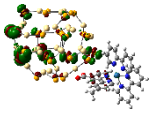	
f=0.16	f=0.23	f=0.19	
421 nm	420 nm	421 nm	
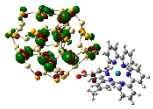			
f=0.12			
417 nm			

There are four and three CT excitonic states in Cr(II) and Os(II) dye-functionalized $Cd_{33}Se_{33}$ QDs, respectively, while in cases of Fe(II) and Ru(II) dye-functionalized $Cd_{33}Se_{33}$ QDs there is only one CT excitonic state. For Cd(II) dye-functionalized $Cd_{33}Se_{33}$ QD only Frenkel excitons localized in QD are present. We further perform the Eigen-vector analysis, in which the excitonic wavefunction is expanded as a linear combination of the occupied and unoccupied molecular orbitals, i.e. hole-electron pairs. We found, for each CT excitonic state, the holes are localized in QD, while the electrons are localized in dye. Therefore, those CT excitonic states are indeed representing the charge-separated states. We also noted, the main difference between Os(II)- and Cr(II) dye functionalized $Cd_{33}Se_{33}$ QDs, and Fe(II)-, Ru(II)- and Cd(II) dye

functionalized $Cd_{33}Se_{33}$ QDs are: first, the HOMOs of these two dyes are closer to the VB edge than the other three dyes (Figure 13 (b)) increasing the electronic coupling of dye to the surface states of $Cd_{33}Se_{33}$ QD, as a large amount of frontier molecular orbitals of CdSe QD is distributed at the surface [185] that is readily resonated with dye's HOMO orbitals. Second, the dipole moment in QD/dye composite is pointed from the dye towards the QD, where the positive charges are localized in dye, while the negative charges are localized in QD, as such, the dipole-dipole interaction easily delocalizes electrons from QD to dye upon the photoexcitation. As indicated earlier, the dipole-dipole interactions in cases of Cr(II)- and Os(II) dye functionalized $Cd_{33}Se_{33}$ QDs are larger than the other dye functionalized $Cd_{33}Se_{33}$ QDs, consequently, it increases the CT excitonic states in these two dye functionalized QDs. The charge transfer excitons bring the disadvantage for CdSe QDs based solar cell since the charge carriers flow to the opposite side of the charge collecting electrode; however it benefits the scheme of QD-dye bisensitizer with QD as co-sensitizer since the electron injections of dye sensitizer are largely enhanced by QD. A similar idea has been successfully applied to the dye sensitized anatase-based TiO_2 solar cells, in which the charge-transfer excitons increases the overall conversion efficiency by orders of magnitudes [38].

4.2. Summary

To summarize, our DFT calculations demonstrate that, changing metal ion aligns dye's HOMO and LUMO with respect to the VB edge and CB edge of $Cd_{33}Se_{33}$ QD, respectively. In particular, increasing the electronegativity decreases the energy difference between the HOMO of dye and VB edge of QD, and increases the energy difference between the LUMO of dye and CB edge. However, tuning metal ion does not provide the favorable condition for hole transfer.

The distributed multipolar analysis suggests, even though the dipole interaction for QD/dye composite based on our calculation is a small quantity (around 5.0 eV) with respect to the total energy, it perturbs the QD-dye energetic alignment decreasing the size of d_{z^2}-orbital. Therefore, no matter for experimental measurement or theoretical modelling an accurate description of such interaction is important for determining the QD-dye energetic alignment.

Our TDDFT calculations suggest, changing metal ion changes the lowest optical transition as well as the first absorption peak in QD/dye composite. B3LYP and CAM-B3LYP both provide a good additive feature on the simulated spectra, i.e. the curvature of bare QD adds the curvature of isolated dye approximately matches the curvature of QD/dye composite. Both functional predict the first absorption peaks of Cr(II) and Os(II) dye-functionalized $Cd_{33}Se_{33}$ QDs originated from metal-ligand and π,π^* transitions, while in cases of other dye-functionalized $Cd_{33}Se_{33}$ QDs the first absorption peak originate from the metal-metal transition. For the lowest optical transition, CAM-B3LYP tends to predict a Frenkel exciton, while B3LYP tends to predict a charge-transfer exciton. Moreover, a small energy difference of the HOMO of dye with respect to the VB edge, as well as a large dipole-dipole interaction increases dye's resonant interaction with QD's surface states, consequently, more charge transfer characters occur in the bright optical transitions. This brings additional tunability for controlling the charge carrier mobility to satisfy some special purposes of photovoltaic device.

CHAPTER 5. EFFECT OF LIGANDS ON ENERGETIC ALIGNMENT AND EXCITED-STATE PROPERTIES

In this chapter we theoretically elucidate the effect of ligand charge in the Ru(II)-complexes on the relative alignments of the energy levels associated with the QD and the dye by performing DFT and TDDFT calculations. The energetic alignment between the QD and dye provides insights in possible direction of the charge transfer in these complexes. As such, our DFT simulations of the geometries, electronic structures, and optical responses of model CdSe QDs functionalized by Ru(II) trisbipyridine and the BD dye, allows us to elucidate the charge transfer trends in these systems as a function of Ru-complex ligand.

5.1. Results and Discussion

Experimental studies have demonstrated that the surface passivating layer of CdSe QDs can be effectively functionalized with Ru(II) polypyridine complexes, such as Ru(II)bpy [40, 42] and the black dye [45, 46]. In these molecules, addition of one or several carboxyl groups at the ligand sites provide chemical bonding of the complex to the QD surface. Therefore, here we focus on two different types of Ru(II) complexes. One molecule includes only 2,2′-bipyridine ligands (bpy) functionalized by one (complex 1) and two (complex 2) carboxylic acid and methyl groups (mcb) in their completely deprotonated (1a and 2a) or protonated (1 and 2) forms, similar to those experimentally studied in refs [42] and [40]. We also model similar Ru(II)bpy complexes with three (complex 3a) and four (complex 4a) deprotonated carboxylic acid groups, as illustrated in Figure 6. The carboxylate linker anchors complexes 1 and 2 to one of the Cd atoms on the QD surfaces via the monodentate attachment. For the deprotonated complexes, the initial attachment is chosen to be the bridging mode, when each oxygen of the carboxylate group is bound to the metal sites of

the QD surface (QD/1a and QD/2a in Figure 18). This attachment has been found to be the most energetically favorable for CdSe-Ru(II)bpy composites [40, 81].

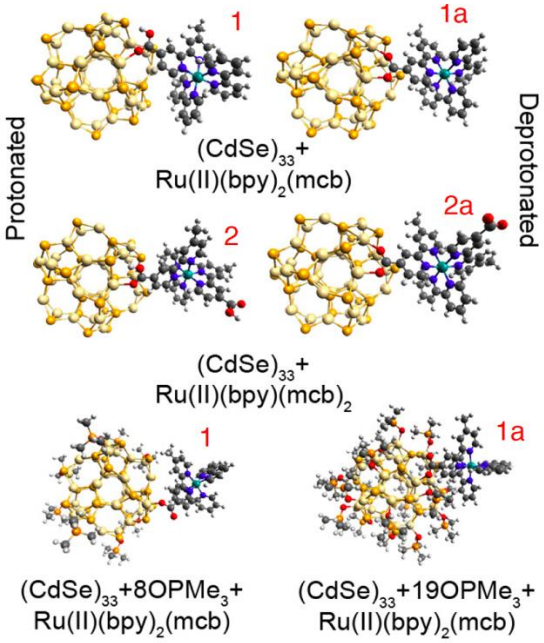

Figure 18. Optimized geometries of $Cd_{33}Se_{33}$ quantum dots (QDs) functionalized by Ruthenium(II)-2,2-bipyridine complexes with one carboxyl group $[Ru(II)(bpy)_2(mcb)]^{1+}$, complex 1, or two carboxyl groups $[Ru(II)(bpy)(mcb)_2]^0$, complex 2. Left and right columns illustrate the protonated (1 and 2) and deprotonated (1a and 2a) complexes attached to the surface of $Cd_{33}Se_{33}$ in the bridging mode, respectively. The bottom are Ru(II) functionalized QDs passivated by 8 OPMe3 ligands (left) and 19 OPMe3 ligands (right).

The second type is the black dye (BD) studied in refs [45] and [46], where the Ru(II) ion is coordinated by three isothiocyanate ligands (SCN^-) and the 2,2′:6′,2″-terpyridine (tpy) is functionalized by three carboxyl groups, as illustrated in Figure 19. In addition, we simulate modified versions of the BD in which the isothiocyanates are substituted by Cl^- or CO ligands to consider the effect of negatively charged versus neutral ligands on the electronic properties of the QD-dye composites. For the BD, we consider two possible attachments: similar attachment to complexes 1a and 2a via the deprotonated carboxylate group in its bridging mode (BD-c, Figure 19) and the anchoring via the thiocyanate group (QD/ BD-t, Figure 19).

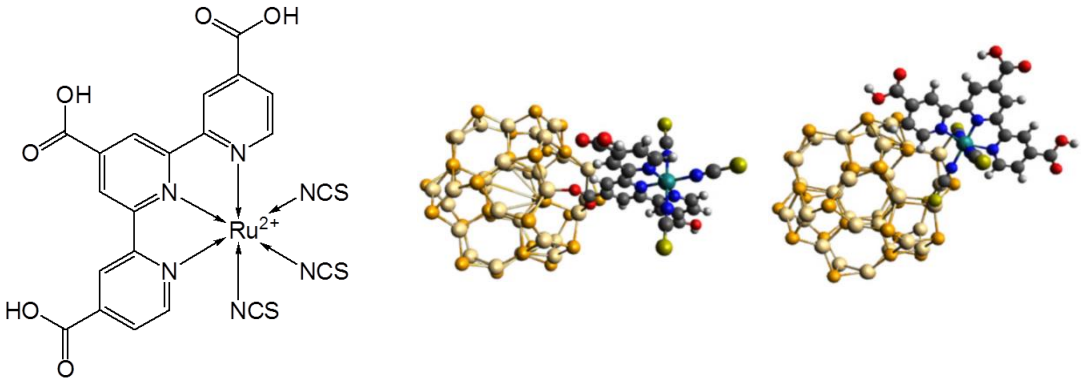

$Ru^{2+}(ctp)(NCS^{-})_3$ **QD/BD-c** **QD/BD-t**

BD

Figure 19. Structures of the systems we studied. On the left, the schematic structure of black dye (BD). Middle and right panels show the $Cd_{33}Se_{33}$ functionalized by the black dye attached via the carboxylate (QD/BD-c) and isothiocyanate (QD/BD-t) groups.

The black dye is negatively charged having −1 and −2 charges in its BD-t and BD-c forms, respectively, due to the SCN^- groups and deprotonated carboxylate linker.

5.1.1. Mutual energy alignment of dye and QD states

Figure 20 shows the projected density of states (PDOS) and, thus, identifies single-electron Kohn−Sham orbitals, which contribute to a specific energy range, as either QD or complex associated states. The unoccupied states belonging to the dyes appear near the edge of CB independent of the complex, its attachment, its protonated state, or the presence of OPMe3 ligands. These states are mainly localized on the bpy or tpy ligands of the Ru(II) complexes. The 3-D view of these orbitals, shown in Figure 21, confirms their strongly dye-localized nature with negligible traces of orbitals leaking to the QD surface, which explains their weak response to changes in the surface or the anchoring groups. The OPMe3 ligands are found to introduce their electronic states deep inside the CB and VB of the QD, as marked by the gray line in Figure 20 (d). This implies that passivating ligands can barely perturb any the frontier orbitals at the CB edge as well as at the VB edge.

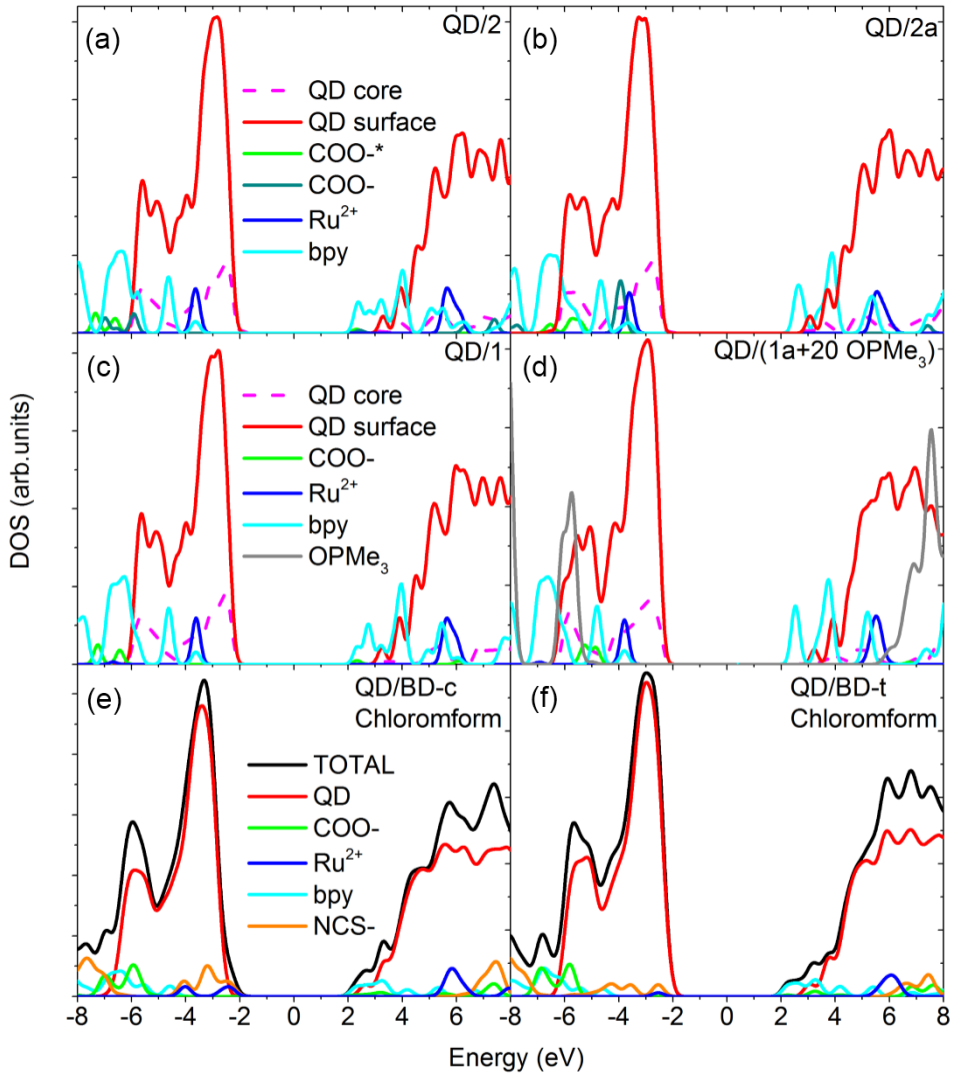

Figure 20. PDOS of the $Cd_{33}Se_{33}$ QD functionalized by derivatives of Ru(II)-bipyridines (a−d) and the black dye (e−f). Calculations are done by CAM-B3LYP functional in chloroform. Zero energy is chosen at the middle of the HOMO−LUMO gap for all systems. The PDOS represents the contributions from the QD's surface (red) and core (dashed magenta) atoms, the Ru(II) ion (blue), the bipyridine (bpy) and terpyridine (tpy) ligands (cyan), the carboxylate (COO) groups (green for nonanchoring and teal for anchoring), thiocyanate groups (orange), and the passivating ligands OPMe3 (gray). The orbitals near the edge of the CB originate from the complex orbitals, independent of the complex. Orbitals associated with Ru(II) ion are deep inside in the VB of the QD functionalized by the Ru(II)-bipyridines, but are at the edge of the QD's VB for the black dye functionalization.

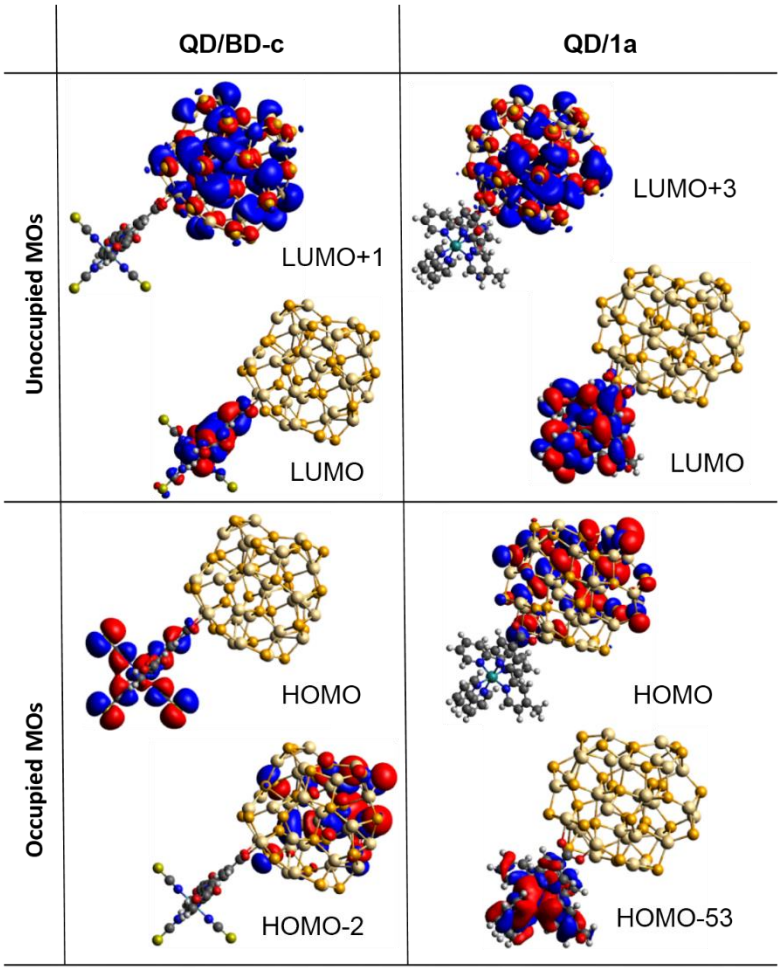

Figure 21. Representative molecular orbitals (MOs) of $Cd_{33}Se_{33}$ QD functionalized by the complex 1a (right panels) and the black dye (left panels). Calculations are done by CAM-B3LYP functional in chloroform.

The occupied orbitals associated with the complex are, however, strongly affected by the type of ligands in the complex. In fact, in complexes 1 and 2, the dye's occupied orbitals, mostly localized on the Ru(II) ion with a small hybridization over bpy ligands, appear deep inside the VB, while the edge of the VB is dominated by the QD's states. The protonation of the anchoring carboxyl group and a full coverage of the QD surface by OPMe3 ligands insignificantly changes the relative position of the dye's orbitals versus the QD's states: they stay deep inside the VB of the QD. Such insensitivity originates from a predominantly localized character of Ru(II) orbitals,

which have negligible contributions from the carboxylate or the QD atoms, as illustrated in Figure 21, right panel. It is important to note that similar trends in energy alignment of the orbitals of Ru(II)bpy complexes versus the QD's orbitals have been computationally predicted for PbSe and ZnO QDs [81], demonstrating that the alignment of electronic states is only slightly affected by the chemical composition of the QDs, which does not change the qualitative trends.

When the bipyridine ligands are substituted by the isothiocyanate ligands, the occupied orbitals of BD originating from the Ru(II) possess a significant hybridization between the SCN ligands and anchoring carboxyl group, as seen in Figure 21, left panel. As a result, the BD orbitals are shifted to the very edge of the VB of the QD, Fig 5.2 e,f. Attachment of the BD to the QD surface via the sulfur in the thiocyanate ligand slightly shifts the Ru(II) orbital by ~0.2 eV toward the VB, pointing to a sensitivity of these states to the dye-QD interactions. Note that the calculated QD-dye binding energy is stronger for BD-c with a carboxyl linker (−0.18 eV) than for BD-t attached to the QD via the SCN ligand (−0.12 eV), predicting a dominant adsorption of the dye via the carboxyl group. However, even if the less favorable attachment of the BD-t happens via the thiocyanate group, the occupied orbitals of the black dye are closer to the VB edge than the orbitals of Ru(II)bpy complexes. As such, the thiocyanate ligands are responsible for aligning the dye's occupied orbitals at the edge of the VB of the QD. Negatively charged thiocyanate ligands destabilize the highest occupied molecular orbital (HOMO) of the complex, lifting it closer or even above the VB edge of the QD.

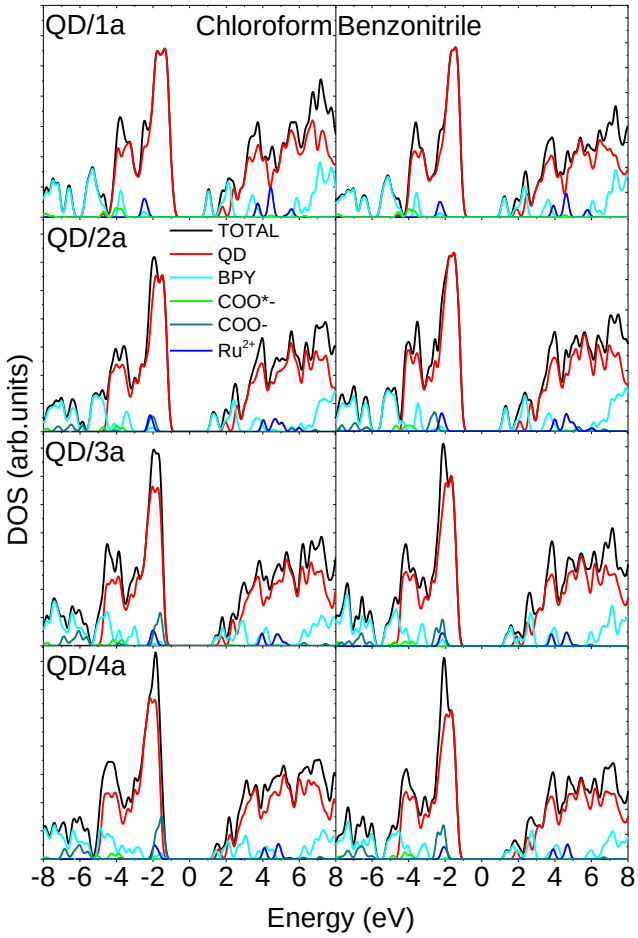

Figure 22. Projected density of states (PDOS) of $Cd_{33}Se_{33}$ QDs functionalized with Ru(II) dyes bearing different charge: -1, 0, 1 and 2, respectively. Schematic structures of dye complexes are shown in left column. Middle column and right column are PDOS of QDs functionalized with different Ru(II) dye in Chloroform and Benzonitrile, respectively. All functionalized QDs are calculated by B3LYP functional. A mixed basis set is applied to all atoms, where LANL2DZ basis set is used for heavy atoms (Cd, Se, Ru) and 6-31G* is used for the other atoms (C, H, Ru, O).

To better understand the effect of the dye's ligand on the mutual alignment of the molecule's versus the QD's electronic levels, first we investigate the role of the charge on the peripheral groups, carboxylates, which are not directly involved in the coordination with Ru(II) ion. For this, one (1a), two (2a), three (3a), and four (4a) deprotonated carboxylic acid groups are added to bipyridine ligands in the Ry(II)bpy complex, resulting in a total charge of +1, 0, −1, and −2, respectively. Independent of the number of the carboxylate groups and the total charge of the

complex, the lowest-energy occupied orbitals of the Ru(II)−polypyridine stay inside the VB of the QD, while the dye's unoccupied orbitals contribute to the QD's band gap close to the CB edge, when calculated in a polar solvent like benzonitrile (Figure 22, right panel). The key role of the isothiocyanate ligands on the destabilization of the dye's occupied orbitals is confirmed by the trend in mutual shifts of the QD- and dye-originated states in solvents of different polarities, as shown in Figure 23. For both BD-c and 1a complexes adsorbed on the $Cd_{33}Se_{33}$, a polar solvent significantly shifts the dye-associated orbitals with respect to the QD's states.

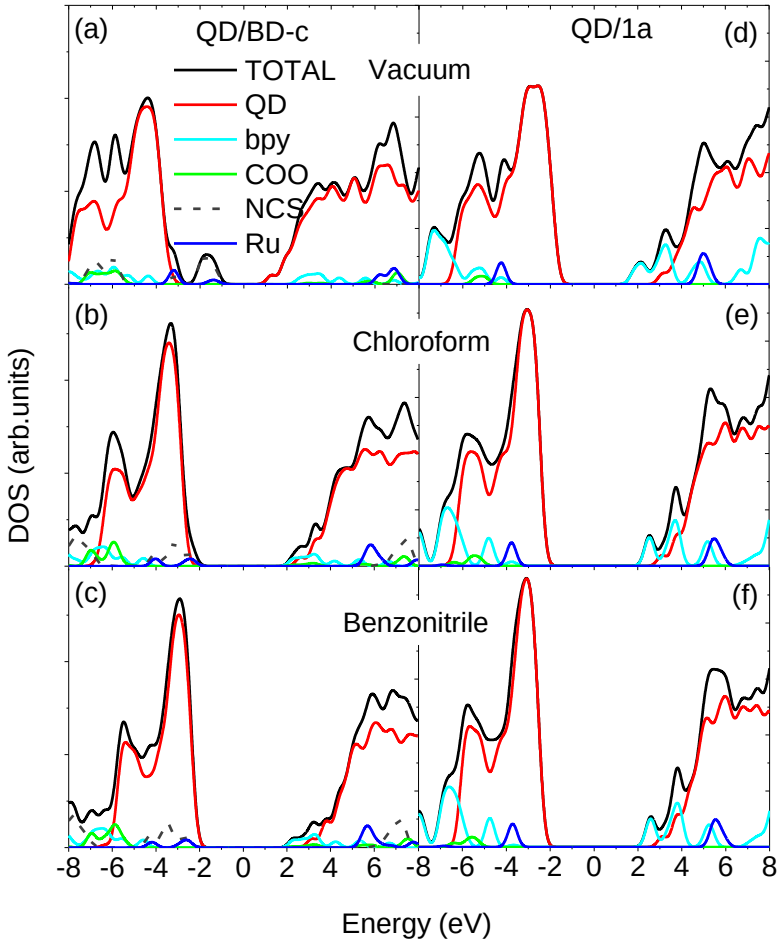

Figure 23. Dependence of the PDOS of $Cd_{33}Se_{33}$ functionalized by the complex 1a (left panels a−c) and the black dye (right panels d−f) on the solvent polariry. PDOS is calculated by CAM-B3LYP functional in vacuum (a and d), chloroform (b and e) and benzonitrile (c and f). The line colors corresponding to contributions of different parts of systems are kept the same as in Fig 5.2. Zero energy is chosen at the middle of the HOMO−LUMO gap for all systems.

However, in the complex 1a with bpy ligands, the polar solvent shifts the orbitals of the complex to higher energies, while orbitals of BD-c with SCN ligands are shifted toward lower energies. In fact, the occupied orbitals of BD-c are nearly at the midgap of the QD when the system is calculated in vacuum, while they move away from the gap, deeper into the VB with increasing solvent polarity (from chloroform to benzonitrile; Figure 23, left panel). Accordingly, the unoccupied states associated with tpy ligands are shifted in the CB toward its edge, when the QD/BD is calculated in benzonitrile. For complex 1a, this trend is reversed. This reverse shift of the dye's orbitals for QD/Ru(II)bpy versus QD/BD originates from an opposite charge on the complexes: +1 for the complex 1a and −2 for BD-c. In fact, similar to the QD/BD, the composites with 3a and 4a complexes having −1 and −2 charge due to additional deprotonated carboxylate groups demonstrate a slight shift of the dye's occupied orbitals further away from the edge of the VB with increases in the solvent polarity, while the dye's unoccupied orbitals move inside the QD's gap. This confirms that the sign of the total charge of the dye is the key factor governing the trend of stabilization or destabilization of the dye's orbitals in polar media.

The energy gap of the QD is also affected by solvent, increasing by about 0.3 - 0.5 eV with the solvent polarity, which agrees with previous computational reports [81]. A polar solvent stabilizes the surface states of the QD, while negligibly impacting the states localized at the inner (core) part of the QD. This increases the energy gap of the QD, since its HOMO and, especially, its lowest unoccupied molecular orbital (LUMO) have a lot of surface character, as seen in Figure 21. However, the complex's orbitals are much more strongly affected by solvent than the QD's states due to the larger electrostatic dipole moment of the complexes, compared to the QD. Therefore, a polar solvent has a stronger effect on the complex's states than the QD's states, resulting in either stronger destabilization of electronic levels of the Ru(II)bpy complexes with a positive charge or

stronger stabilization of states associated with the black dye holding a negative charge. Thus, our calculations suggest that solvents with different polarities can be used to tune a mutual alignment of the dye's versus the QD's orbitals.

Despite the fact the negative charge on the dye helps to align the dye's orbitals closer to the band gap of the QD in nonpolar or weakly polar solvents, the Ru-associated orbitals in the 3a and 4a dyes are further away from the edge of the VB in the case of QDs functionalized by Ru(II)bpy than in QD/BD composites, when calculated in chloroform. In addition, complete deprotonation of carboxylic groups might not take place in experimental samples, if pH is not controlled. As such, the negatively charged peripheral groups do not destabilize the dye's occupied orbitals as efficiently as the isothiocyanates, which are directly coordinated with the Ru(II) ion. To elucidate the role of the negative charge on the ligands coordinating the Ru(II) ion, we have modeled two derivatives of the BD with isothiocyanate groups substituted by Cl^-, $[Ru(cpt)(Cl)_3]^{-1}$, and by CO, $[Ru(cpt)(CO)_3]^{+2}$, as depicted in Figure 24. The effect of the Cl^- ligands is very similar to the SCN^- groups: the occupied orbitals originating from these ligands are destabilized and shifted up to the edge of the QD's VB. The multiple bonds of the SCN^- ligands seem to play an insignificant role in the orbital destabilization: the complex with the Cl^- ligands, which do not have any triple or double bonds, results in a similar destabilization as the BD with SCN^- ligands. In contrast, neutral CO groups, with stronger electron withdrawing character than the Cl^- group, greatly stabilize the Ru-ion orbital and shift it even deeper into the VB of the QD, as compared to the QD functionalized by 1 or 2 complexes in chloroform. Consequently, it is the negative charge of the coordinating ligand that controls the destabilization of the dye's occupied orbitals in the QD/dye composites.

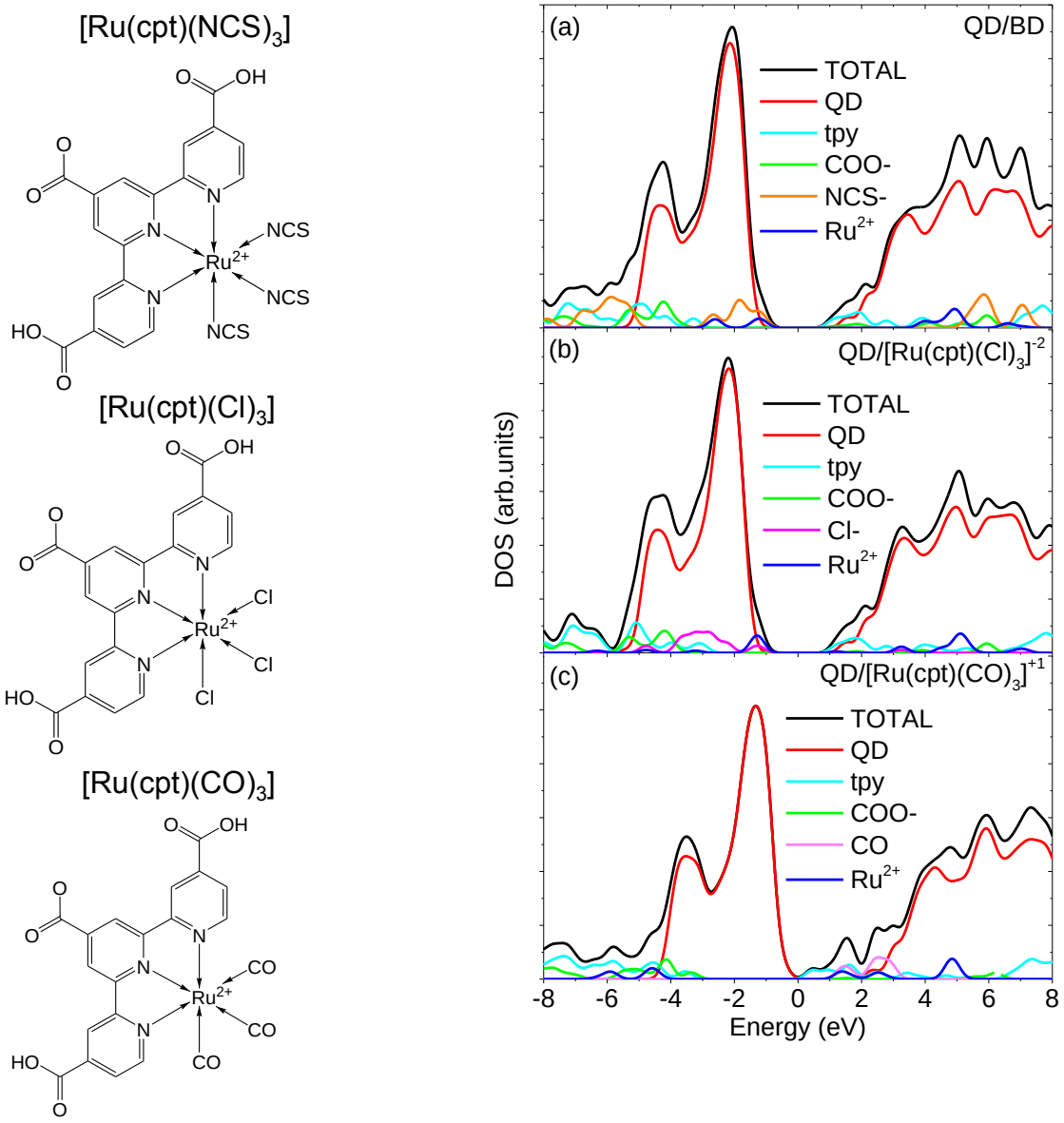

Figure 24. Projected density of states (PDOS) of $Cd_{33}Se_{33}$ QDs functionalized with derivatives of black dye (a-c) in Chloroform. Left column is the schematic structures of three derivatives of black dye, and right column is the PDOS of corresponding functionalized QDs.

We note that calculations presented in Figure 22 and in Figure 24 are obtained by the B3LYP functional, while our other calculations utilize CAM-B3LYP functional. Comparison of data for the QD/BD in Figure 20 and Figure 23 together with data for QD/1a and QD/2a depicted in Figure 20 and Figure 22 demonstrate that both functionals provide similar shapes for the

projected DOS and qualitatively identical behavior of the electronic structure of the composites. However, CAM-B3LYP strongly overestimates the energy gaps of both the dye and the QD, due to a larger portion of HF exchange in the functional. In contrast, B3LYP provides more reasonable gap estimates of about 3 eV for the $Cd_{33}Se_{33}$ and 2.5 eV for Ru(II)bpy dyes, which are in better agreement with available experimental data [163]. As such, the overall trend in relative energy alignments of QD's and dye's states is consistent, independent of the functional, although the absolute values of energies are off. Therefore, we can conclude that the qualitative picture of the electronic structure of QD/dye composites is not changing with the functional. A similar conclusion for QDs was discussed in refs [81] and [161]. Confinement of charge carriers in the QD is expected to significantly affect the alignment of the dye's versus the QD's orbitals as well. To elucidate the effect of the QD's size, we compare the DOS of the large $Cd_{111}Se_{111}$ with the small $Cd_{33}Se_{33}$ clusters in vacuum and in the benzonitrile solvent, as depicted in Figure 25. As expected, an increase in the QD size from 1.5 to 2.2 nm leads to a smaller band gap. However, the confinement affects the CB more than the VB of the QDs. Thus, the VB edges have nearly equal energies in both small and large CdSe QDs, while the edge of the CB is red-shifted by about 2 eV in vacuum and 1.5 eV in solvent for the $Cd_{111}Se_{111}$. Such a difference in the VB and CB behavior originates from heavier holes, with the effective mass 4 times that of electrons in CdSe. Therefore, the VB edge is less sensitive to the confinement, compared to the edge of the CB. As such, it is reasonable to assume that, in the dye-functionalized QDs of a larger diameter, the occupied states associated with the dye are likely to stay at about the same position with respect to the VB as they are in smaller CdSe clusters. In contrast, the unoccupied orbitals of the dye likely occur deeper inside the CB of the QDs with diameters larger than 2 nm.

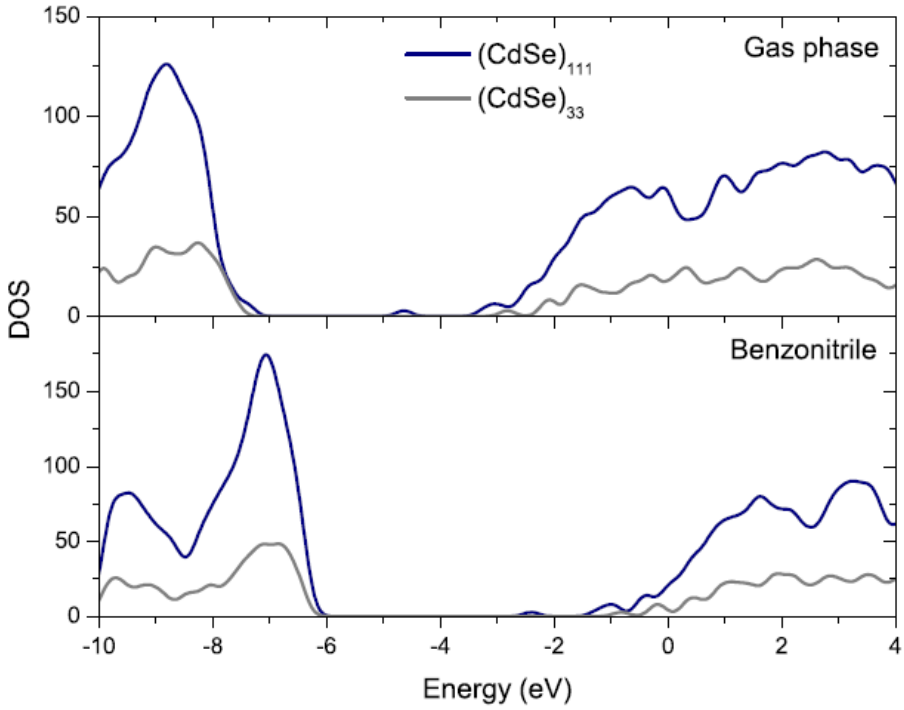

Figure 25. Comparison of the DOS for two sizes of bare QDs in vacuum (top) and benzonitrile solvent (bottom). Calculations are done by CAM-B3LYP functional. The DOS confirms what is expected from effective mass theory: As size increases, the band gap shrinks mainly through the conduction band of light electrons, moving closer in energy to the essentially static valence band formed by heavy holes.

5.1.2. Band offsets: role of QD-dye interactions

Experimentally, it is challenging to directly determine the energy differences between HOMO of the dye and the QD in QD/dye composites. Therefore, these energy offsets are usually estimated from the electrochemical measurements of the isolated metal complexes and the QDs. The electrochemical measurements of $[Ru(II)(bpy)]^{+2}$ complex show an oxidation potential value of 1.26 V versus normal hydrogen electrode (NHE) in acetonitrile [200]. For many related complexes, the oxidation potential is estimated at the range of 0.69 - 1.77 V depending on the substituted ligands and experimental conditions [201]. The oxidation potentials for the CdSe QDs estimated from electrochemical and optical studies vary from 1.0 to 2.0 V vs NHE, depending on surface passivation, extent of traps, and even measurement conditions [202]. As such, by roughly judging

from the measurements of the isolated components, the HOMO energy difference between the dye 1a and the CdSe QD lays in the range from 1.2 to - 0.2 eV, where the negative sign implies that the dye's HOMO is higher in energy than the HOMO of the QD.

Similarly, computational determination of the band offsets is a subject of many uncertainties, given the differences between the model used in the calculation and the actual experimental conditions. In the experiment, the QDs used are substantially larger than those used in the calculations. Additionally, the calculations are conducted at zero temperature and by approximating the solvent as a dielectric continuum, while the experiments have been performed under ambient conditions. However, since our calculations suggest that the VB edge of CdSe is not very sensitive to the size of the QD, the size difference in the QDs between calculations and experiments should not be of major consequence for determining the HOMO offsets. Thermal fluctuations could also affect the results; however, our calculations were performed at the equilibrium geometry, and most fluctuations should occur around this geometry leading to an averaging out of the fluctuation effects. Lack of explicit solvent molecules in the calculations could also affect the quality of our results. For the properties in which we are interested, however, the dominating contribution from the solvent should be from electrostatics rather than, for instance, hydrogen bonding. Since the absolute values of the electronic energies are not accurate reference values, we have chosen the lowest energy of a core 1s electron of the carbon from the methane group in the dye 1a and in the phosphine oxide ligands passivating the $Cd_{33}Se_{33}$ surface as the reference point for both isolated systems. For the noninteracting dye and the QD, the calculated energy difference between their HOMOs varies from 0.03 to 0.5 eV depending on a solvent (see Table 6), which is in a reasonable agreement with the experimental values discusses above (ranging from −0.2 to 1.2 eV). This demonstrates an acceptable qualitative validity of used

methodology despite all approximations. Compared to the $Cd_{33}Se_{33}$/1a case, calculations of the isolated black dye and the $Cd_{33}Se_{33}$ cluster show the offset occupied energies to be negative, i.e., the BD's HOMO is by ~4.5 eV higher than the HOMO of the QD, which slightly increases for less polar solvents like chloroform, as shown in Table 6.

Table 6. Difference between Energies of the Highest Occupied Orbitals of the Dye and the QD ($\Delta E = HOMO_{QD} - HOMO_{dye}$) in eV and the Dipole Moments (μ) in Debye[a]

	QD-ligated/1a					QD/BD			
Solvent	ΔE_{nonint}	ΔE_{int}	$\mu_{QD-nonint}$	$\mu_{dye-nonint}$	μ_{int}	ΔE_{nonint}	ΔE_{int}	$\mu_{dye-nonint}$	μ_{int}
Chloroform	0.03	1.19	21.57	113.30	81.00	-4.55	-0.35	87.13	44.87
Benzonitrile	0.46	1.01	22.53	114.89	82.03	-4.44	0.19	87.71	47.45
Acetonitrile	0.47	1.00	22.61	115.10	82.09	-4.46	0.24	87.75	47.65

[a] Two cases are compared: the non-interacting (ΔE_{nonint}, $\mu_{QD-nonint}$, and $\mu_{dye-nonint}$) isolated and optimized complexes 1a, BD, and the $Cd_{33}Se_{33}$ passivated by OPMe3 ligands versus the interacting (ΔE_{int} and μ_{int}) QD/dye composites of the ligated $Cd_{33}Se_{33}$ functionalized by 1a (QD-ligated/ 1a) and by BD (QD/BD) dyes. For the QD/BD composite, the QD is not ligated by OPMe3. For each isolated systems, the energy of the HOMO is taken with respect to the energy of the core 1s electron of the carbon in a methane group. All calculations are performed with B3LYP functional and LANL2DZ(heavy atoms)/6-31G*(light atoms) basis set.

Having established the consistency between experimental and calculated values for band offsets for individual components, we further notice that the calculated difference between the HOMO associated with $Cd_{33}Se_{33}$ and 1a (or BD) in the interacting QD/1a (or QD/BD) complex substantially changes when compared to noninteracting case as summarized in Table 6 Specifically, as shown in Figures 22, 23, and Table 6, the HOMO predominantly originating from the 1a molecule is more negative by about 1.2 eV than the edge of the QD's VB, when calculated in chloroform and by 1.0 eV in benzonitrile. Similarly, interactions between the QD and the dye dramatically stabilize the dye's HOMO to about 0.2 eV below the QD's HOMO in QD/BD composites in polar solvents. Our observations suggest that electrostatic dipole− dipole coupling (more generally Coulombic interaction ofinhomogeneous electronic densities) between the QD

and the dye are responsible for these stabilization of the dye's orbitals with respect to the QD's VB edge. This effect is similar to the energy reorganization in polar solvent, when the electrostatic interactions between solvent molecules and a solute results may lead to a significant stabilization of electronic levels of a system.

In our case, both the dye and the QD have strong dipole moments, as recorded in Table 3.1. In fact, the calculated dipole moment of the CdSe QD is about 22−23 D, increasing with the solvent dielectric constant, which remarkably agrees with the experimental values of dipole moments of CdSe colloidal QDs measured as 25 and 47 D for 3 and 5 nm diameter nanocrystals [203]. The dipole moments of dyes is much higher. However, in the interacting system, the total dipole moment of the QD/dye composite becomes 1.5 - 2 times smaller than those of the isolated dye. This signifies a redistribution of the electronic density of the composite and results in stabilization of dye's orbitals. To decrease the dipole moment of the dye's part in the QD/dye composite, the electronic charge density should shift toward the Ru(II) center, rather than to the linking carboxylate group, leading to a more localized character of the dye and QD associated orbitals in composites, despite relatively strong dye-QD interactions. Overall, our results clearly demonstrate the dominating role of the QD-dye interactions on the mutual alignment of their electronic levels, resulting in stabilization of the dye orbitals with respect to the QD's VB edge. Subsequently, the energy offsets in the composites does not represent a simple difference of the isolated metal complexes and the QDs, which should be accounted for in experimental studies.

Indeed, the stabilization effect observed in our modeling is qualitative given a limited number of configurations considered. In the realistic systems these shifts are expected to depend on the detailed structure of the nanocrystal, attachment of the dyes with respect to the QD dipole moment direction, density of surface dye coverage, and ligand surface chemistry. While complex,

this is expected to be an additional tunable parameter for arranging a favorable energetics in the future studies. Nonetheless, our calculations demonstrate that the attachment of the complex 1a to different surfaces of the $Cd_{33}Se_{33}$ (A, B, and D surfaces illustrated in Figure 6) changes the HOMO offset energies by less than 0.1 eV, as depicted in Table 7. This small change in the energy alignments between the dye's and QD's HOMO is accompanied by a change in the total dipole moment by 5−15 D, depending on the interacting surface. Although the dependence of the dipole moment on the dye attachment is noticeable, it ismuch smaller than the change in the dipole moments associated with the QD−dye interactions (compare data in Tables 7 and 8), resulting in more significant changes in the energy offsets (0.6−1 eV) due to the QD−dye interactions than due to the adsorption of the dye to different QD's surfaces. The presence of the passivating ligands (Tables 6) also changes the offset energies by less than 0.1 eV, as compared to the case of the nonpassivated $Cd_{33}Se_{33}$ with the dye 1a attached to the A surface shown in Table 7. As such, the QD−dye interaction is the dominant factor in stabilization of the dye's levels with respect to the QD's states, while the surface chemistry of the QDs only slightly adjusts the energy offset values.

Table 7. Difference between Energies of the Highest Occupied Orbitals of the Dye and the QD ($\Delta E = HOMO_{QD} - HOMO_{dye}$) and the Dipole Moments (μ) of $Cd_{33}Se_{33}$/1a Composites in Different Solvents with the Complexes 1a Attached to Different Surfaces Labeled As A, B, and D[a]

	acetonitrile		benzonitrile		chloroform	
Surface	ΔE (eV)	μ (Debye)	ΔE (eV)	μ (Debye)	ΔE (eV)	μ (Debye)
A	0.93	92.60	0.95	92.43	1.06	89.90
B	0.90	103.09	0.93	103.02	0.95	101.86
D	0.98	86.62	0.98	86.52	1.12	85.78

[a] All calculations are performed with B3LYP functional and LANL2DZ(heavy atoms)/6-31G*(light atoms) basis set.

5.1.3. Thermodynamic conditions for charge transfer

Overall, our calculations of the electronic structure of the dye functionalized $Cd_{33}Se_{33}$ suggest that the hole transfer from the photoexcited QD to Ru(II)bpy complexes with neutral ligands is thermodynamically unfavorable, since the QD associated states are higher in energy than the states associated with the Ru(II)bpy dye, as schematically illustrated in Figure 26, right panel. In contrast, the occupied orbitals of the BD with the negatively charged ligands coordinated with the metal ion are comparable or slightly higher in energy than the QD's states at the edge of the VB. This energy alignment of the BD's orbitals provides favorable conditions for a photoexcited hole to transfer from the QD to the dye, as depicted in Figure 26, left panel.

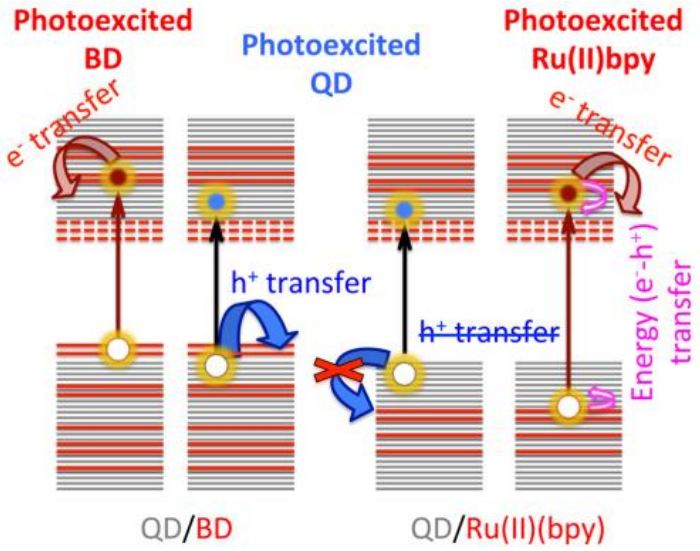

Figure 26. Schematic representation of the electronic structure of the QD/Ru(II)-dye composites illustrating the most probable charge transfer process. Left two panels describe processes in the CdSe QD functionalized by BD, when either the BD (first column) or the QD (second column) are excited. Right two panels describe processes in the CdSe QD functionalized by Ru(II)bpy, when either the QD (third column) or the Ru(II)bpy (fourth column) are excited. The states associated with the dye are red, and QD's states are gray. The lowest unoccupied states of the dyes are marked by dashed lines to depict their optically dark character originating from their metal-to-ligand charge transfer (MLCT) nature. The hole transfer from the QD to the dye is energetically favorable in QD/BD composites, while it is absolutely unfavorable in QD/Ru(II)bpy structures.

Electron transfer from the photoexcited QD is also possible, since the dye's unoccupied orbitals are located below the QD's levels. Thus, both the electron and the hole transfer are thermodynamically favorable in QD/BD composites. Inaddition, the energy transfer process is also energetically possible in composites of small QDs. It was experimentally found that the energy transfer from the CdSe QD to the Ru(II)bpy dye dominates the charge transfer in QDs with diameters smaller than 4 nm [42]. In larger QDs, the energy of the CB edge decreases so that the unoccupied dye orbitals become higher in energy than the edge of the QD's CB, where the electron excitation occurs. Therefore, the electron transfer to the dye is less favorable in photoexcited QDs of diameter larger than 2 nm. When the dye is excited, the electron transfer from the dye to the QD is expected to dominate in QDs functionalized by the BD and its derivatives with negatively charged ligands. In composites of QDs functionalized by Ru(II)pby complexes with neutral ligands, however, the electron transfer has a higher chance to compete with the energy transfer, when both electron and hole are transferred from the complex to the QD, since the hole transfer is also energetically favorable in this case, as illustrated in Figure 26.

Similar scenarios for charge transfer have been experimentally detected in various functionalized QDs. For instance, experimental studies of CdSe QDs functionalized by rhodamine B (RhB) dyes have determined the predominant quenching pathway of exciton dissociation to be electron transfer from the RhB to the QD, while the energy transfer process from the complex to the QD accounted for 16% [68]. In CdSe QDs functionalized by Ru(II)bpy complexes, the hole transfer efficiency is still under debate, while the energy transfer from the complex to the QD has been clearly observed for QDs with diameter smaller than 4 nm [68]. An efficient hole transfer from the CdSe QD to the Ru(II) dye with the cyanide ligands (Ru505) has been detected by time-resolved PL spectroscopy and photocurrent measurements, independent of the presence of the

TiO2 substrate, while the energy transfer dominates in photoexcited QDs functionalized by the N3 dye with two thiocyanate ligands [45, 46]. In CdS nanorods functionalized by $[Ru(II)bpy(tpy)Cl]^+$, the hole transfer from the photoexcited nanorods to the dye has been detected at the 0.1−1 ns time scale, while the electron transfer back to the CdS takes a much longer time (10−100 ns) [204].

If compared to the electron transfer from the anthocyanin sensitized TiO_2 nanocrystalline films, where the electron injection from the dye to the semiconductor surface happens faster than 100 fs [205], the observed times of the charge transfer in nonorode/dye composites [204] are much slower. Such relatively long times of charge transfer might be a signature of a weak Dexter type coupling between the donor and acceptor. As shown in Figure 21, our calculations demonstrate weak hybridization between the QD's and the dye's orbitals, despite a strong confinement of the QD, which is expected to force the QD's wave function to "leak" outside the QD surface. Due to the localized character of the dye and the QD orbitals, they do not strongly overlap, which should result in weak electronic couplings between subsystems leading to slower charge transfer. On the other hand, our simulations demonstrate the "leakage" of the QD's orbitals to small capping molecules, such as $OPMe_3$ or NH_2Me, resulting in a lot of QD−ligand hybridized states deep inside the VB and the CB of the QD [141]. As such, we conclude that it is the nature of the Ru(II) complexes that prevents strong hybridization with the QD states, despite significant QD−dye interactions and the QD confinement. Overall, our calculations point to the weak Dexter-coupling regime for QD/dye composites.

We would like to note, however, that our calculations only allow for estimations of thermodynamic conditions affecting the charge transfer, while kinetics and dynamics of charge transfer are left beyond our modeling. Indeed, many important characteristics, such as electronic donor−acceptor couplings, electron−phonon couplings, Auger couplings, and electron−hole

couplings have to be directly calculated to provide a full description of the charge transfer in samples of QD/dye composites. To include these properties, nonadiabatic dynamics simulations [64, 155] have to be performed to get all details on the charge and energy transfer, which is the scope of our future work. Nonetheless, the presented data on thermodynamic conditions allow us to roughly estimate the feasibility of charge transfer processes and their dependence on the type of the dye interacting with the QD surface. Thus, our calculations elucidate the effect of the dye structure on the minimal requirements to the Ru(II) complex molecules that either favor or disfavor the charge transfer in QD/dye composites.

5.1.4. Excited state properties of QD/dye composites

The accuracy of charge/energy transfer measurements depends on the overlaps of optical transitions of each species in the hybrid QD/dye composites. The small overlap between optical transitions of the QD and the dye ensures better resolution and control in experiments. However, these overlaps are not only defined by the optical properties of individual molecules in the composite, but also by the QD−dye interactions. To explore the effect of the QD−dye interactions on the optical transitions of QD/dye composites, Figure 27 compares the absorption spectra of $Cd_{33}Se_{33}$ functionalized by the Ru(II)bpy complexes 1a and the black dye BD-t and BD-c with the respective spectra of the isolated pristine $Cd_{33}Se_{33}$ and dyes. This comparison clearly indicates the additive character of absorption spectra of composites: The main spectral features of the isolated systems coincide well with those of the functionalized QDs. The absolute values of the oscillator strengths of transitions contributing to each spectral peak for both isolated and interacting QD/1a systems are depicted in Figure 28, directly evidencing the additive nature of the absorption spectra. Similar additive spectral character has been experimentally found in CdSe/ Ru(II)bpy composites [42]. Such additive character is a signature of weak hybridization between the dye's and QD's orbitals

contributing to optical transitions, explaining the weakly perturbed behavior of absorption spectra of QD/dye composites versus the isolated systems.

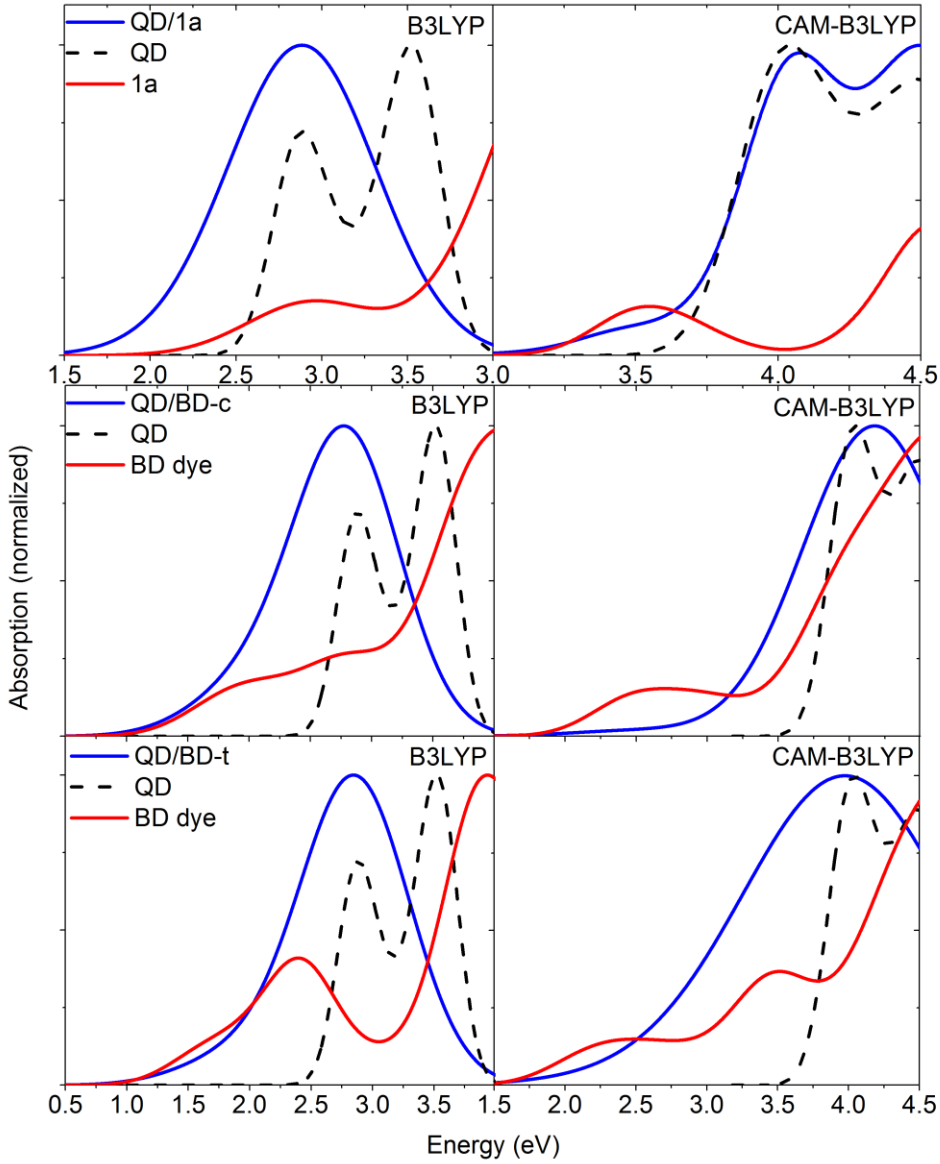

Figure 27. Calculated absorption spectra of the $Cd_{33}Se_{33}$ QD functionalized by Ru(II)−bipyridine complexes 1a (top panels) and the black dye with different anchoring configurations (middle and bottom panels) in benzonitrile. For references, the absorption spectra of the bare $Cd_{33}Se_{33}$ QD (dashed black line) and the isolated Ru(II) complex (red line) are also plotted. Isolated systems are calculated with the preserved geometry they have in the hybrid QD/dye composite. Left and right panels compare the spectra calculated by hybrid B3LYP and by the long-range corrected CAM-B3LYP functionals. For all systems, the lowest-energy weakly intensive band are associated with the Ru(II) complex, which is very distinct from the next highly intensive band dominated by the QD transitions.

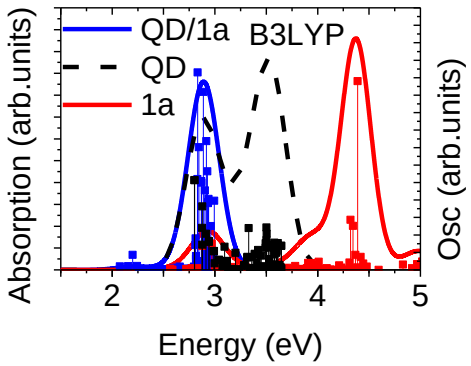

Figure 28. Calculated absorption spectra of the $Cd_{33}Se_{33}$ QD functionalized by Ru(II)- bipyridine complexe 1a in benzonitrile. For references, the absorption spectra of the bare $Cd_{33}Se_{33}$ QD (dashed black line) and the isolated 1a complex (red line) are also plotted. Isolated systems are calculated with the preserved geometry they have in the hybrid QD/dye composite. The hight of vertical lines corresponds to the oscillator strength of electronic transitions contributing to each absorption peak. All calculations are performed using linear response TD-DFT within B3LYP functional and mixed basis set LANL2DZ (Cd, Se, Ru)/6-31G*(C, H, O).

Figure 27 also compares the absorption spectra obtained by B3LYP and CAM-B3LYP functionals in order to check the effect of the used methodology on description of optical properties of the QD/dye composites. Overall, except the blue shift by about 1 eV in CAM-B3LYP calculations, both functionals provide qualitatively similar optical spectra of the systems, with a slightly blue-shifted dye component in QD/1a composite when calculated by B3LYP. In the considered QD/dye composites, the lowest-energy weak spectral peak belongs to the metal-to-ligand charge transfer (MLCT) transitions of the dye. Such low intensity, lower-energy states with MLCT character are typical for Ru(II) complexes [42]. In addition, there are a few low energy transitions in QD/dye composites that are optically dark, since they originate from the optically forbidden QD-to-complex transitions. The presence of these dark states in small CdSe QDs functionalized by dyes might significantly decrease the PL of composites. The lowest energy dye-associated peaks are spectrally separated from the next highly intense band, mostly originating from optically active QD-to-QD transitions. This spectral separation should provide a good experimental resolution of the excitation of the Ru(II) complex. The BD has a smaller optical gap

and wider absorption band compared to the Ru(II)bpy complexes [2]. All complexes demonstrate some overlaps between the higher energy dye and QD peaks in the absorption spectra of the QD/BD composites. Nonetheless, the second high-intensity band (at about 2.8 eV) in all composites we considered have predominantly QD character with just a small overlap with the dye's transitions. However, such overlaps between optical transitions originating from the dye and the QD are expected to increase in composites of larger size QDs, due to redshifts of the QD optical gaps [81]. Similar overlaps were experimentally found in QD/N3 composites [45], which have a similar chemical structure to the BD. In this case, photoexcitation to the QD's absorption maxima cannot be uniquely assigned either to the QD or to the complex, and determination of the charge transfer process is very challenging in experimental probes.

5.2. Summary

To summarize, our DFT and TDDFT calculations demonstrate that variations in the solvent polarity and dye's ligands, specifically in their charge, can be tuned to adjust the electronic structure of QD/dye composites and, subsequently, to facilitate desirable conditions for charge transfer direction and efficiency. For instance, in considered molecular structures, functionalization of CdSe QDs by different Ru(II)bpy complexes with neutral ligands results in energetically unfavorable conditions for hole transfer from the photoexcited QD to the dye, since the occupied orbitals originating from thedye are located deeper inside the VB of the QD. In contrast, a substitution of bipyridines to thiocyanate ligands or Cl ions having negative charge, like in the black dye and its derivatives, destabilizes Ru(II)-associated orbitals, shifting them toward the very edge of the QD's VB. Such alignment of optically sensitive electronic levels allows for the energetically favorable conditions for the hole transfer from the QD to the black dye.

However, independent of the dye, its attachment, the QD size, and the presence of other small passivating ligands, the unoccupied orbitals of the dye appear close to the edge of the QD's conduction band. These states are linked to optically allowed MLCT transitions in the lowest energy absorption bands of the QD/dye composites, and provide pathways for electron transfer from the excited dye to the QD. In composites of CdSe QDs functionalized by Ru(II)bpy with neutral ligands coordinated to the metal ion, however, the electron transfer has a higher chance to compete with the energy transfer than in the QD/BD, since the hole transfer from the dye to the QD is also energetically favorable in this case. For larger QDs functionalized by Ru(II) complexes, our calculations predict the overlap between optically allowed dye-to-dye and QD-to-QD transitions in the absorption spectra of QD/BD composites, which make experimental control over the charge transfer direction very challenging. We also found that the mutual alignment of the dye's and the QD's orbitals is very sensitive to the solvent polarity. The dye's orbitals shift toward the lower energies with an increase of the solvent polarity in QDs functionalized by the dyes with negatively charged ligands, while the trends are reversed in composites of QDs functionalized by dyes with neutral ligands. These trends are attributed to the difference in the sign of the effective charge on the complex. As such, using less polar solvents for QD/BD composites is predicted to be more favorable for the energy level alignment to facilitate the hole transfer from the photoexcited QD to the black dye with negatively charged ligands. In contrast, more polar solvents are expected to provide more favorable conditions for the electron transfer from the photoexcited dye to the QD in composites of CdSe QDs functionalized by Ru(II)bpy dyes with neutral ligands. Finally, the QD-dye interactions are found to dominate in stabilization of the dye's orbitals with respect to the QD's VB edge, as compared to the QD's and dye's HOMO offsets in the isolated QDs and Ru(II) complexes. Our simulations pinpoint the origin of the effect only qualitatively

given a limited number of considered structures. In fact, observed electronic level stabilization can be used in future studies to further tune the composite energetics by varying density of dye coverage, arranging preferential binding of dyes to specific QD crystal surfaces, modifying the electronegativity of surface ligands, etc. Overall, our calculations can be useful for guiding rational design of metal−organic dyes to achieve efficient directional charge transfer processes, important for photovoltaics and photocatalysis.

CHAPTER 6. EFFECT OF BINDING GEOMETRY ON ENERGETIC ALIGNMENT AND ELECTRONIC COUPLING

In this chapter, we use density functional theory (DFT) and time-dependent DFT to simulate $Cd_{33}Se_{33}$ QDs functionalized by Ruthenium polypyridyl dye (N719). The primary goal is to investigate the effect of binding geometry of dye on energetic alignment and the electronic coupling.

To study the effect of binding geometry on interfacial energetic alignment, the geometry of $Cd_{33}Se_{33}$ QD/N719 dye nanocomposite is optimized at the level of density functional theory (DFT). As indicated earlier, a combination of B3LYP functional with LANL2DZ/6-31g* mixed basis set (LANL2DZ: heavy metals; 6-31g*: light elements) correctly predicts the energetic alignment that favors hole transfer from CdSe QD to black dye, which is in consistent with experimental observation [28, 57]. Moreover, it is found, the qualitative trend of band gap, optical gap, binding energy, etc, predicted at the level of DFT with such functional and basis set is reliable with respect to the size and chemical composition of QDs as well as functionalizing QDs with different dye [23, 80, 81, 141]. Therefore, we continue to use such combination of functional with basis set to model $Cd_{33}Se_{33}$ QD/N719 dye nanocomposite.

6.1. Results and Discussion

6.1.1. Binding geometries

N719 dye is attached to $Cd_{33}Se_{33}$ QD by choosing different deprotonation scheme of anchoring group shown in Figure 29. There are a total of four groups of binding configurations. Figure 30 shows three-dimensional views of these structures.

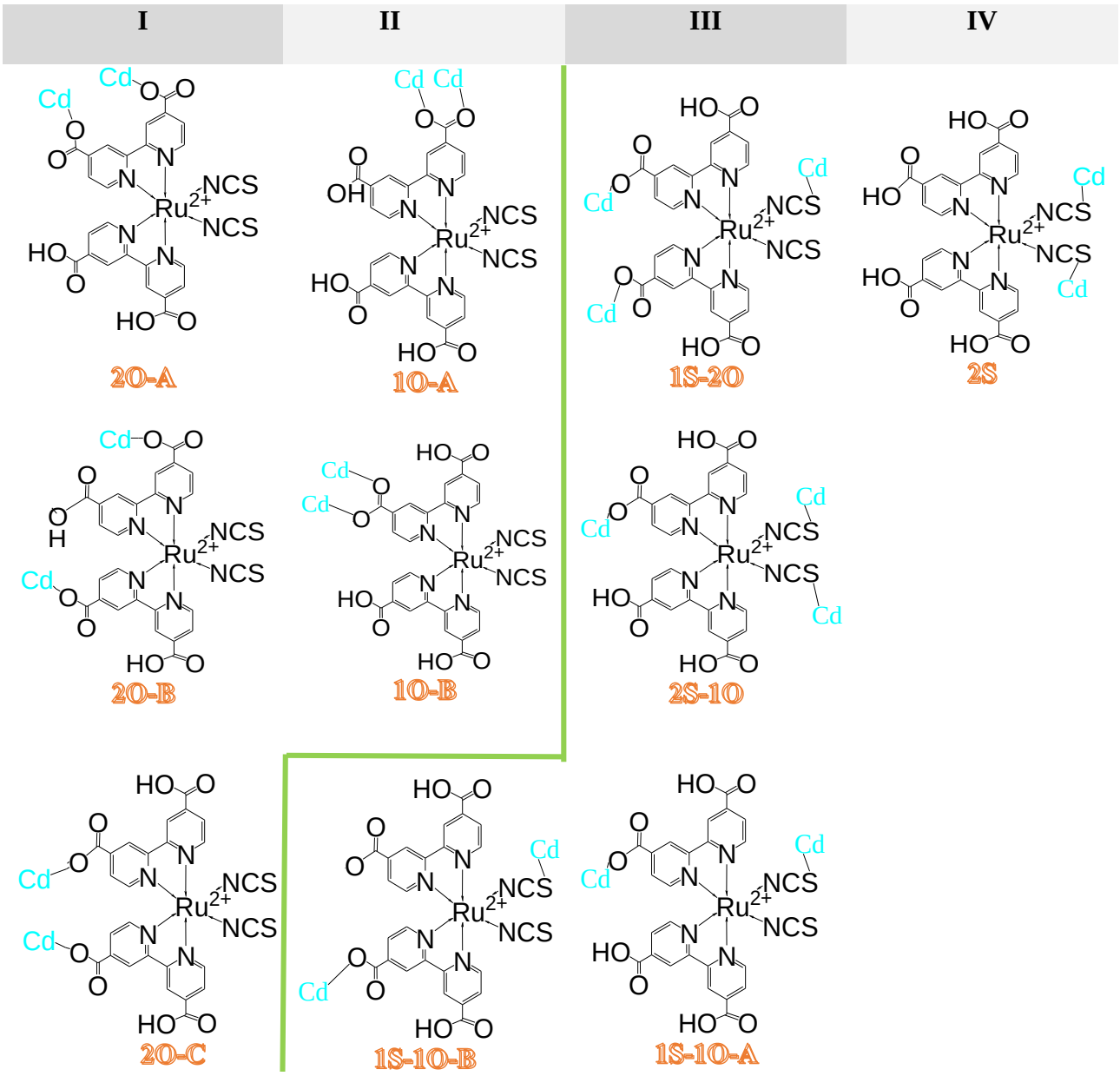

Figure 29. N719 dye is attached to the Cd atoms of $Cd_{33}Se_{33}$ QD. Both carboxylate (denoted by "O") and isocyanate groups (denoted by "S") are used for anchoring N719 dye to $Cd_{33}Se_{33}$ QD. There are four groups of attachments depending on the anchoring group: I. double-carboxylate; II. single-carboxylate; III. carboxylate/isocyanate mixture; IV. double-isocyanate. Each group contains different binding configuration of dye to QD depending on the deprotonation site, denoted by A, B, C.

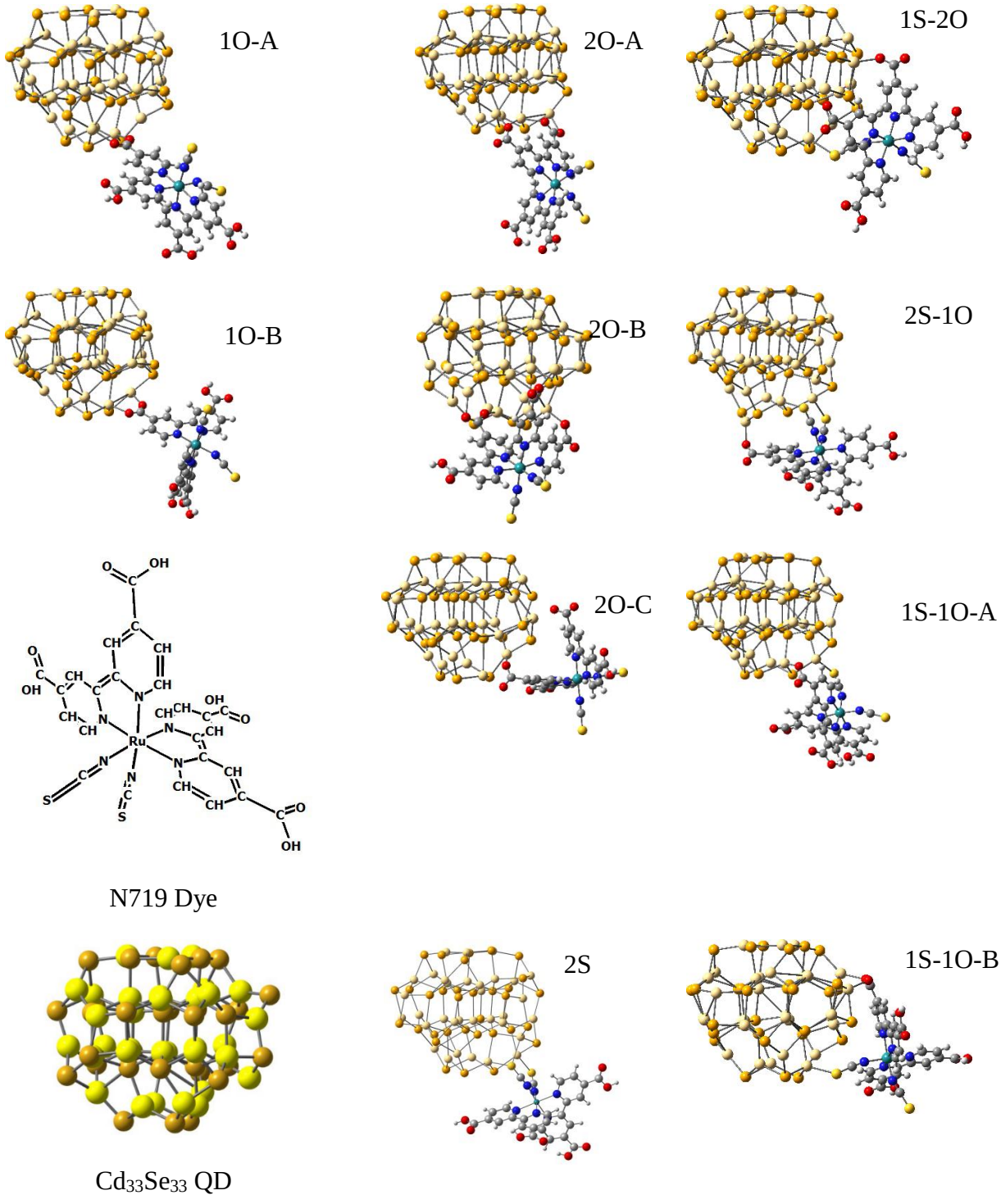

Figure 30. Three-dimensional views of binding geometries of N719 dye attached to $Cd_{33}Se_{33}$ QD.

In group I two carboxylic acids are deprotonated to give 2O-A, 2O-B, 2O-C binding configurations; in group II there are two binding configurations depending on the position of

carboxylate anchor (i.e. 1O-A, 1O-B); in group III there are four configurations (i.e. 1S-2O, 2S-1O, 1S-1O-A, 1S-1O-B) depending on the relative position of isocyanate anchor with respect to carboxylate anchor; only one configuration is available for double isocyanate anchors in group IV (i.e. 2S). It should be noted, the deprotonation sites in group III are chosen in two different 2, 2´-bipyridine ligands, as we found that deprotonating the same ligand destabilizes the isocyanate anchor, and detaching N719 dye from $Cd_{33}Se_{33}$ QD surface.

Table 8. Binding energy, band gap, Cd-S, Cd-O bond lengths of $Cd_{33}Se_{33}$ QD/N719 dye composites with different anchoring group as well as the surface orientation, in vacuum and CH_3CN, respectively

		Vacuum				CH_3CN		
		Binding energy (eV)	Band gap (eV)	Cd-S bond (A^o)	Cd-O bond (A^o)	Binding energy (eV)	Band gap (eV)	Cd-O bond (A^o)
	1O-A	3.25	1.67	-	2.28	0.60	2.13	2.32
I	1O-B	3.33	1.61	-	2.28	0.92	2.02	2.32
	2O-A	5.78	1.65	-	2.27	1.03	2.25	2.39
	2O-B	5.65	1.44	-	2.27	1.04	2.16	2.39
II	2O-C	5.39	1.48	-	2.28	0.82	2.32	2.42
	1S-2O	4.41	1.97	2.75	2.21	0.43	2.34	2.35
	2S-1O	3.14	1.15	2.89	2.17	0.48	2.09	2.29
	1S-1O-A	2.85	1.74	2.74	2.18	0.50	2.16	2.32
III	1S-1O-B	3.29	1.83	2.75	2.32	0.61	2.54	2.39
IV	2S	1.22	1.23	2.88	-	/	/	/

/ - N719 Dye is detached from $Cd_{33}Se_{33}$ QD surface in solvent.

Table 8 shows, the binding energies of group I are relatively larger than the other groups in vacuum, on the contrary, their band gaps are generally smaller except 2O-A. The largest band-gap energies appear to be the single-isocyanate anchoring geometry in group III (i.e. 1S-2O, 1S-1O-B); however, they decrease rapidly with one additional isocyanate anchor in cases of 2S-1O and 2S configurations. We noted that, the dye's states are protruded into the VB when increasing

the number of isocyanate anchors, consequently, the total band gap is determined by the relative positon of LUMO of dye with respect to the VB edge.

Increasing the number of isocyanate anchors also increases Cd-S bond length, ca. 2.88 Å for double-isocyanate anchor vs ca. 2.75 Å for single-isocyanate anchor. On the contrary, the Cd-O bond length shows a casual relation with the number of isocyanate anchors, for both longer bond distances (i.e. 2.21 Å and 2.32 Å) and shorter bond distances (i.e. 2.17 Å and 2.18 Å) are co-existed in cases of single-isocyanate anchor and double-isocyanate anchor. Adding solvent increases the band gap due to the stabilization of dipole moments at QD's surface, and decreases the binding energy. For example, for some binding configurations in group III and IV, N719 dye is detached from $Cd_{33}Se_{33}$ QD's surface in strongly polarized CH_3CN solvent, suggesting the coulomb repulsion between solvent molecules and dye decreased binding energy. In addition, the Cd-O bond lengths are slightly increased in solvent.

6.1.2. Energetic alignments of QD/dye composites

PDOS of QD/dye composite with single- and double-carboxylate anchors (Figure 30 (a) and (b)) show, the energy level of highest occupied state in N719 dye is significantly higher than the VB edge indicating the negatively charged isocyanate ligands destabilized the MOs of dye, while the energy level of lowest unoccupied state is slightly lower than the CB edge except for 2O-B and 2O-C binding configurations. With the extra isocyanate anchor (Figure 30 (c) and (d)) the highest occupied state of dye moves backward towards the VB edge, while the lowest unoccupied state of dye moves further away from the CB edge. In addition, the electron densities of $Cd_{33}Se_{33}$ QDs in group III and IV are more delocalized at the surface than group I and II. However, it should be noted, the PDOS (I, II, III and IV) are calculated upon the ground state geometry, while the real charge transfer occurs between the charge localized states at the adiabatic

crossing region. Therefore, we perform single point calculations on each diabatic state after charge-constrained optimizations at different binding geometries. We assume the final state for electron transfer is the initial state for electron & hole recombination, therefore both electron transfer and electron & hole recombination occur upon the same geometry Table 8 and 10 show the highest occupied MOs and lowest unoccupied MOs at ground state and charge-constrained state, respectively.

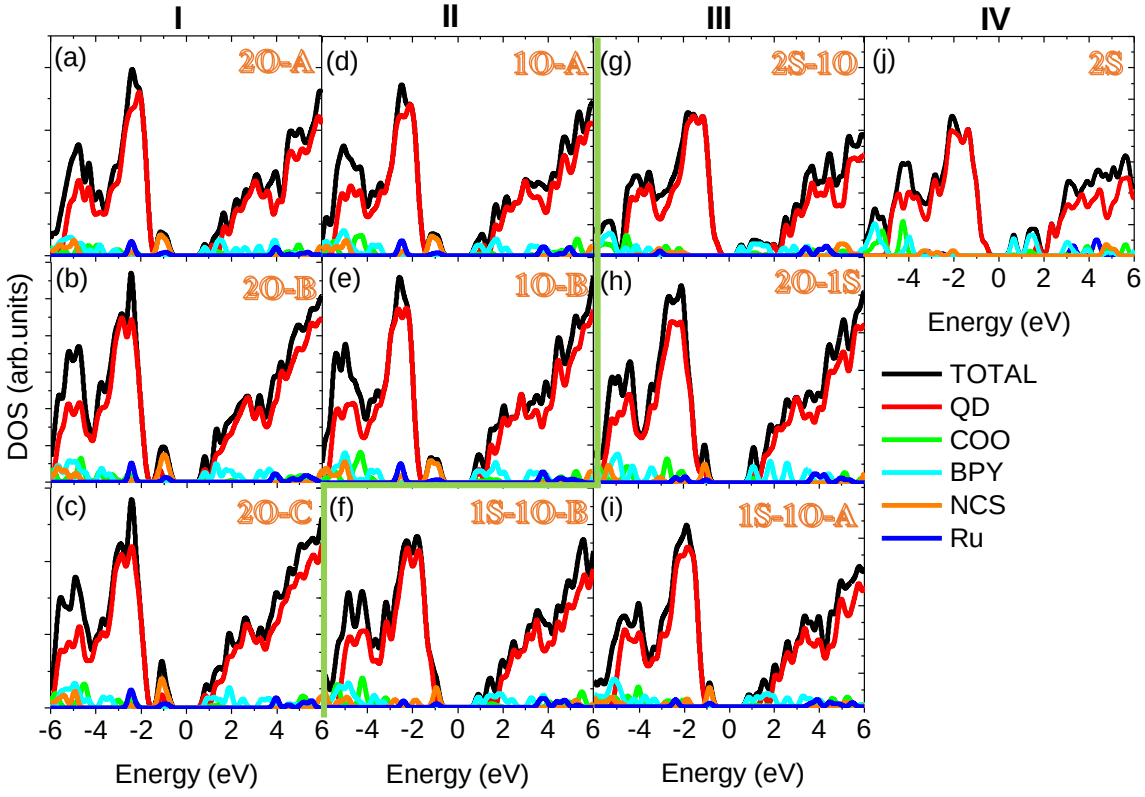

Figure 30. Projected density of states (PDOS) of $Cd_{33}Se_{33}$ QD functionalized by N719 dye with different binding geometry in vacuum. The highest occupied molecular orbital (HOMO) in group I, group II and group III (2S-1O, 2O-1S) are dictated by isocyanate group of dye, while it is dictated by QD for the other attachments. QD's states and dye's states are mixed near the VB edge for 2O-B and 2O-C binding geometries.

Table 9. Frontier Molecular orbitals (FMOs) of ground state at the occupied and unoccupied energy levels of $Cd_{33}Se_{33}$ QD/N719 dye nanocrystal composite in vacuum.

MOs	I			II	
	2O-A	2O-B	2O-C	1O-A	1O-B
HOMO-5	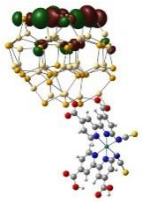	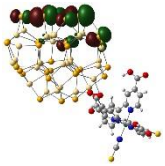	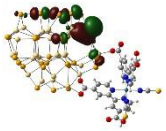	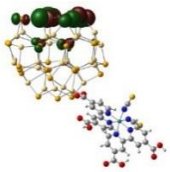	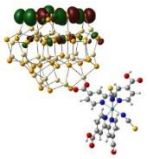
HOMO-4	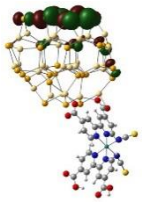	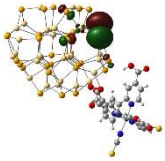	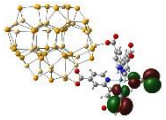	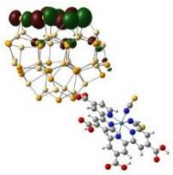	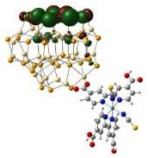
HOMO-3	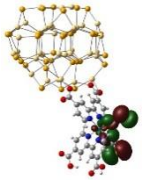	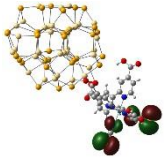	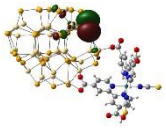	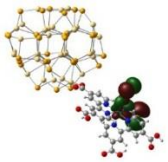	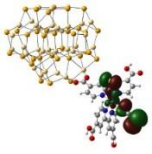
HOMO-2	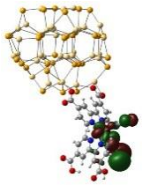	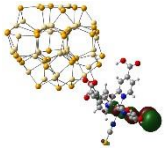	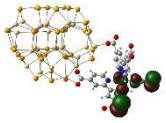	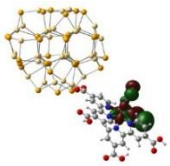	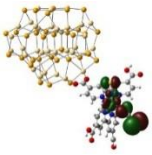
HOMO-1	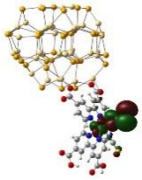	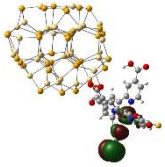	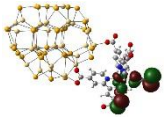	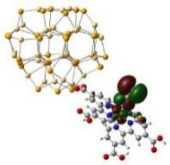	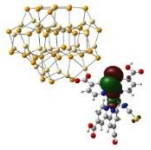
HOMO	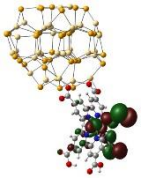	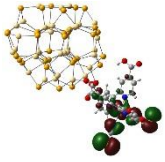	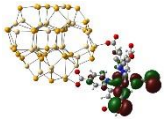	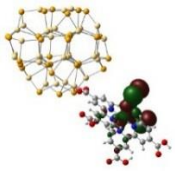	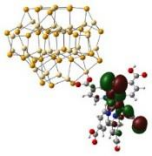

Table 9. Frontier Molecular orbitals (FMOs) of ground state at the occupied and unoccupied energy levels of $Cd_{33}Se_{33}$ QD/N719 dye nanocrystal composite in vacuum (continued).

LUMO	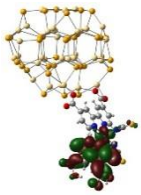	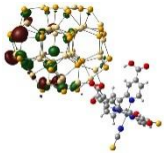	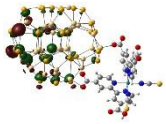	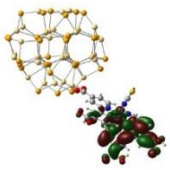	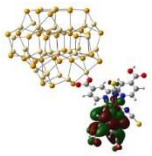
LUMO+1	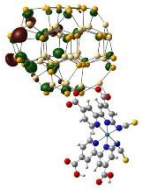	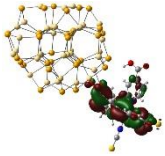	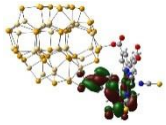	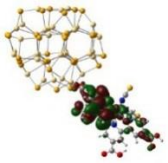	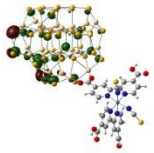
LUMO+2		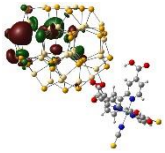	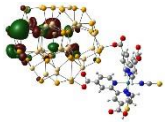	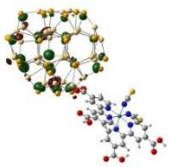	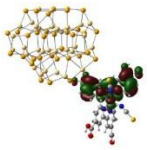
LUMO+3	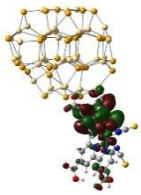	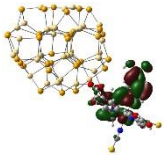	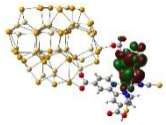	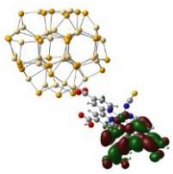	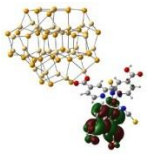
LUMO+4	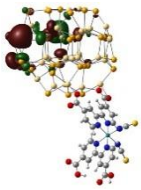	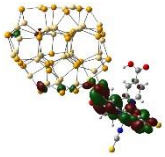	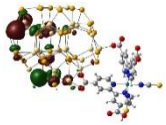	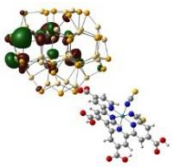	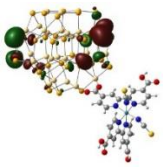
LUMO+5	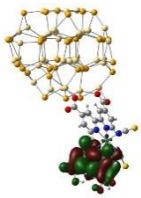	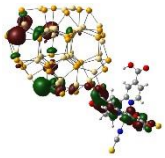	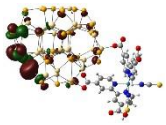	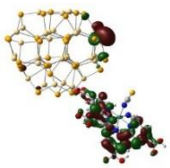	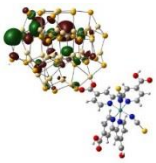

Table 9. Frontier Molecular orbitals (FMOs) of ground state at the occupied and unoccupied energy levels of $Cd_{33}Se_{33}$ QD/N719 dye nanocrystal composite in vacuum (continued).

	2S-1O	2O-1S	1S-1O-A	1S-1O-B	2S
HOMO-5	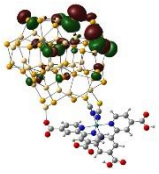	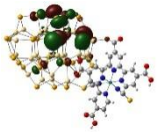	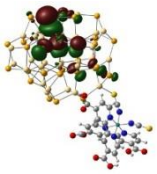	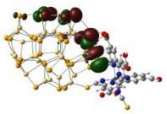	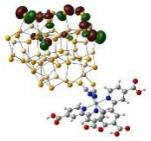
HOMO-4	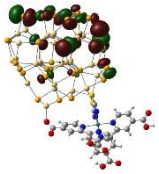	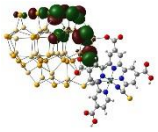	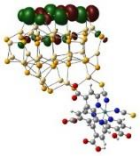	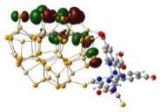	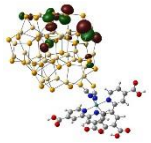
HOMO-3	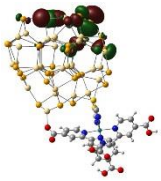	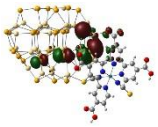	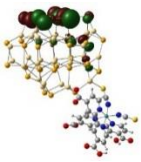	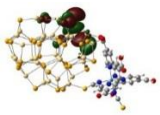	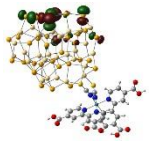
HOMO-2	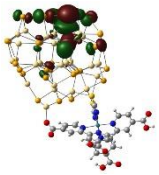	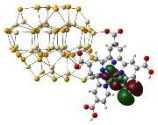		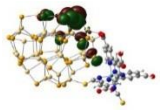	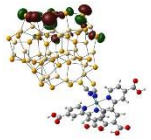
HOMO-1	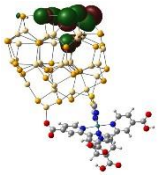	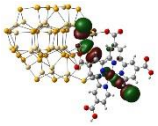	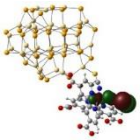	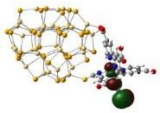	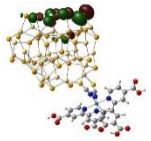
HOMO	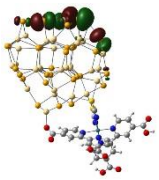	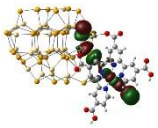	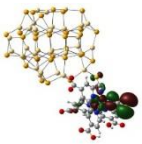	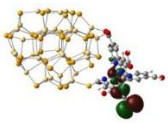	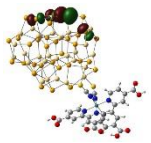

Table 9. Frontier Molecular orbitals (FMOs) of ground state at the occupied and unoccupied energy levels of $Cd_{33}Se_{33}$ QD/N719 dye nanocrystal composite in vacuum (continued).

LUMO	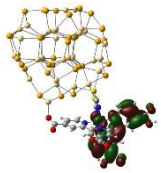	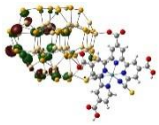	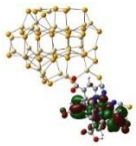	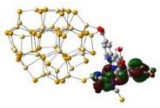	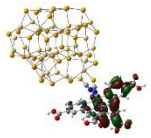
LUMO+1	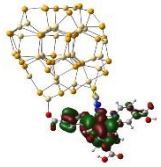	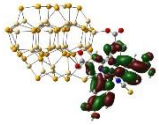		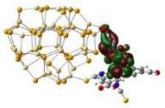	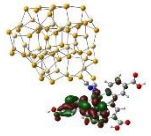
LUMO+2	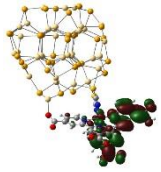	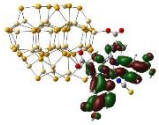	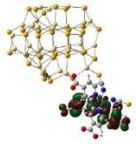	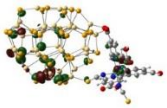	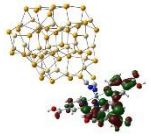
LUMO+3	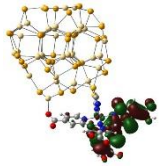		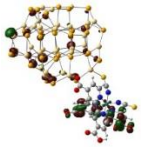	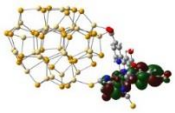	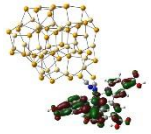
LUMO+4	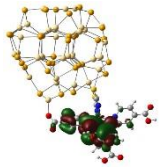	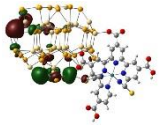	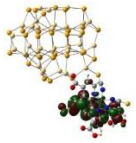	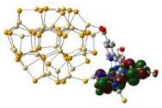	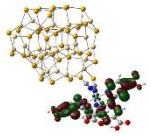
LUMO+5	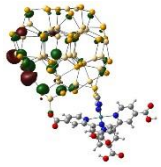	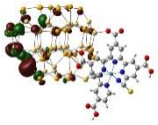	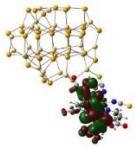	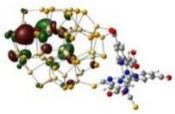	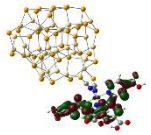

Table 10. Frontier Molecular orbitals (FMOs) of charge constrained state (*et* or *rt*) at the occupied and unoccupied energy levels of $Cd_{33}Se_{33}$ QD/N719 dye nanocrystal composite in vacuum

MOs	I			II	
	2O-A	2O-B	2O-C	1O-A	1O-B
HOMO-5	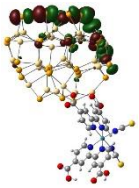	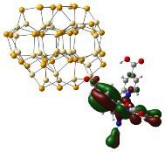	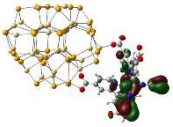	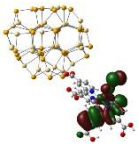	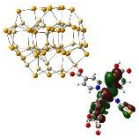
HOMO-4	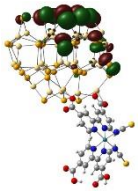	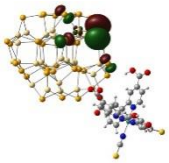	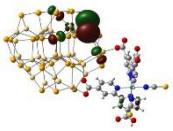	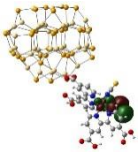	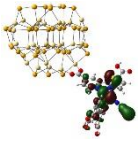
HOMO-3	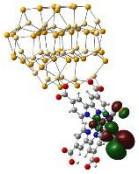	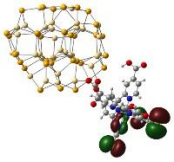	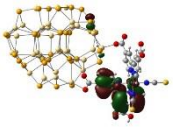	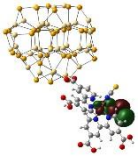	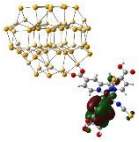
HOMO-2	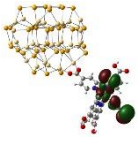	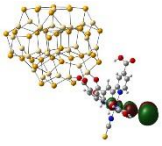	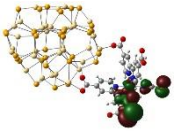	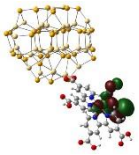	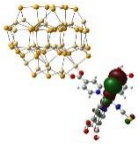
HOMO-1	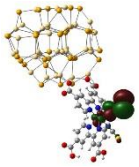	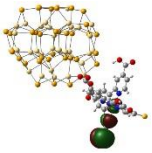	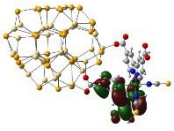	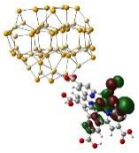	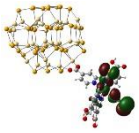
HOMO	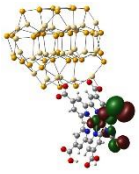	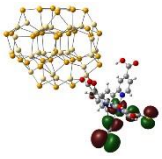	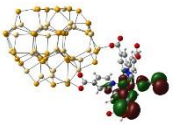	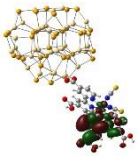	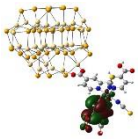

Table 10. Frontier Molecular orbitals (FMOs) of charge constrained state (*et* or *rt*) at the occupied and unoccupied energy levels of $Cd_{33}Se_{33}$ QD/N719 dye nanocrystal composite in vacuum (continued).

LUMO	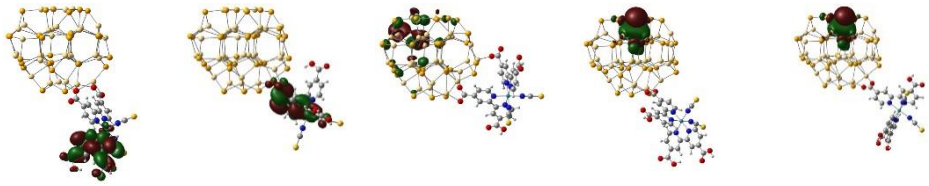				
LUMO+1	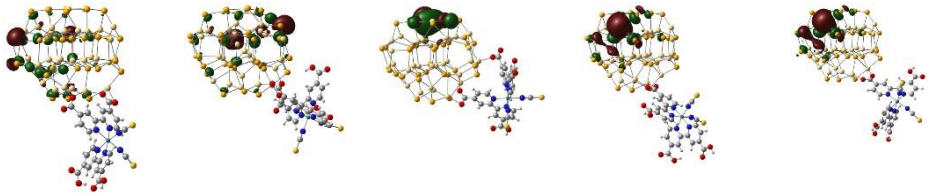				
LUMO+2	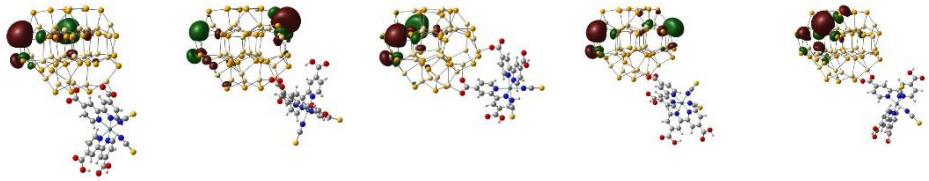				
LUMO+3	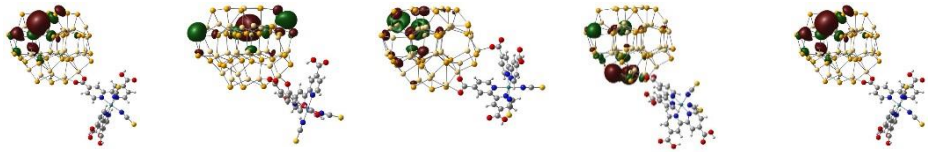				
LUMO+4	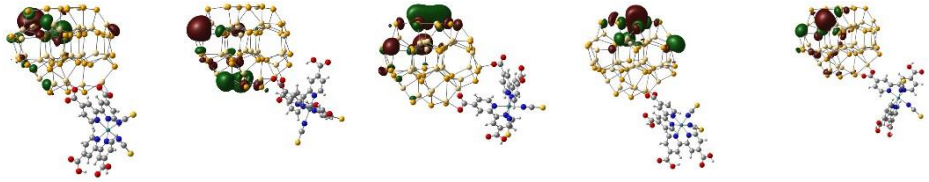				
LUMO+5	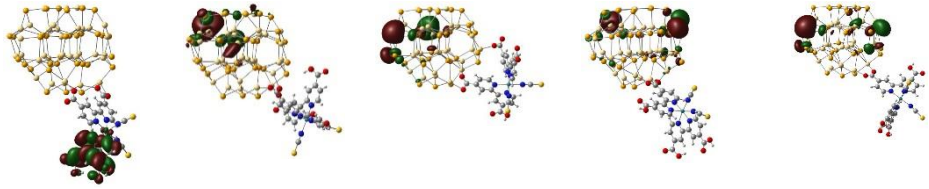				

Table 10. Frontier Molecular orbitals (FMOs) of charge constrained state (*et* or *rt*) at the occupied and unoccupied energy levels of $Cd_{33}Se_{33}$ QD/N719 dye nanocrystal composite in vacuum (continued).

	2S-1O	2O-1S	1S-1O-A	1S-1O-B	2S
HOMO-5	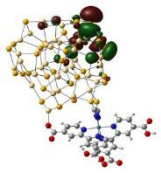	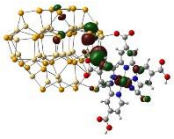	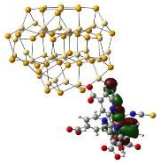	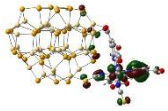	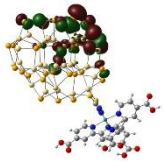
HOMO-4	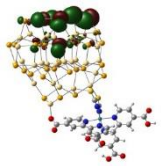	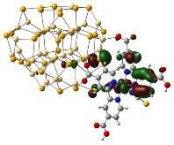	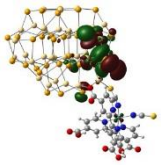	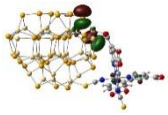	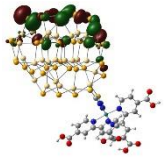
HOMO-3	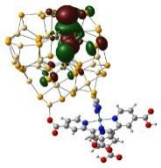	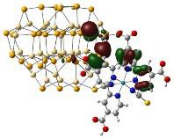	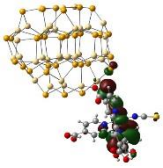	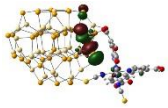	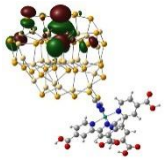
HOMO-2	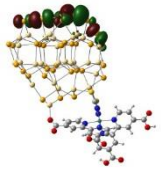	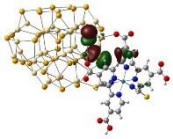	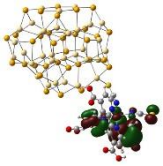	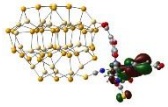	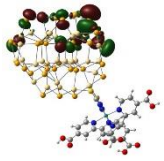
HOMO-1	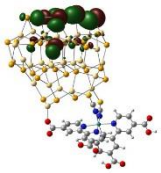	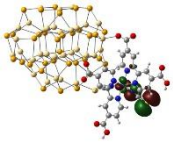	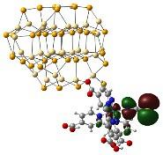		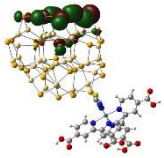
HOMO	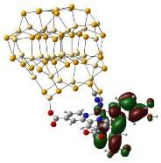	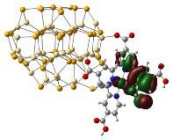	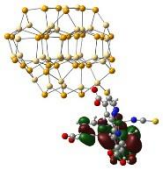	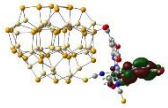	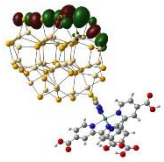
LUMO	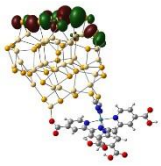	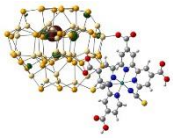	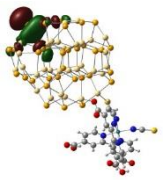	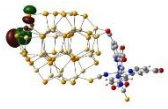	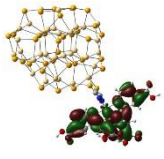

Table 10. Frontier Molecular orbitals (FMOs) of charge constrained state (*et* or *rt*) at the occupied and unoccupied energy levels of $Cd_{33}Se_{33}$ QD/N719 dye nanocrystal composite in vacuum (continued).

LUMO+1	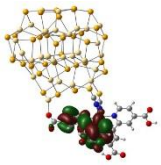	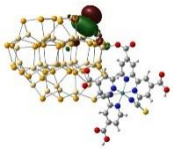	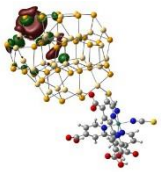	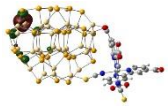	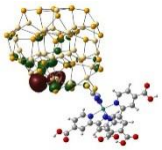
LUMO+2	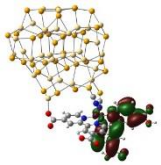	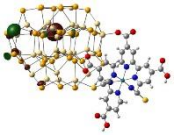	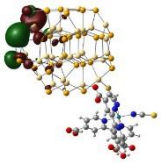	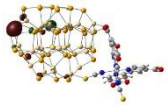	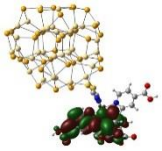
LUMO+3	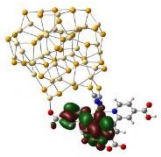	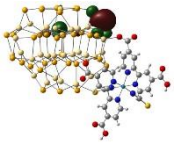	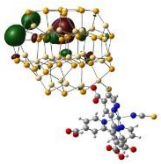	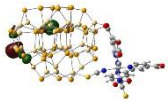	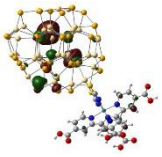
LUMO+4	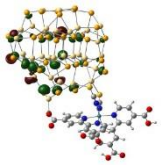	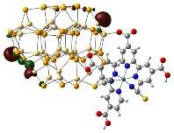	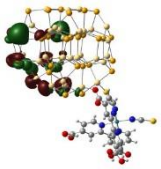	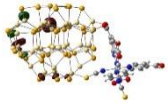	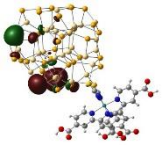
LUMO+5	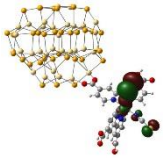	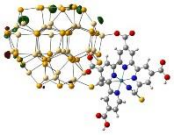	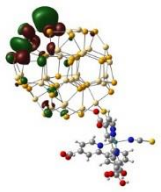	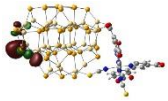	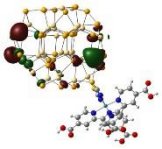

The characters of MOs in unoccupied energy levels are subject to significant changes from the ground states to charge constrained states. The most dominant feature is, the relative position between the lowest unoccupied energy levels of QD and dye is inversed at charge constrained state for most configurations except 2O-A, 2O-C, and 2S. Thus, for most binding geometries electrons are flew forwardly from dye to QD except the 2O-A, 2O-B, 2O-1S and 2S configurations, in which the electrons show back-transfer from QD to dye. Since most binding configurations

demonstrating electron forward-transfer, this indicates N719 dye is an exceptionally good co-sensitizer, especially for larger CdSe QD, as increasing the size of QD only brings down the CB edge providing more driving forces for the electron forward-transfer. In addition, we found for 2O-B and 2O-C binding configurations, the electronic coupling vector of 2O-C is one order of magnitude larger than 2O-B, whereas the donor-acceptor wavefunction overlapping of 2O-C is two order of magnitudes larger than 2O-B. Through inspecting the electron densities at ground states, it is found the electron densities in case of 2O-C are well localized in QD and dye, respectively, in contrast to a strong QD-dye mixture for 2O-B case (as illustrated by LUMO+5 electron density in Table 10). The mixing of electron densities between QD and dye reduces electronic coupling for 2O-B. As such, assuming the same nuclear reorganization energy along the reaction coordinates from ground state to charge constrained state, which can be inferred from the similar DOS in ground states (Figure 30) as well as charge distributions of frontier MOs in charge constrained states (Table 10) for two configurations, the electronic coupling of 2O-C remains larger than 2O-B. We further found, the main difference between 2O-B and 2O-C is the deprotonation site, in which for 2O-C the distance between two deprotonation sites are much smaller than 2O-B, indicating the increase of distance between deprotonation sites decreased electronic coupling.

Table 11. Frontier Molecular orbitals (FMOs) of ground state at the occupied and unoccupied energy levels of $Cd_{33}Se_{33}$ QD/N719 dye nanocrystal composite in CH_3Cl.

MOs	I			II	
	2O-A	2O-B	2O-C	1O-A	1O-B
HOMO-5			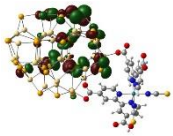	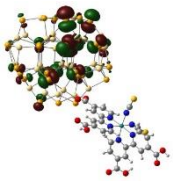	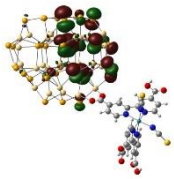
HOMO-4	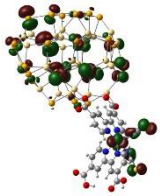	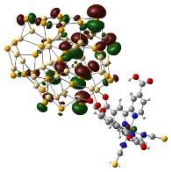	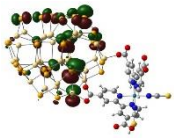	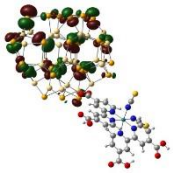	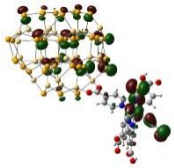
HOMO-3	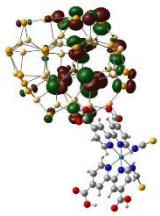	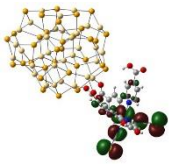	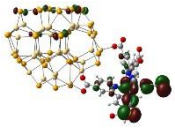	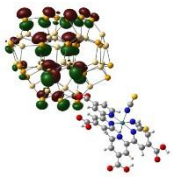	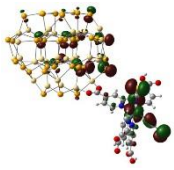
HOMO-2	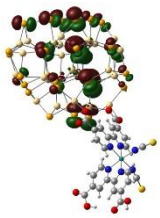	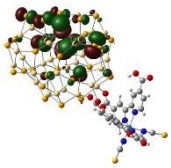	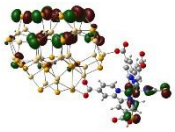	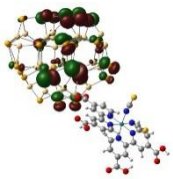	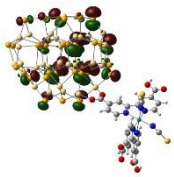
HOMO-1	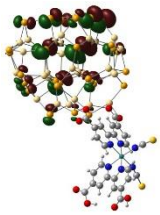	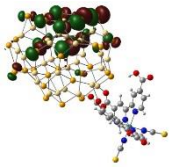	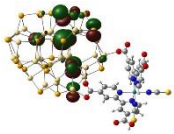	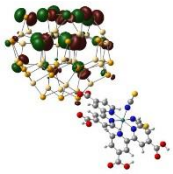	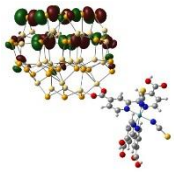
HOMO	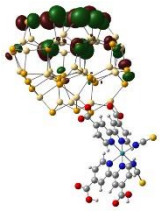	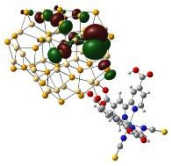	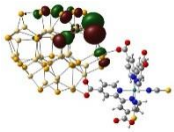	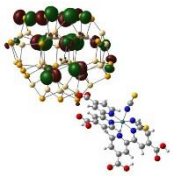	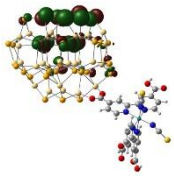

Table 11. Frontier Molecular orbitals (FMOs) of ground state at the occupied and unoccupied energy levels of $Cd_{33}Se_{33}$ QD/N719 dye nanocrystal composite in CH_3Cl (continued).

LUMO	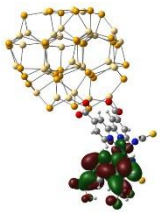	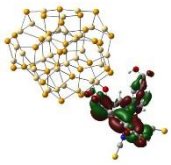	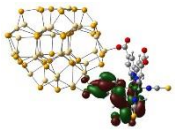	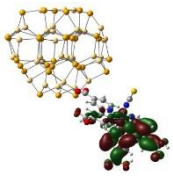	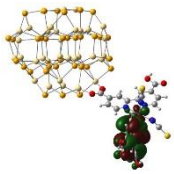
LUMO+1	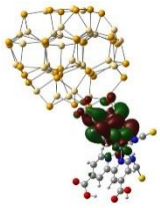	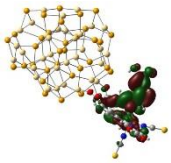	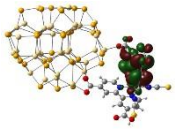	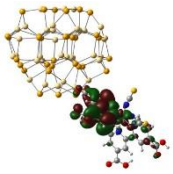	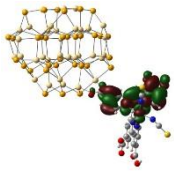
LUMO+2	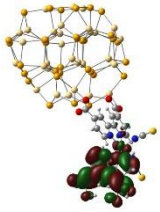	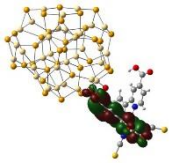	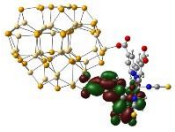	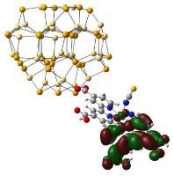	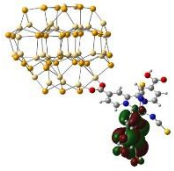
LUMO+3	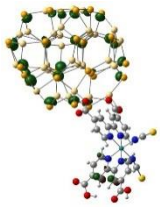	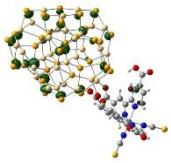	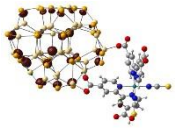	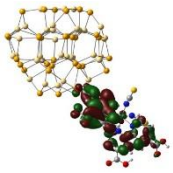	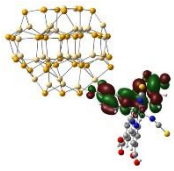
LUMO+4	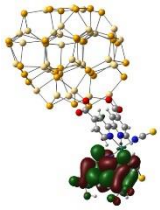	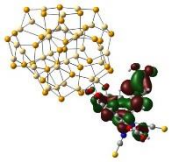	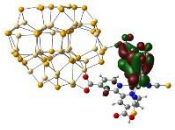	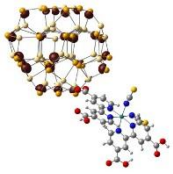	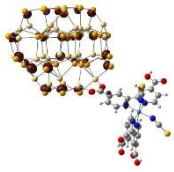
LUMO+5	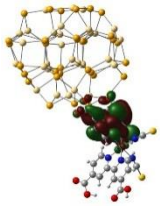	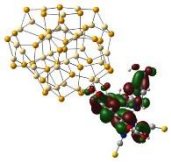	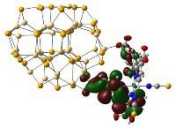	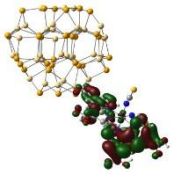	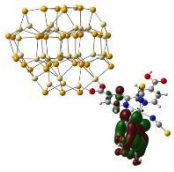

Table 11. Frontier Molecular orbitals (FMOs) of ground state at the occupied and unoccupied energy levels of $Cd_{33}Se_{33}$ QD/N719 dye nanocrystal composite in CH_3Cl (continued).

	2S-1O	2O-1S	1S-1O-A	1S-1O-B	2S
HOMO-5	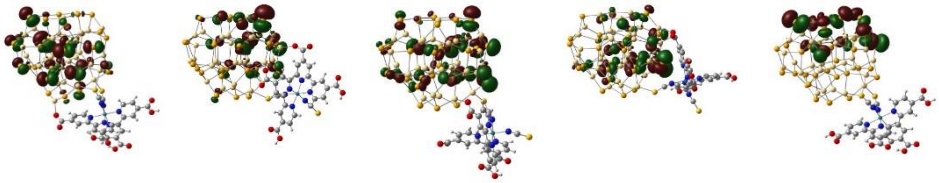				
HOMO-4	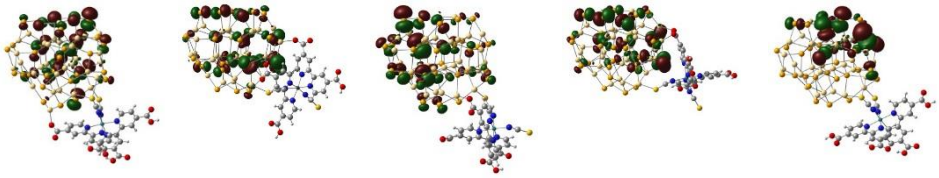				
HOMO-3	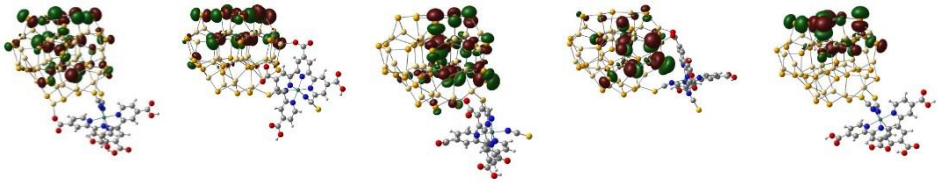				
HOMO-2	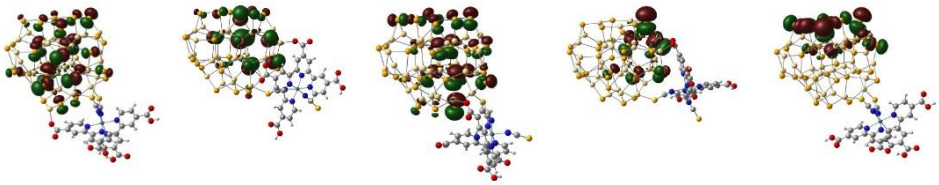				
HOMO-1	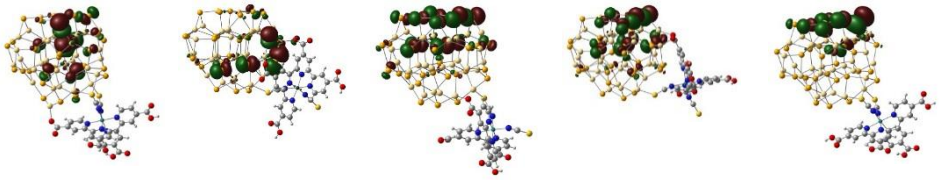				
HOMO	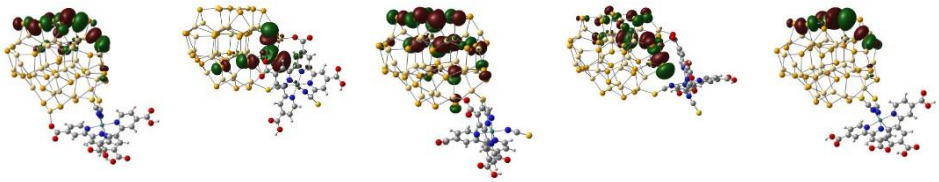				
LUMO	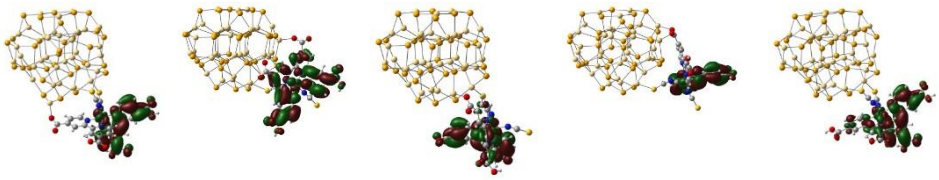				

Table 11. Frontier Molecular orbitals (FMOs) of ground state at the occupied and unoccupied energy levels of $Cd_{33}Se_{33}$ QD/N719 dye nanocrystal composite in CH_3Cl (continued).

LUMO+1	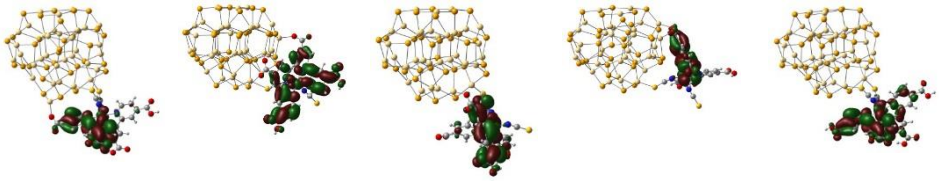				
LUMO+2	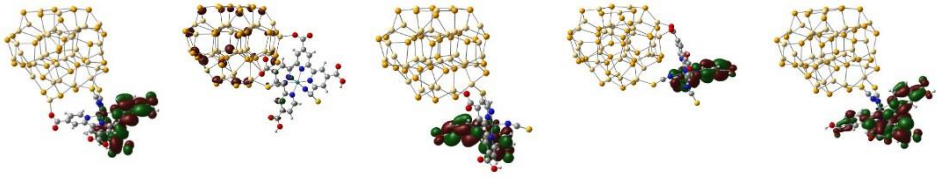				
LUMO+3	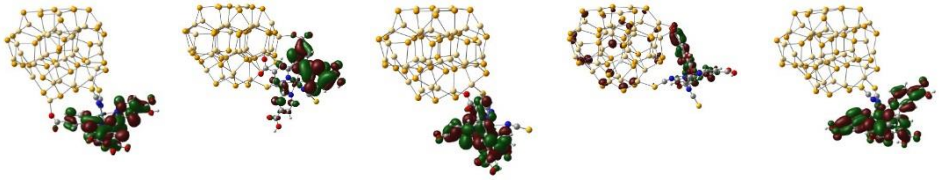				
LUMO+4	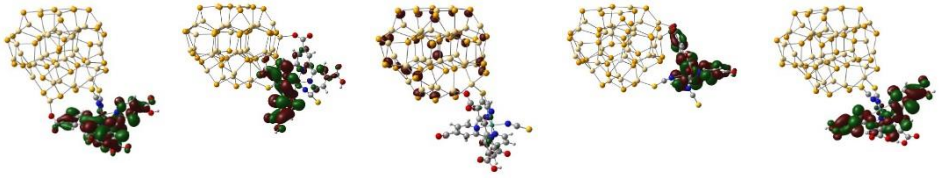				
LUMO+5	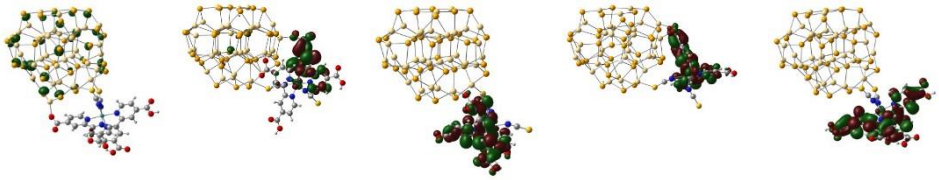				

We also noted, solvent increases the delocalization of molecular orbitals (MOs) at the surface of $Cd_{33}Se_{33}$ QD, as indicated in Table 11.

Table 12. Electronic coupling vectors (charge transfer integrals) for electron-transfer (*et*) as well as electron & hole recombination (*re*)

Binding geometry	Electronic coupling vector (eV)		Donor-acceptor wavefunction-overlapping	
	et	*re*	*et*	*re*
1O-A	3.84×10^{-8}	3.57×10^{-8}	4.54×10^{-10}	5.40×10^{-10}
1O-B	2.29×10^{-6}	4.2×10^{-9}	5.36×10^{-5}	1.57×10^{-10}
2O-A	-1.29×10^{-6}	2.32×10^{-7}	3.15×10^{-5}	7.35×10^{-6}
2O-B	-3.6×10^{-8}	1.84×10^{-8}	2.84×10^{-7}	4.13×10^{-7}
2O-C	8.28×10^{-7}	1.73×10^{-8}	2.33×10^{-5}	4.14×10^{-7}
1S-1O-A	8.08×10^{-8}	1.92×10^{-5}	3.46×10^{-4}	7.14×10^{-4}
1S-1O-B	3.41×10^{-4}	1.32×10^{-2}	1.32×10^{-2}	3.38×10^{-1}
2S-1O	4.60×10^{-4}	2.09×10^{-2}	4.68×10^{-1}	3.65×10^{-1}
2O-1S	3.22×10^{-6}	1.78×10^{-6}	5.35×10^{-5}	3.35×10^{-5}
2S	-7.30×10^{-2}	1.36×10^{-2}	4.49×10^{-1}	2.46×10^{-1}

- Negative sign indicates electron back-transfer from CB edge of QD to LUMO of dye.

Table 13. Ionization potentials of isolated N719 dyes. The structures are cut from $Cd_{33}Se_{33}$ QD/N719 dye composites, and optimized. The calculations are performed in vacuum with the same functional and basis set as in other calculations

		Ionization potential energy (eV)
I	2O-A/dye	13.143
	2O-B/dye	13.180
	2O-C/dye	13.181
II	1O-A/dye	10.575
	1O-B/dye	10.618
III	2S-1O/dye	11.682
	2O-1S/dye	14.034
	1S-1O-A/dye	11.714
	1S-1O-B/dye	11.757
IV	2S/dye	9.447

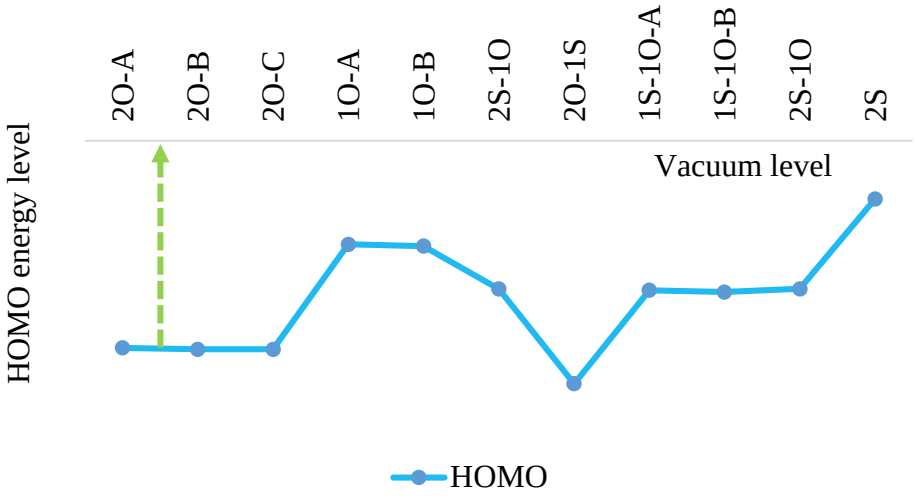

Figure 31. Relative energetic positions of HOMO levels of dye with respect to the vacuum level, which are derived based on the ionization potentials, according to Koopman theory. The geometries are cut from $Cd_{33}Se_{33}$ QD/N719 dye composites, then these dyes in different binding geometries are optimized to the lowest energetic configurations. The highest HOMO level appear to be the dye cut from 2S despite its HOMO in 2S deep inside the VB. On the other hand, even though the 2S-1O also has the dye states deep inside the VB; however the HOMO level of dye in 2S-1O is much lower than 2S. The calculations are carried out in vacuum with the same functional and basis set used in other calculations.

As mentioned above, increasing the number of isocyanate anchors pushes dye's metal states deep inside the VB edge, while the unoccupied ligand states are protruded out of the CB edge resulting an electron back-transfer in 2S and 2S-1O configurations (Figure 30). If comparing the ionization potentials of isolated dye cut from different binding geometries (Table 13), the dye cut from 2S has the smallest ionization potential, indicating a relatively closer of HOMO level to the vacuum level, thus a relatively higher energetic position with respect to the VB edge (Figure 31); however the dye state in 2S goes deep inside the VB edge, suggesting QD-dye interaction somehow changed the energetic alignment. Weiss Emily et al[65] suggest that a controllable exciton delocalization radius can be inferred from the bonding and antibonding molecular orbital hybridizations at the interface between CdSe QD and hole delocalizing ligands, depending on the

resonance of ligand's HOMO with respect to QD's frontier orbitals. Therefore, the potential barrier is determined by the region of density of states where the hybridization resonance occurs (Figure 32).

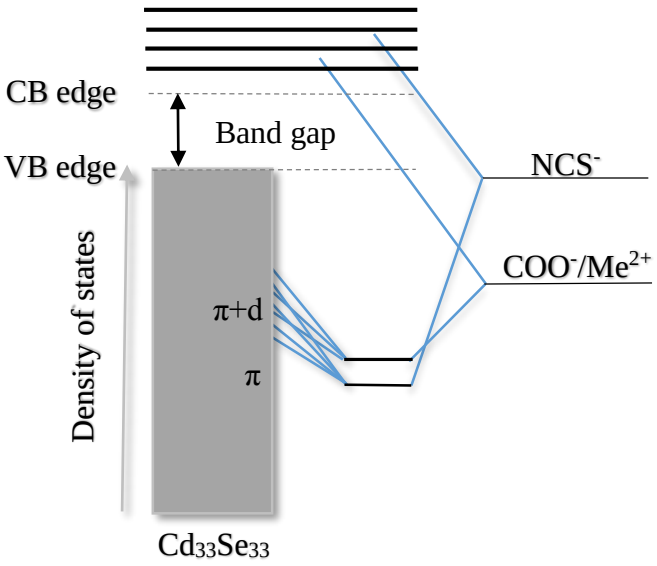

Figure 32. Schematics of molecular orbital hybridization at the interface between $Cd_{33}Se_{33}$ QD and isocyanate anchor as well as carboxylate anchor. Carboxylate anchor forms an effective mixture with metal state of dye, thus strongly resonates with the frontier d and π orbitals of $Cd_{33}Se_{33}$ QD. On the contrary, isocyanate anchor only forms resonate states with π orbitals of $Cd_{33}Se_{33}$ QD.

When attaching N719 dye to $Cd_{33}Se_{33}$ QD, bonding and antibonding molecular orbital hybridization also occurs at the interface due to the resonance of π orbitals in carboxylate group or isocyanate group with π orbitals of Se^{2-} ions near the VB edge. However, our calculation show that, the electronic states in carboxylate anchor are strongly hybridized with the metal ion state of dye, while isocyanate anchor has a negligible overlapping with metal ion state. This indicates, the mixed carboxylate/Me^{2+} state is easier to resonate with the d-orbital states of $Cd_{33}Se_{33}$ QD, since they possess the same symmetry, while the isocyanate states mainly resonate with the π orbitals of Se^{2-} ion. Consequently, carboxylate anchor has a stronger coupling with the frontier MOs of $Cd_{33}Se_{33}$ QD than isocyanate anchor due to more resonating states. This places the highest

occupied state of dye in 2S deep inside the VB edge after attached to $Cd_{33}Se_{33}$ QD. However, it is somehow contradictory to apply such hypothesis to 2S-1O, in which the highest occupied state of dye also rests deep inside the VB edge despite possessing one carboxylate anchor, implying additional factors to associate with the molecular orbital hybridization. By inspecting donor-acceptor wavefunction overlapping (Table 13), it is found, the amplitudes of donor-acceptor wavefunction overlapping for electron transfer and electron & hole recombination of 2S-1O are on the same scale (ca. 10^{-1}) as 2S, and much larger than other configurations. Such large amplitude increases the interfacial orbital interaction and the resonances between dye and QD. In addition, the frontier MOs at charge constrained state show more localized character on carboxylate groups that are not directly connected with QD, as such, the increase of donor-acceptor wavefunction overlapping has a negligible effect on carboxylate anchor, while mainly affecting the isocyanate anchor, which explains the very similar energetic position of dye in 2S and 2S-1O. Apparently, such binding configurations (2S and 2S-1O) do not benefit the $Cd_{33}Se_{33}$ QD as light sensitizer due to the electron backflow as well as low regeneration of ground state of $Cd_{33}Se_{33}$ QD; however it favors QD-dye bisensitizer, since the charge injections of dye sensitizer is greatly enhanced by QD co-sensitizer.

For the other binding configurations (2O-1S, 1S-1O-A, 1S-1O-B) in group III the relative positon of dye's HOMO with respect to the VB edge is similar to those of group I and II, while for LUMO it is dictated by $Cd_{33}Se_{33}$ QD. However, we found, the second highest metal state of dye is moved further away from the VB edge for the three configurations than other configurations (group I and group II) suggesting the extra isocyanate anchor changed the molecular orbital hybridization between QD and dye. This can be elucidated within the second-order perturbation

theory, in which the energy levels of new hybridized molecular orbitals are separated from the energy levels of isolated molecules by the sum of the orbitals of resonated states:[65]

$$\Delta E_{ij} = \sum_{i} \sum_{j} \frac{V_{ij}^2}{\Delta \varepsilon_{ij}} \tag{6.1}$$

where V_{ij} is the electronic coupling matrix, and $\Delta \varepsilon_{ij}$ is the energy gap between pairwise states. When the extra isocyanate anchor is attached to CdSe QD, it adds new contributions in eqn (6.1). The $\Delta \varepsilon_{ij}$ remains the same, since only binding geometries are changed, while the ligands still remain the same; however it does increase the magnitudes of coupling matrix elements, since the isocyanate anchor is close to the surface of $Cd_{33}Se_{33}$ QD increased the wavefunction overlapping. As such, it increases the energy separation shifting the bonding orbitals to lower energy levels, accordingly, the resonance region in density of states of $Cd_{33}Se_{33}$ QD is moved to deeper energy levels as well. Consequently, the metal state of dye is moved further away from the VB edge when hybridizing with QD state.

Therefore, when designing QD/dye composite sensitizer it needs to carefully consider the deprotonation scheme, for different combination of anchors changes the energetic alignment giving rise to different charge transfer diagrams. Especially, for larger QDs an increased number of carboxylate or isocyanate anchors thereof the binding geometries, are available to attach dye on QD's surface due to the reduced molecular strain of dye at the bulky surface.[39, 206] As such, the energetic alignment as well as the electronic coupling between the two molecules either fosters or inhibits the overall conversion efficiency of QD/dye sensitizer. It should be noted, our prediction on charge flow directions is in line with Ivan Mora-Sero et al's work,[28] where they experimentally measured the energy level alignment between $Cd_{33}Se_{33}$ QD and N719 dye, and hypothesize type I (electron forward-flow) and type II (electron back-flow) alignments are coexisted in CdSe

QD/N719 dye nanocrystal composite. Our computational work further reveals, in addition to theirs, such electron back-flow and forward-flow phenomenon are associated with different binding configurations of N719 dye on the surface of $Cd_{33}Se_{33}$ QD.

At last, adding solvent pushes the highest occupied dye states inside the VB edges (Figure 33), suggesting solvent stabilized the dye's orbitals with respect to QD's orbitals.

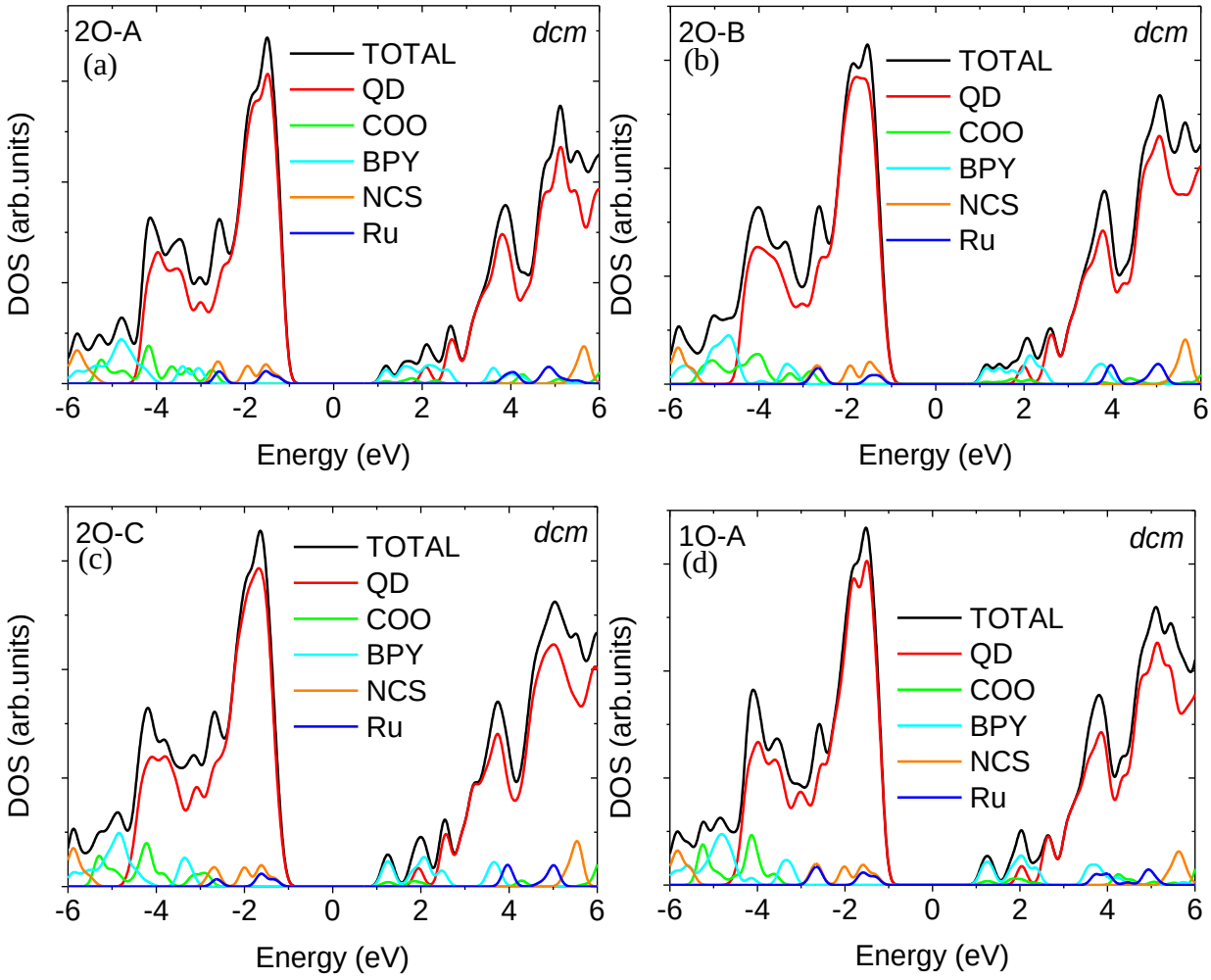

Figure 33. Projected density of states (PDOS) of Cd33Se33 QD/N719 dye nanocrystal composite, in dichloromethane (dcm).

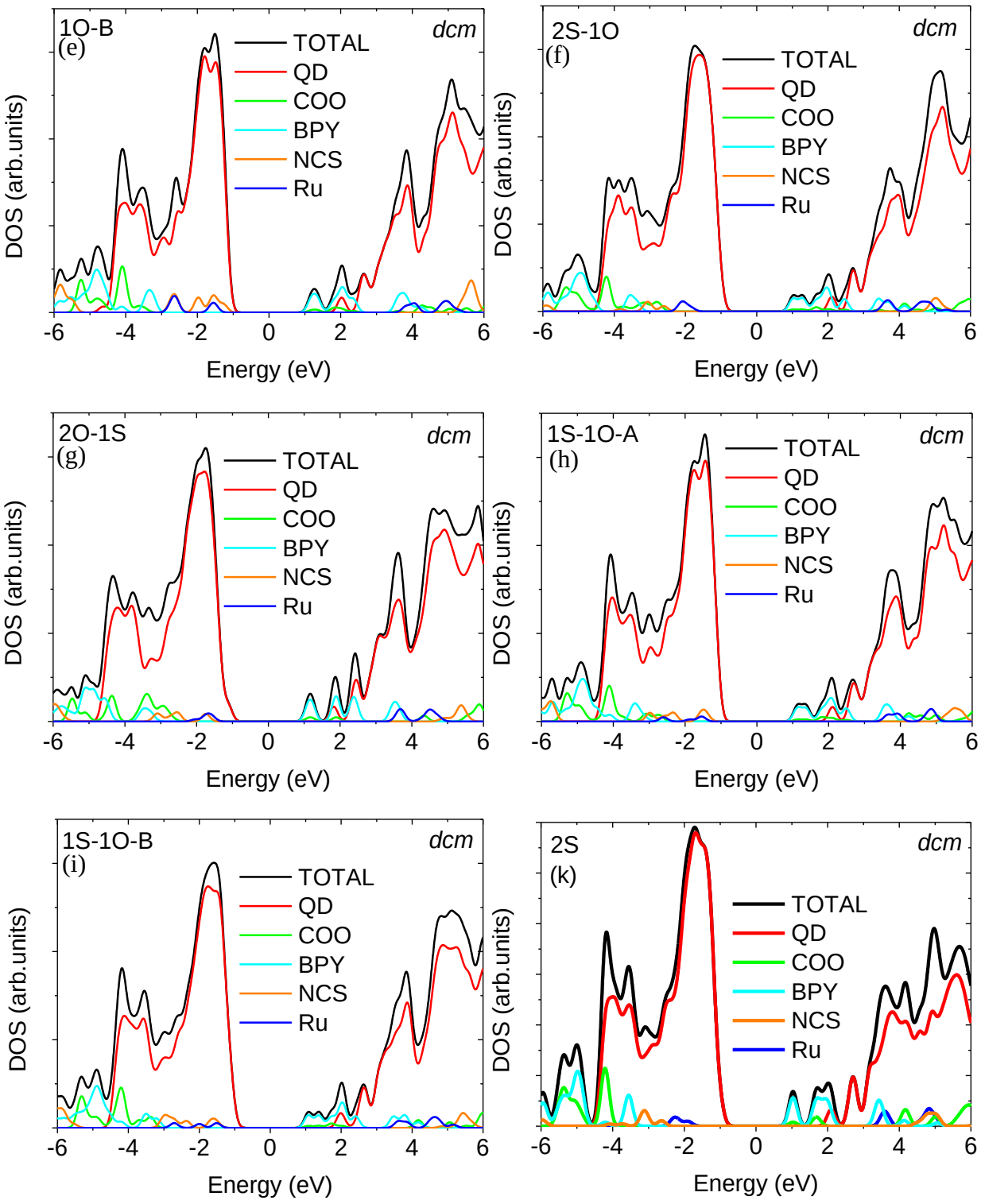

Figure 33. Projected density of states (PDOS) of $Cd_{33}Se_{33}$ QD/N719 dye nanocrystal composite, in dichloromethane (*dcm*) (continued).

6.1.3. Electronic coupling

As illuminated above, the electronic coupling determines the degree of molecular orbital hybridizations resulting in different energetic alignment. Another important aspect of electronic coupling is, it describes how strong the donor state is electronically coupled with acceptor state. The stronger of the coupling the faster of charge transfer occurs. Therefore, we calculate the electronic coupling vectors, in different binding geometry. The electronic coupling vectors of 2S and 2S-1O binding geometries are much larger than other configurations, ca. 10^{-3} orders of magnitude for electron transfer and ca. 10^{-2} orders of magnitude for electron & hole recombination. We further found, the donor-acceptor wavefunction overlappings of the two configurations are much larger than other configurations indicating large QD-dye correlations. Such strong correlation, as indicated earlier, changes the MOs altering the energetic alignment, in addition, it accelerates the charge transfer rates as well. Our speculation on the existence of strong correlation at charge localized state is supported by Liu et al's report,[207] where they use DFT calculations to show, the total thermodynamic free energy of P3HT/PCBM system at ground state is equivalent to the sum of the free energies of isolated P3HT molecule and isolated PCBM molecule; however they found such approach is invalid when they calculate for the charge localized state, in which there exists a strong coulomb interaction between positively charged donor molecule and negatively charged acceptor molecule, therefore donor and acceptor cannot be treated as isolated molecules. In addition, we found, in cases of 2S and 2S-1O configurations the lowest unoccupied QD state is placed in a much higher energetic level than the other configurations, which give rise to exceptionally strong coupling with the lowest unoccupied state as well as the ground state of dye due to the larger thermodynamic free energy difference.

If comparing the electronic coupling vectors of different binding geometries for electron transfer (*et*) and electron & hole recombination (*re*), it is found, they can be divided by two categories: (1) *et* coupling bigger than *re* coupling, i.e. 1O-A, 1O-B, 2O-A, 2O-B, 2O-C and 2S; (2) *et* coupling smaller than *re* coupling, i.e. 1S-1O-A, 1S-1O-B and 2S-1O. The former binding configurations reveal faster electron transfer, which is a typical phenomenon in ligated CdSe QD,[208-210] while the latter binding configurations reveal faster electron & hole recombination; however, the smaller binding energies in latter configurations indicate, the charge transfer in $Cd_{33}Se_{33}$ QD/N719 dye assemblies is dominated by the former binding configurations. As such, the electron & hole recombination does not play a dominant role in photoexcited charge carrier relaxation. In addition, it is found the larger donor-acceptor wavefunction-overlappings in 2S-1O, 1S-1O-B and 2S than other binding configurations play a vital role in regarding to the electron transfer and electron & hole recombination. Intuitively, in case of electron transfer the main contribution in donor-acceptor wavefunction-overlapping comes from the overlapping between LUMO levels of QD and dye, while in case of electron & hole recombination the main contribution in donor-acceptor wavefunction-overlapping comes from the overlapping between LUMO level of dye and HOMO level of QD. To this end, we found the linker length plays a vital role in determining the coupling between QD and dye, and generally, the shorter of linker the larger of coupling. Through the inspection, we found the length of isocyanate anchor is 2.83 angstrom, while the length of carboxylate anchor is 4.62 angstrom, which means the dye is more strongly coupled with the QD with isocyanate linking group in cases of 2S-1O, 1S-1O-B and 2S. We also noted, even though 1S-1O-A also uses the mixed isocyanate/carboxylate anchors to bind on the surface of QD, the isocyanate anchor forms 90 degree angle with the right side of carboxylate anchor, while it forms 90 degree angle towards the center of carboxylate anchor in case of 1S-1O-

B. This places the former one further away from the surface of QD, and thus, decreases the electronic coupling between QD and dye. As such, the electronic coupling of 1S-1O-B is larger than 1S-1O-A.

6.1.4. Optical absorption

Figure 34 shows the simulated absorption spectra of $Cd_{33}Se_{33}$ QD/N719 dye composite at different binding geometries, calculated with Casida formalism of linear response theory. All spectra show good additive features except 2S, 2S-1O and 1S-1O-B, in which the first absorption peak of isolated dye is split off the first absorption peak of QD/dye composite, caused by the relatively strong QD-dye correlations for the three binding configurations, as indicated by the exceptionally large donor-acceptor wavefunction overlappings in Table 13. Such strong correlation polarizes the QD/dye interface breaking the additive feature in low-energy absorption region. We further noted, the first absorption peak of isolated dye corresponds to the metal-to-ligand and π,π^* transitions. Since the correlation between QD and dye is strong, it gives rise to the resonance interaction between π orbitals in HOMO of dye and π orbitals of Se^{2-} ion near the VB edge, consequently, it changes the MOs of dye resulting in the first absorption peak of isolated dye split off the first absorption peak of QD/dye composite, thus the latter spectra is red-shifted.

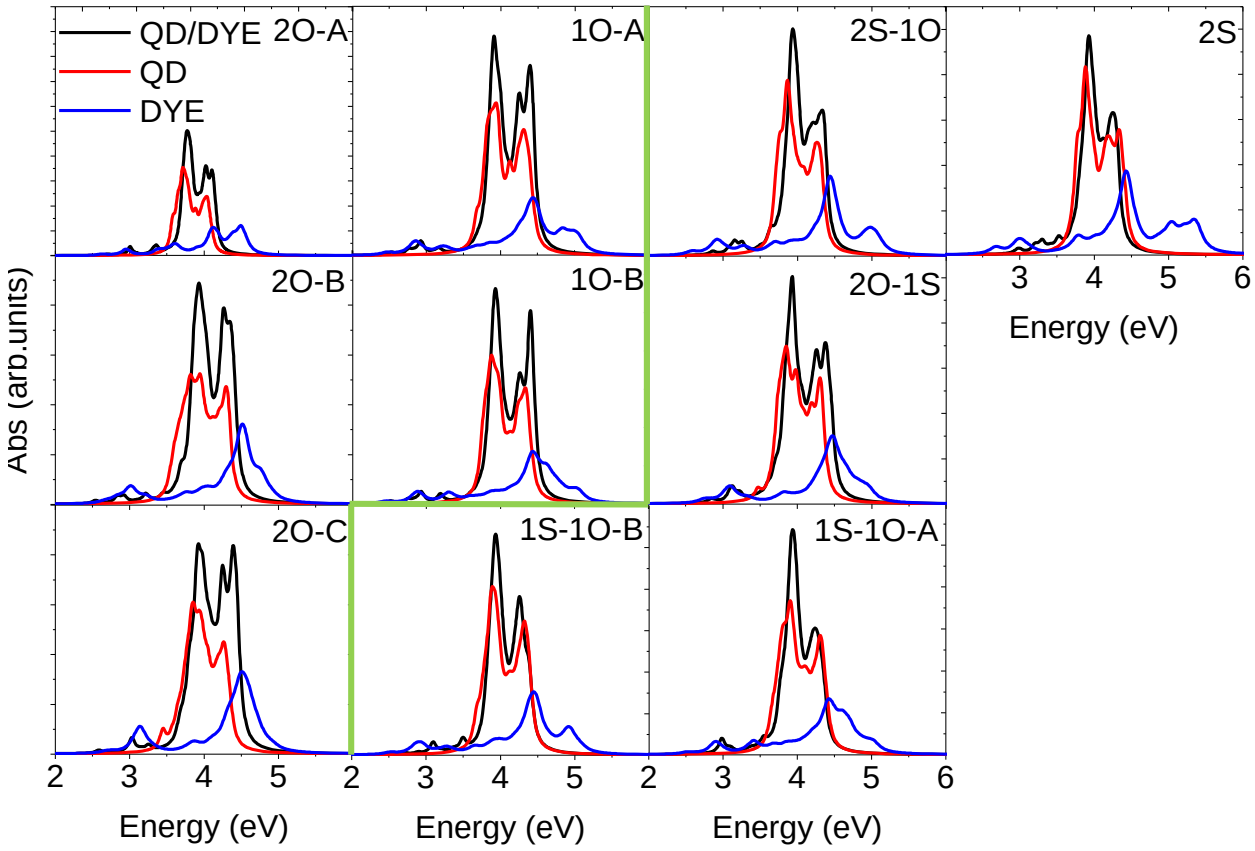

Figure 34. Absorption spectra of bare $Cd_{33}Se_{33}$ QD, isolated N719 dye as well as $Cd_{33}Se_{33}$ QD/N719 dye composite in dichloromethane. Both bare $Cd_{33}Se_{33}$ QD and isolated N719 dye are cut from QD/dye composite, afterwards TDDFT calculations are carried out using CAM-B3LYP functional. All spectra reveal good additive feature, i.e. the spectra profile of QD adding to the spectra profile of dye approximately equals to the spectra profile of QD/dye composite, which is typical in weakly correlated donor-acceptor system. However, there exists differences in low-energy region of the spectra between different binding geometries. In cases of 2S, 2S-1O and 1S-1O-B the first absorption peak of isolated dye is split off the first absorption peak of QD/dye composite, suggesting a polarization of interface region by QD-dye correlation, therefore the additive feature is not applicable to the low-energy region of spectra.

6.2. Summary

To summarize our work, we simulated the electronic structures and charge-transfer properties of $Cd_{33}Se_{33}$ QD functionalized by N719 dye at different binding geometries using density functional theory as well as charge-constrained density functional theory calculations. Through projected density of states we found, deprotonation site has a critical impact on the

energetic alignment between QD and dye. In particular, increasing the distance between deprotonation sites reduces the electronic coupling between QD and dye, which indicates, when designing QD/dye sensitizer a pre-knowledge of the deprotonations of dye structure is very important for controlling the charge carrier mobility in QD/dye nanocrystal composite. Negatively charged isocyanate ligand destabilizes dye's highest occupied orbitals making the hole transfer from QD to dye possible. In addition, it also increases the degree of molecular orbital hybridizations between QD and dye resulting in the highest occupied metal states further away from the VB edge. Adding solvent delocalizes the electron densities between $Cd_{33}Se_{33}$ QD and N719 dye removed the surface trap states, which is important to improve the charge carrier mobility in QD/dye nanocrystal system.

Though performing charge-constrained DFT calculations, we show, in most binding configurations electrons flow forwardly from dye to QD, and transferred faster than electron & hole recombination at charge localized adiabatic crossing region, which is similar to dye sensitized anatase based solar cell, and benefits the overall conversion efficiency of QDs based solar cell. A further optimization of light conversion efficiency is possible through increasing the electronic coupling between QD and dye.

Through time-dependent density functional calculation, we found, some binding geometries result in the isolated dye states split off the first absorption peak of $Cd_{33}Se_{33}$ QD/N719 dye composite due to the polarization of interfaces. Consequently, it breaks the additivity, and results in the red-shift of the spectra.

CHAPTER 7. NONADIABATIC CHARGE-CARRIER RELAXATION IN $Cd_{33}Se_{33}$ QD/Ru(II) POLYPYRIDINE NANOCOMPOSITE

In previous three chapters, we simulated CdSe QDs functionalized by dye using DFT, TDDFT and charge constrained DFT calculations, and show: (1) negatively charged ligand destabilizes the highest occupied orbital of dye, driving dye state out of the VB edge of QD; (2) solvent delocalizes electrons at the QD surface; (3) QD-dye interaction changes the interfacial hybridization of molecular orbitals giving rise to different energetic alignment. In this chapter, we proceed to study the relaxation and charge transfer dynamics.

7.1. Results and Discussion

7.1.1. Ground-state electronic properties and optical spectra

Figure 35 shows the projected density of states (PDOS) at ground state. GGA functional is well-known for underestimating the band gap. One way to bypass the flaw is to use scissor operation opening the band gap. Figure 35 (c) shows, after scissor operation, the profiles of PDOS calculated by PBE functional are very similar to that of PBE1 functional (Figure 35 (a)), especially the energetic alignment between the highest occupied states of $Cd_{33}Se_{33}$ QD and black dye. The highest occupied state is dominated by black dye, while the lowest unoccupied state is dominated by QD. PBE1 functional (Figure 35 (a)) predicts a band gap ca. 1 eV, one the contrary, PBE functional largely underestimates the band gap. It should be noted, the plane wave basis set implemented in VASP is more complete than spherical basis set. If comparing the band gaps calculated by VASP (Figure 35 (a)) and Gaussian09 (Figure 35 (b)) software packages, the former one is larger than the latter one and therefore closer to the experimental value.

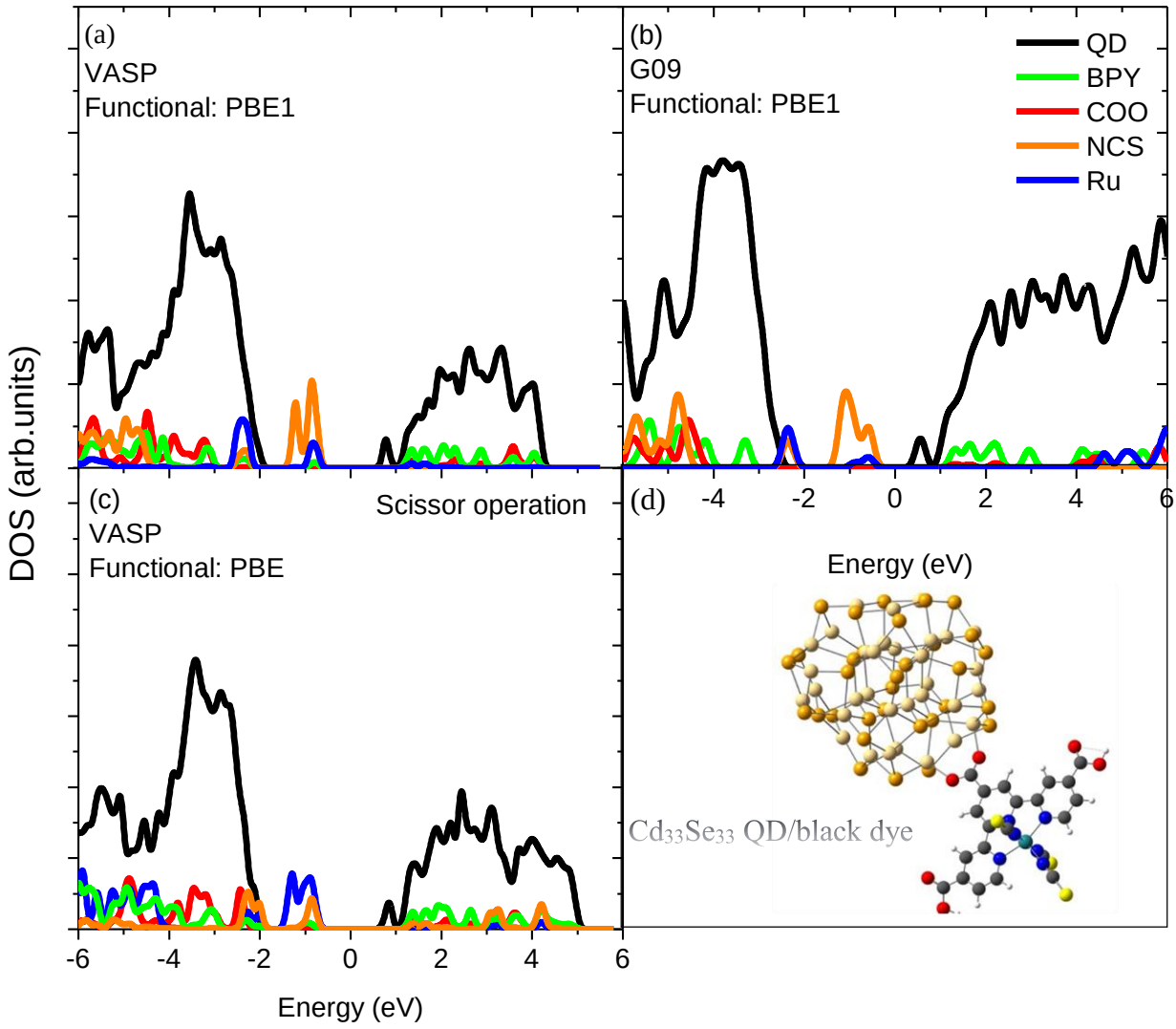

Figure 35. Black dye functionalized $Cd_{33}Se_{33}$ QD. Black dye is attached to $Cd_{33}Se_{33}$ QD with carboxylate anchoring group. The profiles of PDOS calculated by Gaussian09 and VASP software packages are highly similar to each other, (a) and (b). The highest occupied state of energy levels is dictated by the Ruthenium ion as well as related isocyanate anchoring group, while the lowest unoccupied state is dictated by QD. After scissor operation the profile of PDOS calculated by PBE functional highly resembles the hybrid functional.

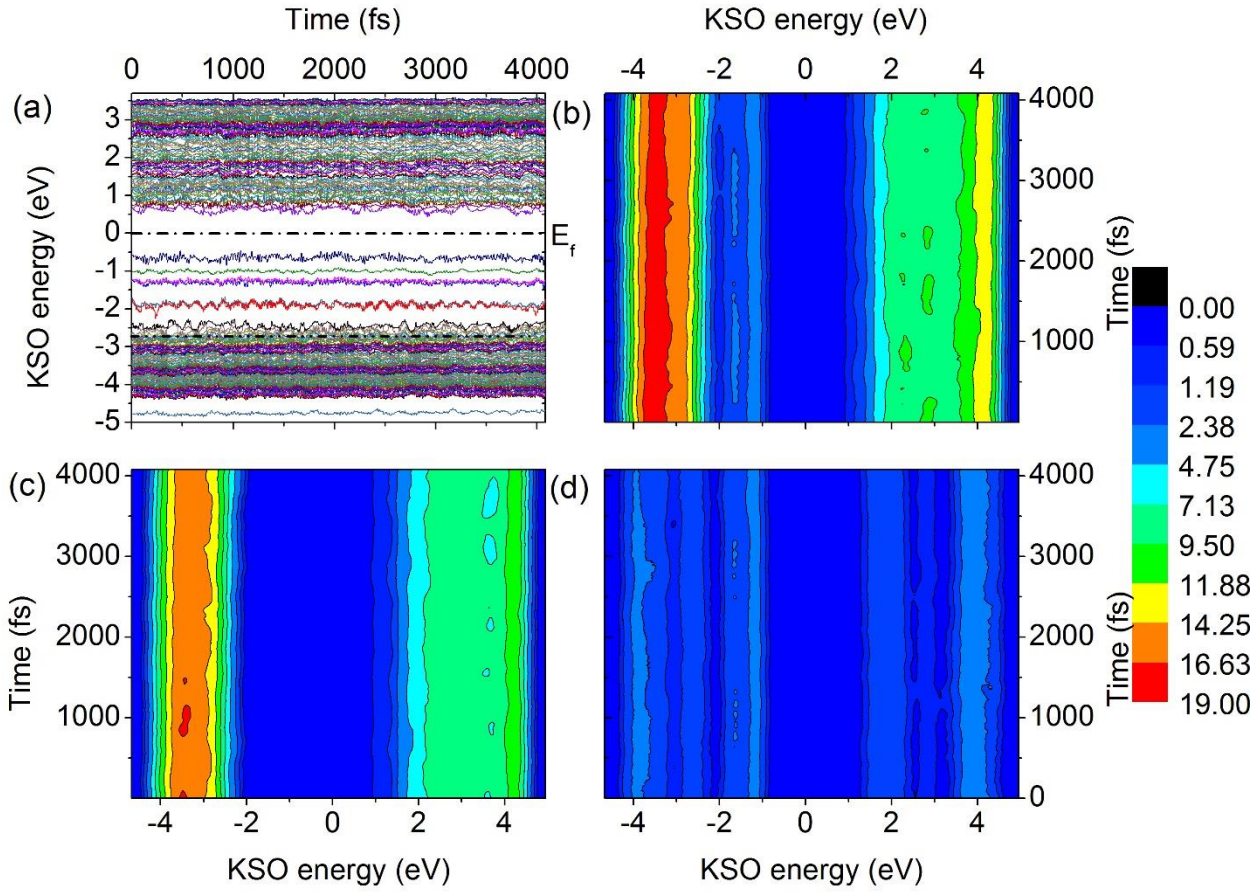

Figure 36. (a) Fluctuation of time-evolved Kohn-sham orbital (KSO) energies of $Cd_{33}Se_{33}$ QD/BD dye composite. E_f is the fermi level. The energy spacing in valence band is relatively smaller than conduction band indicating the density of states of hole denser than electron. Several highest occupied KSOs near the E_f separated from the main bands consists of dye character indicating QD redoxed by dye during the charge carrier relaxation. (b) is time-evolved total density of states, and (c) and (d) are time-evolved projected density of states onto the QD and dye, respectively.

Figure 36 (a) is time-evolved Kohn-sham orbital (KSO) energies (after scissor operation) providing the information about energy fluctuation of Kohn-sham orbitals along with time. The total band gap remains relatively constant over the time with periodic fluctuation corresponding to nonadiabtic recombination. Several highest occupied KSOs near the Fermi level are energetically separated from the other occupied KSOs. By projecting the total density of states onto QD (c) and dye (d), we found those highest occupied KSOs are exclusively dominated by dye character

indicating $Cd_{33}Se_{33}$ QD redoxed by dye during the charge-carrier relaxation. The profiles of total density of states of $Cd_{33}Se_{33}$ QD/BD dye composite are different in VB and CB indicating asymmetrical excitation across the band gap. The relatively smaller energy spacing in VB than CB indicates a heavier effective mass of hole than electron. In addition, the total density of states remains relatively constant against the time indicating the static density distribution barely affected the charge transfer property at the interface.

The time-averaging Kohn-sham optical spectra (Figure 37) is obtained by applying independent particle approximation [211]

$$\langle a(\omega)\rangle = \frac{1}{T}\int_0^T a\left(\hbar\omega, \vec{R}_I(t)\right) dt \tag{7.1}$$

$$a\left(\hbar\omega, \vec{R}_I(t)\right) = \sum_{ij} f_{ij}\left(\{\vec{R}_I(t)\}\right)\delta\left(\hbar\omega - \hbar\omega_{ij}\{\vec{R}_I(t)\}\right) \tag{7.2}$$

$$f_{ij}\left(\{\vec{R}_I(t)\}\right) = \frac{4\pi m_e \omega_{ij}}{3\hbar e^2}\left|\vec{D}_{ij}\right|^2 \tag{7.3}$$

$$\vec{D}_{ij}\left(\{\vec{R}_I(t)\}\right) = e\int \varphi_i^{KS^*}\left(\{\vec{R}_I(t)\}\right)\vec{r}\,\varphi_j^{KS^*}\left(\{\vec{R}_I(t)\}\right)d\vec{r} \tag{7.4}$$

Where $f_{ij}\left(\{\vec{R}_I(t)\}\right)$ is the oscillation strength giving the probability of electronic transition, $\vec{D}_{ij}$ is the transition dipole moment between quantized energy level i and energy level j. In order to correctly apply Kohn-sham formalism to describe optical transition, the coulomb interactions in photoexcited electron-hole pairs must be negligible comparing with quantization effect, as such, the kinetic energy term dominates the Hamiltonian of photoexcited charge carrier, therefore independent particle approximation based on the zero-order electronic wavefunction becomes the

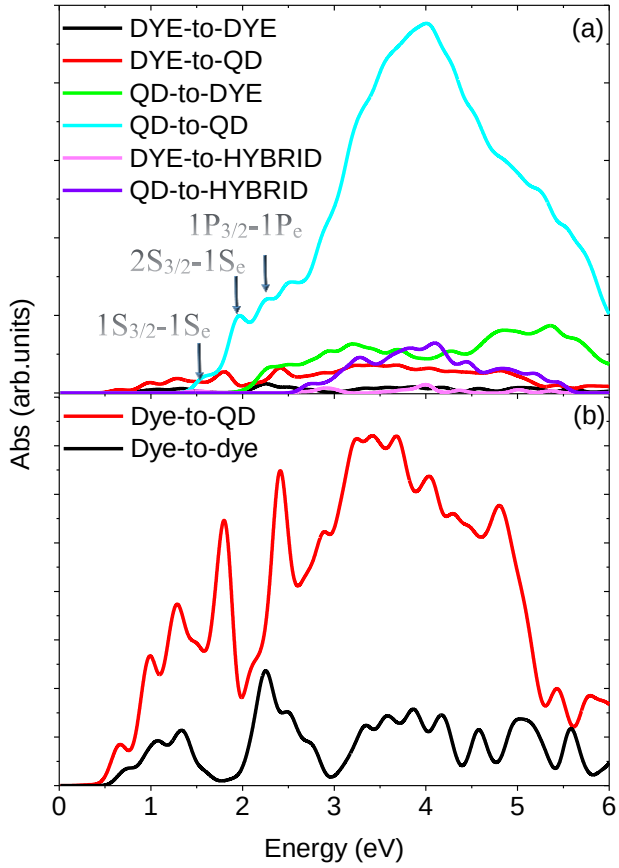

Figure 37. Time-averaged decomposed Kohn-Sham absorption spectra, where the optical transitions are governed by the occupied- and unoccupied quantized energy levels. Each quantized energy level is composed of QD state and dye sate. At the energy range between 0 eV and 1.8 eV only dye-QD and dye-dye charge-transfer excitations occur, where the amplitude of dye-QD transitions are much larger than dye-dye transitions. At the energy range between 1.8 eV and 2 eV the absorption is dominated by QD-QD and dye-QD transitions. Above 2eV the absorption is dominated by QD-QD symmetric transitions, indicated by arrows.

valid picture. This further requires the size of material is smaller than its bohr radius, which is a valid assumption for $Cd_{33}Se_{33}$ QD. To project the spectra on the specified fragment, the whole system is divided by the regions of $Cd_{33}Se_{33}$ QD and BD dye, respectively, and quantized energy level is decomposed as the admixture of QD state and dye state. When the ratio λ between QD and dye states is between the lower threshold limit and upper threshold limit, e.g. $40\% < \lambda < 60\%$, the energy level is dictated by the hybrid state, otherwise, it is dictated by the fragment corresponding to the high-percentage state. In order to make the hybrid state contain approximately

equal amount of $Cd_{33}Se_{33}$ QD- and BD dye states, we set 40% as lower limit and 60% as higher limit. Figure 37 (a) shows, at the low energy range (0~1.8 eV) the photoexcitation is dominated by dye-dye and dye-QD transitions, where the amplitude of dye-QD transition is larger than that of dye-to-dye transition; at the medium energy range (1.8~2 eV) both QD and dye are photoexcited, and QD-QD transition emerges; at the high energy range (>2 eV) QD-QD transition has a significantly larger amplitude than other transitions. It should be noted, the dye-dye transition as well as dye-hybrid transition is likely to be blue-shifted due to the Kohn-sham formalism underestimated the excitonic effect. This brings further impact on the initial distribution of electron populations upon photoexcitation, which should follow the trend of transition amplitudes at different excitation levels. In case of asymmetric excitation, the transition amplitude is given as Gaussian function

$$f_{unsym}(i) = os(i) \times e^{-\frac{(dE(i)-E_{ex})^2}{\sigma}} \tag{7.5}$$

Where $os(i)$ is the oscillation strength, dE(i) is the energy gap between two transition states, σ is the line width, and E_{ex} is the reference energy to control the amplitude of excitation level. The index i runs over all possible optical transitions. The KSO energies of two transition states corresponding to the largest $f_{unsym}(i)$ provides the initial excitation levels for electron and hole, respectively. By summing over 300 nuclear trajectories a statistical distribution of electron or hole population is obtained as the starting point for propagating the electronic coefficient, and nuclear trajectory hopping is governed by the probability of state-to-state transition. In case of symmetric excitation, the transition amplitude is given by multiplying eqn. (7.6) with one additional Gaussian function

$$f_{sym}(i) = f_{unsym}(i) \times e^{-\frac{(exEe-exEh)^2}{\sigma}} \quad (7.6)$$

Where exEe is the energy difference between the LUMO and the unoccupied KSO, while exEh is the energy difference between HOMO and occupied KSO. The statistical distribution of initial charge carrier in symmetric case is the same as the unsymmetric case. In previous work of electronic dynamics in PbSe and CdSe QDs, we scale the total band gap (E_g) of QD as the reference energy (e.g. $1E_g$, $2E_g$, etc) to control the excitation level. However, scaling the total band gap of QD/dye composite provides incorrect reference energy, since the exciton effect of dye is underestimated in Kohn-sham spectra. Instead, we choose to scale the total band gap of QD to place the initial photoexcited electron-hole pair in $Cd_{33}Se_{33}$ QD. Consequently, the nuclear trajectory is dominated by the quantum forces of QD rather than dye during charge-relaxation molecular dynamics. Since one of our approximations is based on using the ground-state nuclear trajectory to mimic excited-state nuclear trajectory, it requires a negligible electron-hole coulomb interaction with respect to the many-body electronic effect at ground state, which results in the quantum forces governed by ground-state electronic Hamiltonian. Such assumption is correct only if the leading contribution for electronic Hamiltonian comes from the kinetic energy term, as such, the initial charge carriers must be mainly distributed in QD rather than dye, where the quantization effect prevails over the electron-hole correlation making the kinetic energy dominate the electronic Hamiltonian.

The arrows in Figure 37 (a) mark the three lowest optical transitions, consistent with the experimental results [212, 213] as well as KP theory predictions[96]. The S-S and P-P transitions are in consistent with the selection rules that allows for strong optical transition. The spin-coupling effect is not considered in our model, therefore the spin-split band as well as the resultant orbital angular

momentum $S_{1/2}$ is not present in hole states. The asymmetry of the DOS of CdSe QD indicates the optical transitions occur without symmetry restriction, unlike PbSe QD [110]. Therefore, the initial populated states are chosen from those states having the largest optical activity.

7.1.2. Time-domain photoinduced electron- and hole relaxation

After reaching thermal equilibrium the stochastic molecular dynamics is performed to provide the nuclear-trajectory ensembles. A total of 300 nuclear trajectories are obtained in prior to propagate the electronic coefficient, afterwards the Tully surface hopping scheme is used to obtain the state-to-state transition probability.

Figure 38 (a) shows, shows, the exciton (electron-hole pair) dissociation occurs within 30 femtosecond, afterwards, the total energies are relaxed through coupling electronic states with nuclear vibrational modes. The electron is relaxed significantly slower than hole. Interestingly, the relaxation energies are decayed exponentially along with time (Figure 40). This indicates the relaxation dynamics in dye functionalized $Cd_{33}Se_{33}$ QD is quite different than bare PbSe QD that is reported previously[77]. The energy relaxation of latter one is fitted well by Gaussian plus exponential fit suggesting two-stage relaxation dynamics; however in case of dye functionalized $Cd_{33}Se_{33}$ QD only two exponential components works well, i.e.

$$y = y0 + A1 * exp\left(-\frac{x - x0}{t1}\right) + A2 * exp\left(-\frac{x - x0}{t2}\right) \qquad (7.7)$$

Where *y0*, *A1*, *A2*, *x0* and $t1$ are fitting parameters. *A1* and *A2* correspond to the percentages of each component, respectively, while $t1$ and $t2$ correspond to the relaxation times of each component, respectively.

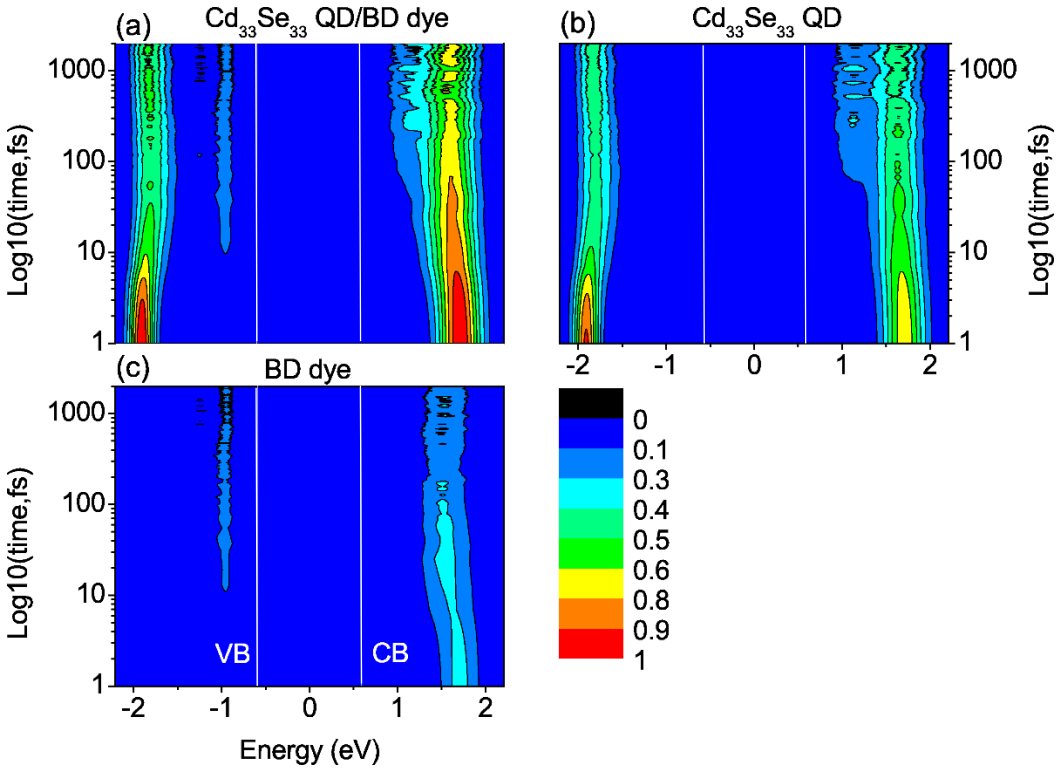

Figure 38. (a) Time-evolved electronic- and hole relaxation-dynamics by multiplying DOS by the corresponding state occupations. (b) and (c) are projected dynamics onto $Cd_{33}Se_{33}$ QD and BD dye, respectively. The initial excitation level of electron is about 0.6 eV higher than the CB edge, while for hole it is about 0.7 eV lower than the VB edge. The y axis time scale is logarithmic for showing the initial moment of population dynamics corresponding to a shorter time scale of exciton dynamics.

By fitting the exponential components, the electron relaxation consists of a fast component of 19 femtoseconds and a slow component of 365 femtoseconds, and hole relaxation consists of a fast component of 11 femtoseconds and a slow component of 92 femtoseconds. The time scale obtained through our simulation occurs much faster than that of experiments due to small size of $Cd_{33}Se_{33}$ QD accelerated the relaxation. The initial stages of electron- and hole relaxations occurs in a few tens of femtoseconds, and afterwards the electrons are relaxed much slower than holes due to the phonon bottleneck when the relaxations proceed to the band edges.

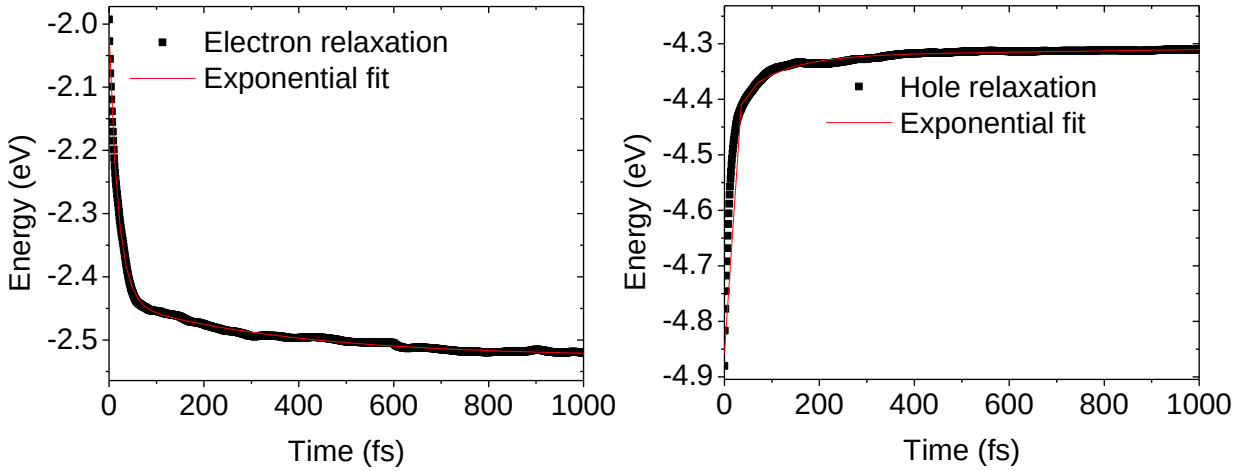

Figure 39. Exponential fitting of energy relaxation of electron- and hole dynamics.

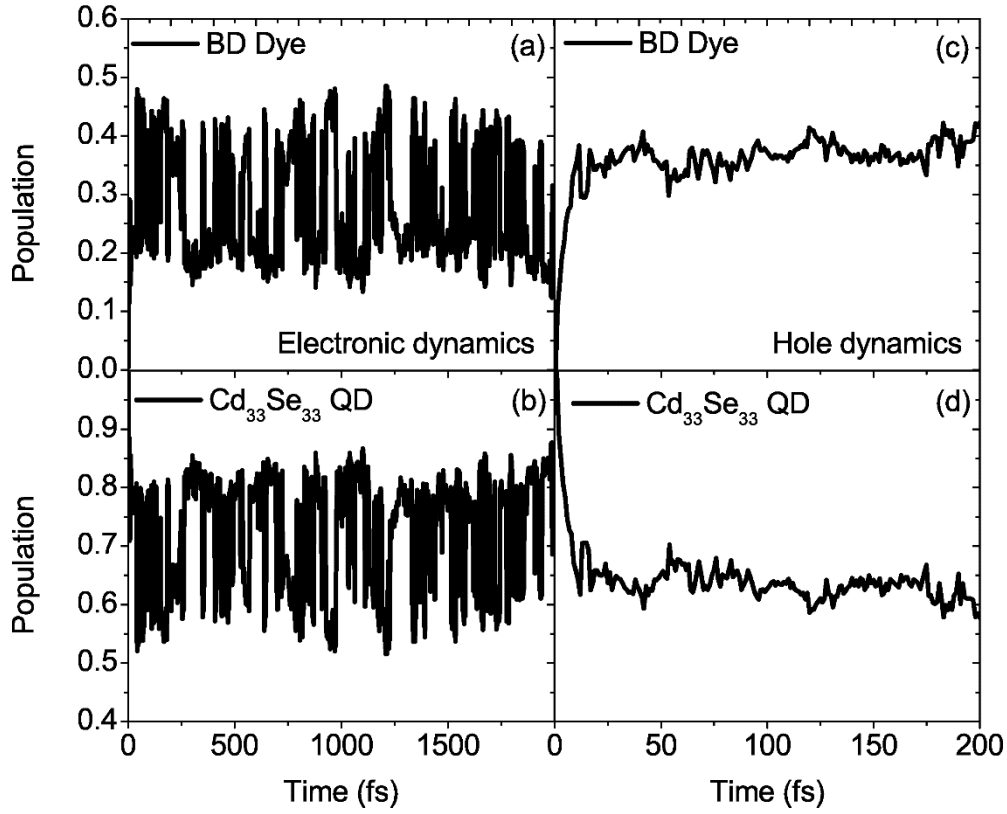

Figure 40. Projected electronic- and hole population dynamics onto the $Cd_{33}Se_{33}$ QD (lower panel) and the BD dye (upper panel), respectively. (a) and (b) show, the populations are fluctuated in $Cd_{33}Se_{33}$ QD and BD dye during the relaxation, while (c) and (d) show, there is a significant population injection from $Cd_{33}Se_{33}$ QD to BD dye at the initial phase of relaxation dynamics.

The electronic population emerged near the band edge occurs in ca. 800 femtoseconds during the relaxation; however it occurs much faster for hole, i.e. ca. 200 femtoseconds. Both

electron and hole are not fully relaxed to the band edges at the end of the dynamics; however, due to different cause. For electron, the energy spacing near the band edge is much larger than those of high-lying states, as such, the near-edge electronic states are weakly coupled with nuclear vibrational modes, consequently, the relaxation dynamics is largely slow down near the band edge, and mainly modulated by the electronic dephasing effect. On the contrary, the density of states of hole for $Cd_{33}Se_{33}$ QD is much denser than electron, as such, the phonon bottleneck is unlikely to be observed for hole relaxation dynamics, as evidenced in many experiments. However, as indicated earlier, the highest occupied state is dominated by BD dye instead of $Cd_{33}Se_{33}$ QD, as such, the hole transfer as well as the ensued relaxation in BD dye dominates the time scale of hole relaxation near the band edge.

Figure 40 shows, the electronic population is fluctuated along with the time suggesting electronic states strongly resonate with phonon frequencies, on the contrary, the hole population is relatively stable against the time due to the much heavier effective mass. Figure 42 shows the Fourier transforms of the energy gaps between the initially excited MOs and HOMO/LUMO states. It is similar to that has been studied in PbSe QD [77], the spheroidal acoustic phonons with frequencies around 100 cm^{-1} dominate both electron and hole dynamics. We also observe the longitudinal optical modes with frequency around 200 cm^{-1} presented in the spectra. Even though the majority part of spectra for electron and hole are similar in regarding to the amplitude and frequencies, it should be noted the electron is coupled with a higher frequency phonon mode around 800 cm^{-1}. This is given by the fact that the energy spacing in unoccupied level is larger than occupied level, as such, the electronic states are placed in higher energy levels containing more nodes, thus coupled more effectively with high frequency phonons.

Figure 40 shows both electron and hole demonstrate ultrafast hot carrier injections from QD to dye at the initial moment of relaxation dynamics due to the energy exchange between the hybridized states of QD and dye as well as the electronic coupling effect. The initial electronic population in BD dye emerges in ca. 10 fs (Figure 43). Such time scale is too short to be accommodated by nuclear motion, therefore, it is a direct charge injection through electronic coupling between high-lying state of QD and low-lying state of dye. Similar phenomenon had been observed in dye sensitized TiO_2 anatose, where ultrafast charge injection occurs upon the initial photoexcitation corresponding to the hot carrier injection due to the electronic coupling effect. At the later time of relaxation dynamics, the electron population in dye is reduced against $Cd_{33}Se_{33}$ QD suggesting a dye-to-QD electron transfer due to the lowest unoccupied state dominated by $Cd_{33}Se_{33}$ QD. The phonon bottleneck near CB edge improves the electron injection from QD to dye, since electron gains extra lifetime in CB in prior to return to the ground state. On the contrary, the hole transfer occurs in a few tens of femtoseconds, as indicated by the decay of population curves against the time in Figure 40 (b). This agrees well with experimental observation, where the faster hole-transfer greatly improves the overall conversion efficiency in CdSe QD/BD dye composite[46]. Figure 44 shows the total populations corresponding to five highest occupied dye states. After 2000 fs relaxation dynamics about 70% charge-carrier populations reaches the LUMO of $Cd_{33}Se_{33}$ QD, on the contrary, there is about 30% populations distributed in BD dye, while only a small amount of charge-carriers remain in the highest occupied MO of $Cd_{33}Se_{33}$ QD, indicating the rest of hole population transferred to BD dye.

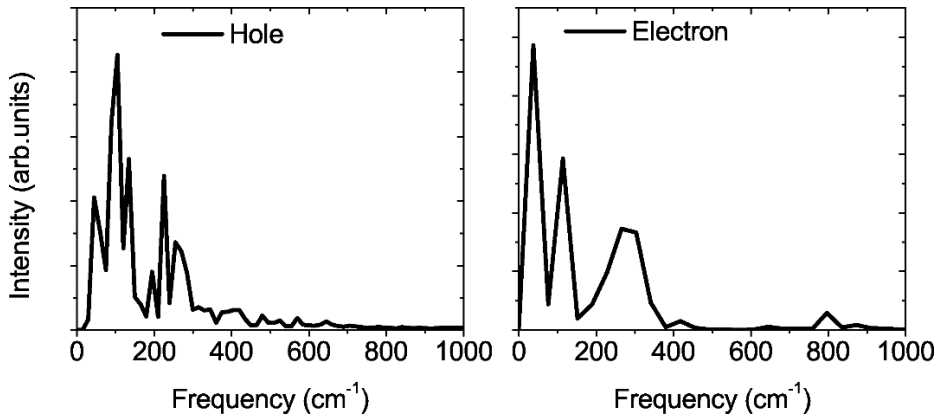

Figure 41. Fourier transforms of the energy gaps between initially excited MOs and HOMO/LUMO states of holes (a) and (b) electrons. Both charge carrier couple with low frequency phonons, with electrons coupled to a slightly higher frequency mode (ca. 800 cm^{-1}).

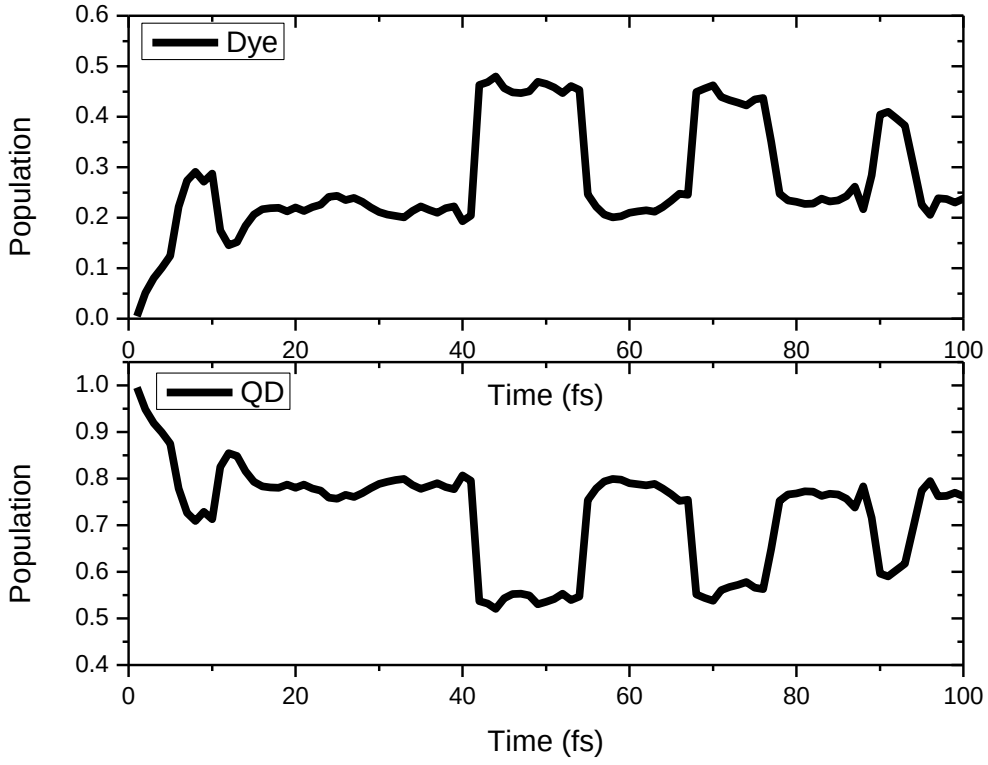

Figure 42. The initial moment of electron relaxation in $Cd_{33}Se_{33}$ QD/BD dye.

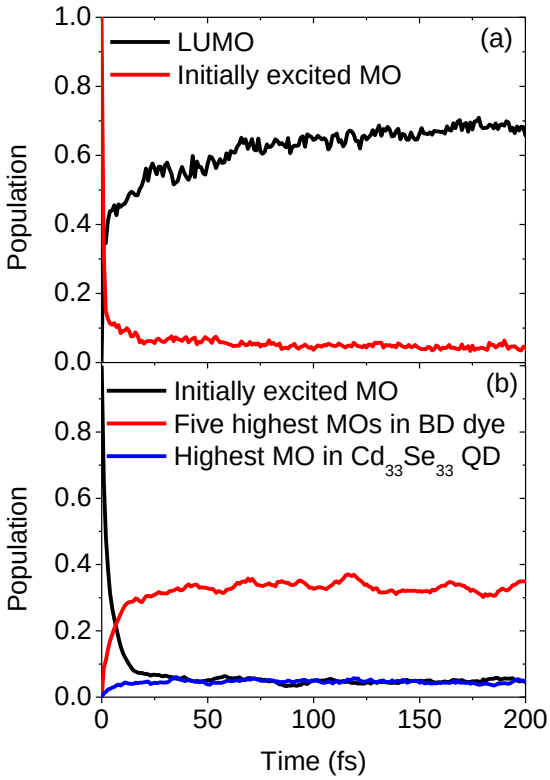

Figure 43. Time-dependent populations of molecular orbitals (MOs) in CB (upper panel) and VB (lower panel). The five highest occupied MOs in VB are dominated by BD dye.

7.2. Summary

To summarize our work, we apply time-dependent density functional theory to explicitly solve the electronic coefficient at each time step by expanding the time-dependent wavefunction as a linear combination of Kohn sham basis function. Tully surface hopping scheme is used to obtain the state-to-state transition rates that governs the nuclear hops between electronic potential surfaces. Such method is durable for the large-scale modelling of nonadiabatic charge transfer, and we apply it to study the relaxation dynamics as well as charge transfer in CdSe QD/BD dye nanocrystal composite.

Our results suggest, the ground-state density of states are unsymmetrically distributed among conduction- and valence bands indicating the unsymmetric optical transition that is served

as the initial condition for the electronic dynamics. By projecting the total density of states onto QD and dye, we obtain the PDOS. The overall profiles of PDOS as well as their relative positions with respect to fermi level are highly similar by comparing GGA functional (PBE) with hybrid functional (PBE1). Therefore, approximating the exchange-correlation part in electronic Hamiltonian with GGA functional provides correct predictions on the charge-carrier populations as well as charge transfer time-scale, which further indicates it is a durable way to simulate the materials in large scale and condensed phase. The projected Kohan-sham spectra not only provides the information about optical transition strength, but also tells which component governs the optical transition. Especially, for CdSe QD/BD dye nanocrystal composite the optical transition is governed by dye-QD and dye-dye transitions at low energy range, while QD-QD transition dominates the high energy range.

At the initial moment of relaxation dynamics a hot charge-carrier injection occurs for both electron and hole due to the electronic coupling as well as the energy exchange of hybridized states between QD and dye, which could be used as improving the conversion efficiency of CdSe QD/BD dye nanocrystal composite solar cells. The initial exciton dissociates within 10 fs followed by a slow relaxation dynamics coupled with nuclear motion. The population fluctuation of electronic states is much larger than that of hole states during the dynamics indicating the electronic states coupled strongly with nuclear vibrational modes, on the contrary, the fluctuation is much smaller in case of hole due to the heavier effective mass. Through exponential fitting, we obtain the time scales for electron- and hole relaxation dynamics suggesting a faster hole transfer than electron transfer. In addition, the phonon bottleneck occurs near the band edge in case of electron, while for hole dynamics no phonon bottleneck is observed due to the hole transferred from QD to dye.

CHAPTER 8. CONCLUSION

In this thesis, we use the DFT method, and, in combining with Tully fewest switched surface hopping scheme to address the dye functionalization effect on interfacial energetic alignment as well as the charge-carrier relaxation dynamics in QD/dye nanocrystal composite, and demonstrate such alignment being affected by the metal ion, organic ligands as well as binding geometry of dye. Our work shows, changing metal ion changes the alignment between the highest occupied MO levels of QD and dye, and the alignment between the lowest unoccupied MO levels of QD and dye, respectively. In general, increasing the electronegativity of metal ion increases the energy difference between the highest occupied states, while decreases the energy difference between the lowest unoccupied states. The large QD-dye dipole interaction reduces the d_{z^2} orbital electron density of metal ion, subsequently perturbs the trend of metal-ligand interaction against the electronegativity of metal ion. In particular, the dipole interaction increases the long-range resonant interaction between QD and dye, consequently, it increases QD-dye charge transfer interaction upon the photoexcitation. This brings the important applications of photosensitizers in serving some special purposes of photovoltaic devices. For instance, instead of QD as sensitizer another designing philosophy is to use dye as sensitizer, as such, the initial photoexcitation from QD to dye increases the total amounts of charge carriers injected to photoelectrode improving the conversion efficiency. However, changing metal ion does not provide the favorable thermodynamic condition for hole transfer. On the other hand, negatively charged ligands as well as less polarized solvent destabilizes the highest occupied MO of dye pushing it out of the VB edge of QD, and allowing for hole transfer from QD to dye. In addition, the presence of small ligands affects the MLCT optical transitions in the lowest energy absorption bands of QD/dye composite. Different binding geometry of dye at CdSe QD surface results in different electronic

coupling between QD and dye giving rise to different energetic alignment due to the interfacial electronic effect. Those alignments yield both electron forward-transfer and back-transfer in a statistical ensemble of QD/dye nanocrystal composites manipulated via binding geometry. In particular, if the ionization potential of isolated dye is placed in a high energetic position that cannot form the effective resonant interaction with VB of QD, only the bonding molecular orbital is appreciably populated, while the antibonding orbital is dominated by dye, which pushes the dye state deep inside the VB edge of QD. At last, we performed the nonadiabatic molecular dynamics to study the charge-carrier relaxation as well as charge transfer across the heterogeneous interface of $Cd_{33}Se_{33}$ QD/BD dye nanocrystal composite. Through the fewest switched surface hopping scheme, the nuclear trajectory is hopped between different electronic potential surface guided by the state-to-state transition probability. The hole relaxation reveals a faster time scale than electron relaxation, due to the denser distribution of density of states in valence band than conduction band. At the initial moment of relaxation dynamics there is a hot charge-carrier injection from QD to dye due to the electronic coupling and energy exchange between the hybridized states of QD and dye, and the initial hole populations emerged in dye takes place in ten femtoseconds. The hole transfer process lasts for ca. 50 femtosecond, while electron transfer still takes place in 2 picoseconds. Both electron and hole couple with low frequency vibrational modes of nuclear, with electron couples with a slightly higher frequency mode.

Through the thesis we pave the way for understanding the role of QD-dye interaction in electronic coupling as well as interfacial charge transfer property in QD/dye nanocrystal composite, and providing the detailed studies from the aspects of chemical structure and binding geometry of dye, QD-dye dipole interaction, QD-dye electronic coupling as well as the real-time charge transfer across the interface of QD/dye nanocrystal composite.

REFERENCES

1. K. M. Karlsson, 2011.
2. A. Hagfeldt and M. Grätzel, *Accounts of Chemical Research*, 2000, **33**, 269-277.
3. C. R. Wronski, 2000.
4. A. Hagfeldt, G. Boschloo, L. Sun, L. Kloo and H. Pettersson, *Chemical reviews*, 2010, **110**, 6595-6663.
5. G. Chen, J. Seo, C. Yang and P. N. Prasad, *Chem Soc Rev*, 2013, **42**, 8304-8338.
6. M. A. Green, *Third generation photovoltaics*, Springer, 2006.
7. I. Mora-Seró and J. Bisquert, *The Journal of Physical Chemistry Letters*, 2010, **1**, 3046-3052.
8. L. M. Peter, *The Journal of Physical Chemistry Letters*, 2011, **2**, 1861-1867.
9. D. Kuang, C. Klein, Z. Zhang, S. Ito, J. E. Moser, S. Zakeeruddin and M. Grätzel, *Small*, 2007, **3**, 2094-2102.
10. Q. Wang, S. M. Zakeeruddin, M. K. Nazeeruddin, R. Humphry-Baker and M. Grätzel, *Journal of the American Chemical Society*, 2006, **128**, 4446-4452.
11. M. K. Nazeeruddin, P. Liska, J. Moser, N. Vlachopoulos and M. Grätzel, *Helvetica Chimica Acta*, 1990, **73**, 1788-1803.
12. M. Matsumura, Y. Nomura and H. Tsubomura, *Bulletin of the Chemical Society of Japan*, 1977, **50**, 2533-2537.
13. N. Alonso, M. Beley, P. Chartier and V. Ern, *REVUE DE PHYSIQUE APPLIQUEE*, 1981, **16**, 5-10.
14. J. Desilvestro, M. Graetzel, L. Kavan, J. Moser and J. Augustynski, *Journal of the American Chemical Society*, 1985, **107**, 2988-2990.
15. T. Horiuchi, H. Miura and S. Uchida, *Chemical Communications*, 2003, 3036-3037.
16. H. Zhou, Q. Chen, G. Li, S. Luo, T.-b. Song, H.-S. Duan, Z. Hong, J. You, Y. Liu and Y. Yang, *Science*, 2014, **345**, 542-546.
17. N. J. Jeon, J. H. Noh, Y. C. Kim, W. S. Yang, S. Ryu and S. I. Seok, *Nature materials*, 2014.
18. A. Marchioro, J. Teuscher, D. Friedrich, M. Kunst, R. Van De Krol, T. Moehl, M. Grätzel and J.-E. Moser, *Nature Photonics*, 2014, **8**, 250-255.
19. M. Liu, M. B. Johnston and H. J. Snaith, *Nature*, 2013, **501**, 395-398.
20. A. Pang, C. Chen, L. Chen, W. Liu and M. Wei, *RSC Advances*, 2012, **2**, 9565-9570.
21. G. Hodes, *The Journal of Physical Chemistry C*, 2008, **112**, 17778-17787.
22. P. V. Kamat, *The Journal of Physical Chemistry C*, 2008, **112**, 18737-18753.
23. S. A. Fischer, A. M. Crotty, S. V. Kilina, S. A. Ivanov and S. Tretiak, *Nanoscale*, 2012, **4**, 904-914.
24. A. Kongkanand, K. Tvrdy, K. Takechi, M. Kuno and P. V. Kamat, *Journal of the American Chemical Society*, 2008, **130**, 4007-4015.
25. P. Guyot-Sionnest, B. Wehrenberg and D. Yu, *The Journal of chemical physics*, 2005, **123**, 074709-074709-074707.
26. N. Gaponik, D. V. Talapin, A. L. Rogach, K. Hoppe, E. V. Shevchenko, A. Kornowski, A. Eychmüller and H. Weller, *The Journal of Physical Chemistry B*, 2002, **106**, 7177-7185.
27. A. H. Ip, S. M. Thon, S. Hoogland, O. Voznyy, D. Zhitomirsky, R. Debnath, L. Levina, L. R. Rollny, G. H. Carey and A. Fischer, *Nature nanotechnology*, 2012.

28. I. Mora-Seró, D. Gross, T. Mittereder, A. A. Lutich, A. S. Susha, T. Dittrich, A. Belaidi, R. Caballero, F. Langa and J. Bisquert, *Small*, 2010, **6**, 221-225.
29. S. Kilina, P. Cui, S. A. Fischer and S. Tretiak, *The Journal of Physical Chemistry Letters*, 2014.
30. V. I. Klimov, *Annu. Rev. Phys. Chem.*, 2007, **58**, 635-673.
31. J. B. Sambur, T. Novet and B. Parkinson, *Science*, 2010, **330**, 63-66.
32. O. E. Semonin, J. M. Luther, S. Choi, H.-Y. Chen, J. Gao, A. J. Nozik and M. C. Beard, *Science*, 2011, **334**, 1530-1533.
33. S. Rühle, M. Shalom and A. Zaban, *ChemPhysChem*, 2010, **11**, 2290-2304.
34. P. V. Kamat, *Accounts of chemical research*, 2012, **45**, 1906-1915.
35. M. Shalom, J. Albero, Z. Tachan, E. Martínez-Ferrero, A. Zaban and E. Palomares, *The Journal of Physical Chemistry Letters*, 2010, **1**, 1134-1138.
36. H. Choi, R. Nicolaescu, S. Paek, J. Ko and P. V. Kamat, *ACS nano*, 2011, **5**, 9238-9245.
37. M. Grätzel, *Journal of Photochemistry and Photobiology C: Photochemistry Reviews*, 2003, **4**, 145-153.
38. F. De Angelis, S. Fantacci, A. Selloni, M. K. Nazeeruddin and M. Grätzel, *Journal of the American Chemical Society*, 2007, **129**, 14156-14157.
39. F. Schiffmann, J. VandeVondele, J. r. Hutter, R. Wirz, A. Urakawa and A. Baiker, *The Journal of Physical Chemistry C*, 2010, **114**, 8398-8404.
40. A. Y. Koposov, T. Cardolaccia, V. Albert, E. Badaeva, S. Kilina, T. J. Meyer, S. Tretiak and M. Sykora, *Langmuir*, 2011, **27**, 8377-8383.
41. A. Y. Koposov, P. Szymanski, T. Cardolaccia, T. J. Meyer, V. I. Klimov and M. Sykora, *Advanced Functional Materials*, 2011, **21**, 3159-3168.
42. M. Sykora, M. A. Petruska, J. Alstrum-Acevedo, I. Bezel, T. J. Meyer and V. I. Klimov, *Journal of the American Chemical Society*, 2006, **128**, 9984-9985.
43. H. Zhang, Z. Zhou, B. Yang and M. Gao, *The Journal of Physical Chemistry B*, 2003, **107**, 8-13.
44. X.-S. Wang, T. E. Dykstra, M. R. Salvador, I. Manners, G. D. Scholes and M. A. Winnik, *Journal of the American Chemical Society*, 2004, **126**, 7784-7785.
45. S. Giménez, A. L. Rogach, A. A. Lutich, D. Gross, A. Poeschl, A. S. Susha, I. Mora-Seró, T. Lana-Villarreal and J. Bisquert, *Journal of applied physics*, 2011, **110**, 014314.
46. I. Mora-Seró, V. Likodimos, S. Giménez, E. Martínez-Ferrero, J. Albero, E. Palomares, A. G. Kontos, P. Falaras and J. Bisquert, *The Journal of Physical Chemistry C*, 2010, **114**, 6755-6761.
47. R. Plass, S. Pelet, J. Krueger, M. Grätzel and U. Bach, *The Journal of Physical Chemistry B*, 2002, **106**, 7578-7580.
48. Y. Yin and A. P. Alivisatos, *Nature*, 2005, **437**, 664-670.
49. P. Yu, J. M. Nedeljkovic, P. A. Ahrenkiel, R. J. Ellingson and A. J. Nozik, *Nano Letters*, 2004, **4**, 1089-1092.
50. E. Dekel, D. Gershoni, E. Ehrenfreund, D. Spektor, J. M. García and P. M. Petroff, *Physical review letters*, 1998, **80**, 4991.
51. V. Sukhovatkin, S. Hinds, L. Brzozowski and E. H. Sargent, *Science*, 2009, **324**, 1542-1544.
52. D. S. Kilin, K. Tsemekhman, O. V. Prezhdo, E. I. Zenkevich and C. von Borczyskowski, *Journal of Photochemistry and Photobiology A: Chemistry*, 2007, **190**, 342-351.
53. Q. Chen, Q. Ma, Y. Wan, X. Su, Z. Lin and Q. Jin, *Luminescence*, 2005, **20**, 251-255.

54. K. Kalyanasundaram and M. Grätzel, *Coordination chemistry reviews*, 1998, **177**, 347-414.
55. A. Hagfeldt and M. Graetzel, *Chemical Reviews*, 1995, **95**, 49-68.
56. F. De Angelis, S. Fantacci, A. Selloni, M. Grätzel and M. K. Nazeeruddin, *Nano letters*, 2007, **7**, 3189-3195.
57. S. Kilina, P. Cui, S. A. Fischer and S. Tretiak, *The Journal of Physical Chemistry Letters*, 2014, **5**, 3565-3576.
58. E. M. Johansson, M. Hedlund, H. Siegbahn and H. Rensmo, *The Journal of Physical Chemistry B*, 2005, **109**, 22256-22263.
59. F. De Angelis, S. Fantacci, E. Mosconi, M. K. Nazeeruddin and M. Grätzel, *The Journal of Physical Chemistry C*, 2011, **115**, 8825-8831.
60. K. Sodeyama, M. Sumita, C. O'Rourke, U. Terranova, A. Islam, L. Han, D. R. Bowler and Y. Tateyama, *The Journal of Physical Chemistry Letters*, 2012, **3**, 472-477.
61. V. Thavasi, V. Renugopalakrishnan, R. Jose and S. Ramakrishna, *Materials Science and Engineering: R: Reports*, 2009, **63**, 81-99.
62. S. M. Morton and L. Jensen, *The Journal of chemical physics*, 2011, **135**, 134103.
63. S. M. Morton and L. Jensen, *The Journal of chemical physics*, 2010, **133**, 074103.
64. S. Kilina, K. A. Velizhanin, S. Ivanov, O. V. Prezhdo and S. Tretiak, *ACS nano*, 2012, **6**, 6515-6524.
65. M. T. Frederick, V. A. Amin, N. K. Swenson, A. Y. Ho and E. A. Weiss, *Nano letters*, 2012, **13**, 287-292.
66. S. F. Lee and M. A. Osborne, *ChemPhysChem*, 2009, **10**, 2174-2191.
67. J. Huang, D. Stockwell, Z. Huang, D. L. Mohler and T. Lian, *Journal of the American Chemical Society*, 2008, **130**, 5632-5633.
68. A. Boulesbaa, Z. Huang, D. Wu and T. Lian, *The Journal of Physical Chemistry C*, 2009, **114**, 962-969.
69. A. J. Morris-Cohen, K. O. Aruda, A. M. Rasmussen, G. Canzi, T. Seideman, C. P. Kubiak and E. A. Weiss, *Physical Chemistry Chemical Physics*, 2012, **14**, 13794-13801.
70. Y. Yang, W. Rodríguez-Córdoba and T. Lian, *Journal of the American Chemical Society*, 2011, **133**, 9246-9249.
71. K. E. Knowles, M. Malicki, R. Parameswaran, L. C. Cass and E. A. Weiss, *Journal of the American Chemical Society*, 2013, **135**, 7264-7271.
72. E. A. McArthur, J. M. Godbe, D. B. Tice and E. A. Weiss, *The Journal of Physical Chemistry C*, 2012, **116**, 6136-6142.
73. K. Katsiev, A. H. Ip, A. Fischer, I. Tanabe, X. Zhang, A. R. Kirmani, O. Voznyy, L. R. Rollny, K. W. Chou and S. M. Thon, *Advanced Materials*, 2014, **26**, 937-942.
74. A. J. Williamson, J. C. Grossman, R. Q. Hood, A. Puzder and G. Galli, *Physical Review Letters*, 2002, **89**, 196803.
75. C. M. Isborn, S. V. Kilina, X. Li and O. V. Prezhdo, *The Journal of Physical Chemistry C*, 2008, **112**, 18291-18294.
76. M. Pastore, E. Mosconi, F. De Angelis and M. Grätzel, *The Journal of Physical Chemistry C*, 2010, **114**, 7205-7212.
77. S. V. Kilina, C. F. Craig, D. S. Kilin and O. V. Prezhdo, *The Journal of Physical Chemistry C*, 2007, **111**, 4871-4878.
78. M. Eichinger, P. Tavan, J. Hutter and M. Parrinello, *The Journal of chemical physics*, 1999, **110**, 10452-10467.

79. O. Voznyy and E. Sargent, *Physical review letters*, 2014, **112**, 157401.
80. V. V. Albert, S. A. Ivanov, S. Tretiak and S. V. Kilina, *The Journal of Physical Chemistry C*, 2011, **115**, 15793-15800.
81. M. M. Hedrick, M. L. Mayo, E. Badaeva and S. Kilina, *The Journal of Physical Chemistry C*, 2013, **117**, 18216-18224.
82. R. J. Cave and M. D. Newton, *Chemical physics letters*, 1996, **249**, 15-19.
83. R. J. Cave and M. D. Newton, *The Journal of chemical physics*, 1997, **106**, 9213-9226.
84. A. A. Voityuk and N. Rösch, *The Journal of chemical physics*, 2002, **117**, 5607-5616.
85. C.-P. Hsu, Z.-Q. You and H.-C. Chen, *The Journal of Physical Chemistry C*, 2008, **112**, 1204-1212.
86. A. Kubas, F. Hoffmann, A. Heck, H. Oberhofer, M. Elstner and J. Blumberger, *The Journal of chemical physics*, 2014, **140**, 104105.
87. C.-L. Cheng, J. S. Evans and T. Van Voorhis, *Physical Review B*, 2006, **74**, 155112.
88. Y. Takimoto, F. Vila and J. Rehr, *The Journal of chemical physics*, 2007, **127**, 154114.
89. G. Kotliar, S. Y. Savrasov, K. Haule, V. S. Oudovenko, O. Parcollet and C. Marianetti, *Reviews of Modern Physics*, 2006, **78**, 865.
90. G. Baskaran, Z. Zou and P. Anderson, *Solid state communications*, 1987, **63**, 973-976.
91. A. Ishizaki and G. R. Fleming, *The Journal of chemical physics*, 2009, **130**, 234110.
92. J. C. Tully and R. K. Preston, *The Journal of Chemical Physics*, 1971, **55**, 562-572.
93. A. Neogi, C.-W. Lee, H. O. Everitt, T. Kuroda, A. Tackeuchi and E. Yablonovitch, *Physical Review B*, 2002, **66**, 153305.
94. A. Yoffe, *Advances in Physics*, 2001, **50**, 1-208.
95. O. Zakharov, A. Rubio, X. Blase, M. L. Cohen and S. G. Louie, *Physical Review B*, 1994, **50**, 10780.
96. A. L. Efros and M. Rosen, *Annual Review of Materials Science*, 2000, **30**, 475-521.
97. W. E. Buhro and V. L. Colvin, *Nature Materials*, 2003, **2**, 138-139.
98. A. L. Efros and A. L. Efros, *Soviet Physics Semiconductors-Ussr*, 1982, **16**, 772-775.
99. L. Brus, *The Journal of chemical physics*, 1983, **79**, 5566-5571.
100. S. V. Kilina, *Phonon-assisted Charge Carrier Dynamics and Photoexcited State Phenomena in Nanoscale Systems: Semiconductor Quantum Dots and Carbon Nanotubes*, ProQuest, 2007.
101. J. J. Sakurai and J. Napolitano, *Modern quantum mechanics*, Addison-Wesley, 2011.
102. D. Norris, A. Sacra, C. Murray and M. Bawendi, *Physical review letters*, 1994, **72**, 2612.
103. D. Norris and M. Bawendi, *Physical Review B*, 1996, **53**, 16338.
104. A. I. Ekimov, A. L. Efros and A. A. Onushchenko, *Solid State Communications*, 1985, **56**, 921-924.
105. Y. V. Vandyshev, V. Dneprovskii, A. Ekimov, D. Okorokov, L. Popova and A. L. Efros, *Soviet Journal of Experimental and Theoretical Physics Letters*, 1987, **46**, 495.
106. K. L. Low, Y. Yang, G. Han, W. Fan and Y.-C. Yeo, *Journal of Applied Physics*, 2012, **112**, 103715.
107. S. Kim, A. Konar, W.-S. Hwang, J. H. Lee, J. Lee, J. Yang, C. Jung, H. Kim, J.-B. Yoo and J.-Y. Choi, *Nature communications*, 2012, **3**, 1011.
108. Y.-S. Kim, M. Marsman, G. Kresse, F. Tran and P. Blaha, *Physical Review B*, 2010, **82**, 205212.
109. R. D. Schaller, M. A. Petruska and V. I. Klimov, *Applied Physics Letters*, 2005, **87**, 253102.

110. R. D. Schaller and V. I. Klimov, *Physical review letters*, 2004, **92**, 186601.
111. A. Bartnik, F. Wise, A. Kigel and E. Lifshitz, *Physical Review B*, 2007, **75**, 245424.
112. Y. Wang and N. Herron, *Physical Review B*, 1990, **42**, 7253.
113. J. Tang, K. W. Kemp, S. Hoogland, K. S. Jeong, H. Liu, L. Levina, M. Furukawa, X. Wang, R. Debnath and D. Cha, *Nature materials*, 2011, **10**, 765-771.
114. P. Hohenberg and W. Kohn, *Physical review*, 1964, **136**, B864.
115. W. Kohn and L. J. Sham, *Physical Review*, 1965, **140**, A1133.
116. C. Itzykson and J.-B. Zuber, *Quantum field theory*, Courier Corporation, 2006.
117. J. P. Perdew and W. Yue, *Physical review B*, 1986, **33**, 8800.
118. J. P. Perdew and A. Zunger, *Physical Review B*, 1981, **23**, 5048.
119. M. Petersilka, U. Gossmann and E. Gross, *Physical review letters*, 1996, **76**, 1212.
120. C. F. Craig, W. R. Duncan and O. V. Prezhdo, *Physical review letters*, 2005, **95**, 163001.
121. M. Marques, *Time-dependent density functional theory*, Springer Science & Business Media, 2006.
122. C. Leforestier, R. Bisseling, C. Cerjan, M. Feit, R. Friesner, A. Guldberg, A. Hammerich, G. Jolicard, W. Karrlein and H.-D. Meyer, *Journal of Computational Physics*, 1991, **94**, 59-80.
123. J. Tully, *Journal*, 1998.
124. J. C. Tully, *The Journal of Chemical Physics*, 1990, **93**, 1061-1071.
125. S. Hammes-Schiffer and J. C. Tully, *The Journal of chemical physics*, 1994, **101**, 4657-4667.
126. P. V. Parandekar and J. C. Tully, *The Journal of chemical physics*, 2005, **122**, 094102.
127. T. Todorov, J. Hoekstra and A. Sutton, *Physical review letters*, 2001, **86**, 3606.
128. M. Di Ventra, Y.-C. Chen and T. Todorov, *Physical review letters*, 2004, **92**, 176803.
129. Q. Wu and T. Van Voorhis, *The Journal of chemical physics*, 2006, **125**, 164105.
130. D. M. Adams, L. Brus, C. E. Chidsey, S. Creager, C. Creutz, C. R. Kagan, P. V. Kamat, M. Lieberman, S. Lindsay and R. A. Marcus, *The Journal of Physical Chemistry B*, 2003, **107**, 6668-6697.
131. H. M. McConnell, *The Journal of Chemical Physics*, 1961, **35**, 508-515.
132. M. A. Ratner, *Journal of Physical Chemistry*, 1990, **94**, 4877-4883.
133. K. D. Jordan and M. N. Paddon-Row, *Chemical reviews*, 1992, **92**, 395-410.
134. M. D. Newton, *Chemical Reviews*, 1991, **91**, 767-792.
135. R. J. Cave, K. Burke and E. W. Castner, *The Journal of Physical Chemistry A*, 2002, **106**, 9294-9305.
136. A. Kubas, F. Gajdos, A. Heck, H. Oberhofer, M. Elstner and J. Blumberger, *Physical Chemistry Chemical Physics*, 2015, **17**, 14342-14354.
137. Q. Wu and T. Van Voorhis, *Physical Review A*, 2005, **72**, 024502.
138. T. A. Betley, Q. Wu, T. Van Voorhis and D. G. Nocera, *Inorganic chemistry*, 2008, **47**, 1849-1861.
139. A. Farazdel, M. Dupuis, E. Clementi and A. Aviram, *Journal of the American Chemical Society*, 1990, **112**, 4206-4214.
140. M. S. Gordon, M. A. Freitag, P. Bandyopadhyay, J. H. Jensen, V. Kairys and W. J. Stevens, *The Journal of Physical Chemistry A*, 2001, **105**, 293-307.
141. S. Kilina, S. Ivanov and S. Tretiak, *Journal of the American Chemical Society*, 2009, **131**, 7717-7726.
142. S. H. Tolbert and A. Alivisatos, *The Journal of chemical physics*, 1995, **102**, 4642-4656.

143. A. Kasuya, R. Sivamohan, Y. A. Barnakov, I. M. Dmitruk, T. Nirasawa, V. R. Romanyuk, V. Kumar, S. V. Mamykin, K. Tohji and B. Jeyadevan, *Nature materials*, 2004, **3**, 99-102.
144. A. Puzder, A. Williamson, F. Gygi and G. Galli, *Physical review letters*, 2004, **92**, 217401.
145. E. Oh, M.-Y. Hong, D. Lee, S.-H. Nam, H. C. Yoon and H.-S. Kim, *Journal of the American Chemical Society*, 2005, **127**, 3270-3271.
146. U. Resch-Genger, M. Grabolle, S. Cavaliere-Jaricot, R. Nitschke and T. Nann, *Nature methods*, 2008, **5**, 763-775.
147. D. M. Willard, T. Mutschler, M. Yu, J. Jung and A. Van Orden, *Analytical and bioanalytical chemistry*, 2006, **384**, 564-571.
148. U. Wilhelm and J. Weis, *Physica E: Low-dimensional Systems and Nanostructures*, 2000, **6**, 668-671.
149. M. K. Nazeeruddin, S. Zakeeruddin, R. Humphry-Baker, M. Jirousek, P. Liska, N. Vlachopoulos, V. Shklover, C.-H. Fischer and M. Grätzel, *Inorganic Chemistry*, 1999, **38**, 6298-6305.
150. M. K. Nazeeruddin, R. Humphry-Baker, P. Liska and M. Grätzel, *The Journal of Physical Chemistry B*, 2003, **107**, 8981-8987.
151. A. Puzder, A. J. Williamson, N. Zaitseva, G. Galli, L. Manna and A. P. Alivisatos, *Nano Letters*, 2004, **4**, 2361-2365.
152. T. M. Inerbaev, A. E. Masunov, S. I. Khondaker, A. Dobrinescu, A.-V. Plamadă and Y. Kawazoe, *The Journal of chemical physics*, 2009, **131**, 044106.
153. B. P. Bloom, L.-B. Zhao, Y. Wang, D. H. Waldeck, R. Liu, P. Zhang and D. N. Beratan, *The Journal of Physical Chemistry C*, 2013, **117**, 22401-22411.
154. A. M. Abuelela, T. A. Mohamed and O. V. Prezhdo, *The Journal of Physical Chemistry C*, 2012, **116**, 14674-14681.
155. S. V. Kilina, A. J. Neukirch, B. F. Habenicht, D. S. Kilin and O. V. Prezhdo, *Physical review letters*, 2013, **110**, 180404.
156. J. Foresman, J. Ortiz, J. Cioslowski and D. Fox, *Wallingford, CT*, 2009.
157. P. Yang, S. Tretiak, A. E. Masunov and S. Ivanov, *The Journal of chemical physics*, 2008, **129**, 074709.
158. E. Badaeva, V. V. Albert, S. Kilina, A. Koposov, M. Sykora and S. Tretiak, *Physical Chemistry Chemical Physics*, 2010, **12**, 8902-8913.
159. V. V. Albert, E. Badaeva, S. Kilina, M. Sykora and S. Tretiak, *Journal of Luminescence*, 2011, **131**, 1739-1746.
160. T. Yanai, D. P. Tew and N. C. Handy, *Chemical Physics Letters*, 2004, **393**, 51-57.
161. J. M. Azpiroz, J. M. Ugalde and I. Infante, *Journal of chemical theory and computation*, 2014, **10**, 76-89.
162. S. Tretiak, A. Crotty, S. Fischer and S. Kilina, *Passivating ligand and solvent contribution to the electronics properties of semiconductor nanocrystals*, Los Alamos National Laboratory (LANL), 2010.
163. M. Del Ben, R. W. Havenith, R. Broer and M. Stener, *The Journal of Physical Chemistry C*, 2011, **115**, 16782-16796.
164. V. I. Klimov, *The Journal of Physical Chemistry B*, 2000, **104**, 6112-6123.
165. E. Gross and W. Kohn, *Adv. Quantum Chem*, 1990, **21**, 287-323.
166. R. L. Martin, *The Journal of chemical physics*, 2003, **118**, 4775-4777.
167. R. Dennington, T. Keith and J. Millam, *Semichem Inc., Shawnee Mission, KS*, 2009.

168. M. Frisch, G. Trucks, H. Schlegel, G. Scuseria, M. Robb, J. Cheeseman, G. Scalmani, V. Barone, B. Mennucci and G. Petersson, *There is no corresponding record for this reference*.
169. S.-I. Lu, C.-C. Chiu and Y.-F. Wang, *The Journal of chemical physics*, 2011, **135**, 134104.
170. A. Stone, *Chemical Physics Letters*, 1981, **83**, 233-239.
171. A. Stone, *Journal*, 1996.
172. M. W. Schmidt, K. K. Baldridge, J. A. Boatz, S. T. Elbert, M. S. Gordon, J. H. Jensen, S. Koseki, N. Matsunaga, K. A. Nguyen and S. Su, *Journal of computational chemistry*, 1993, **14**, 1347-1363.
173. C. Dykstra, G. Frenking, K. Kim and G. Scuseria, *Theory and Applications of Computational Chemistry: the first forty years*, Elsevier, 2011.
174. J. M. Olsen, K. Aidas and J. Kongsted, *Journal of Chemical Theory and Computation*, 2010, **6**, 3721-3734.
175. K. Aidas, C. Angeli, K. L. Bak, V. Bakken, R. Bast, L. Boman, O. Christiansen, R. Cimiraglia, S. Coriani and P. Dahle, *Wiley Interdisciplinary Reviews: Computational Molecular Science*, 2014, **4**, 269-284.
176. H. Oberhofer and J. Blumberger, *The Journal of chemical physics*, 2009, **131**, 064101.
177. M. Valiev, E. J. Bylaska, N. Govind, K. Kowalski, T. P. Straatsma, H. J. Van Dam, D. Wang, J. Nieplocha, E. Apra and T. L. Windus, *Computer Physics Communications*, 2010, **181**, 1477-1489.
178. M. T. Carter, M. Rodriguez and A. J. Bard, *Journal of the American Chemical Society*, 1989, **111**, 8901-8911.
179. R. Palmer and T. Piper, *Inorganic Chemistry*, 1966, **5**, 864-878.
180. F. G. Gao and A. J. Bard, *Chemistry of materials*, 2002, **14**, 3465-3470.
181. Y.-H. Liu, Y.-L. Lu, H.-C. Wu, J.-C. Wang and K.-L. Lu, *Inorganic chemistry*, 2002, **41**, 2592-2597.
182. F. Burstall and R. Nyholm, *Journal of the Chemical Society (Resumed)*, 1952, 3570-3579.
183. C. C. Scarborough, S. Sproules, T. Weyhermüller, S. DeBeer and K. Wieghardt, *Inorganic chemistry*, 2011, **50**, 12446-12462.
184. A. E. Kuznetsov and D. N. Beratan, *The Journal of Physical Chemistry C*, 2014, **118**, 7094-7109.
185. M. T. Frederick, V. A. Amin and E. A. Weiss, *The Journal of Physical Chemistry Letters*, 2013, **4**, 634-640.
186. A. Pal, S. Srivastava, P. Saini, S. Raina, P. P. Ingole, R. Gupta and S. Sapra, *The Journal of Physical Chemistry C*, 2015.
187. F. Jensen, *Introduction to computational chemistry*, John Wiley & Sons, 2007.
188. L. v. M. Lawson Daku, F. Aquilante, T. W. Robinson and A. Hauser, *Journal of Chemical Theory and Computation*, 2012, **8**, 4216-4231.
189. H. Paulsen, L. Duelund, H. Winkler, H. Toftlund and A. X. Trautwein, *Inorganic chemistry*, 2001, **40**, 2201-2203.
190. C. Bressler, C. Milne, V.-T. Pham, A. ElNahhas, R. Van der Veen, W. Gawelda, S. Johnson, P. Beaud, D. Grolimund and M. Kaiser, *Science*, 2009, **323**, 489-492.
191. W. Gawelda, A. Cannizzo, V.-T. Pham, F. van Mourik, C. Bressler and M. Chergui, *Journal of the American Chemical Society*, 2007, **129**, 8199-8206.
192. C. Adamo and D. Jacquemin, *Chemical Society Reviews*, 2013, **42**, 845-856.
193. P. A. Frantsuzov and R. Marcus, *Physical Review B*, 2005, **72**, 155321.

194. M. Nirmal, D. Norris, M. Kuno, M. Bawendi, A. L. Efros and M. Rosen, *Physical review letters*, 1995, **75**, 3728.
195. P. Hawrylak, *Physical Review B*, 1999, **60**, 5597.
196. V. Agranovich, H. Benisty and C. Weisbuch, *Solid state communications*, 1997, **102**, 631-636.
197. Y. Zhao and D. G. Truhlar, *The Journal of Physical Chemistry A*, 2006, **110**, 13126-13130.
198. R. Kobayashi and R. D. Amos, *Chemical physics letters*, 2006, **420**, 106-109.
199. Z.-L. Cai, M. J. Crossley, J. R. Reimers, R. Kobayashi and R. D. Amos, *The Journal of Physical Chemistry B*, 2006, **110**, 15624-15632.
200. K. Kalyanasundaram, *Coordination Chemistry Reviews*, 1982, **46**, 159-244.
201. E. Eskelinen, P. Da Costa and M. Haukka, *Journal of Electroanalytical Chemistry*, 2005, **579**, 257-265.
202. A. J. Houtepen and D. Vanmaekelbergh, *The Journal of Physical Chemistry B*, 2005, **109**, 19634-19642.
203. S. A. Blanton, R. L. Leheny, M. A. Hines and P. Guyot-Sionnest, *Physical review letters*, 1997, **79**, 865.
204. H.-W. Tseng, M. B. Wilker, N. H. Damrauer and G. Dukovic, *Journal of the American Chemical Society*, 2013, **135**, 3383-3386.
205. N. J. Cherepy, G. P. Smestad, M. Grätzel and J. Z. Zhang, *The Journal of Physical Chemistry B*, 1997, **101**, 9342-9351.
206. E. Galoppini, *Coordination Chemistry Reviews*, 2004, **248**, 1283-1297.
207. B. Di, Y. Meng, Y. D. Wang, X. J. Liu and Z. An, *Journal of Physical Chemistry B*, 2011, **115**, 9339-9344.
208. J. Huang, Z. Huang, S. Jin and T. Lian, *The Journal of Physical Chemistry C*, 2008, **112**, 19734-19738.
209. S. N. Sharma, Z. S. Pillai and P. V. Kamat, *The Journal of Physical Chemistry B*, 2003, **107**, 10088-10093.
210. V. Chakrapani, D. Baker and P. V. Kamat, *Journal of the American Chemical Society*, 2011, **133**, 9607-9615.
211. D. J. Vogel and D. S. Kilin, *The Journal of Physical Chemistry C*, 2015, **119**, 27954-27964.
212. J. Hopfield, *Journal of Applied Physics*, 1961, **32**, 2277-2281.
213. S. N. Inamdar, P. P. Ingole and S. K. Haram, *ChemPhysChem*, 2008, **9**, 2574-2579.